



The  
University  
Of  
Sheffield.

# Near Infrared Thermal Imaging for Process Monitoring in Additive Manufacturing

By:

Nicholas Boone

A thesis submitted in partial fulfilment of the requirements for the degree of

Doctor of Philosophy

The University of Sheffield  
Faculty of Engineering  
Department of Electronic and Electrical Engineering

Submission Date

15<sup>th</sup> June 2020

# Contents

Acknowledgements .....	5
Abstract.....	6
Publications .....	7
Upcoming Publications (In Preparation).....	7
List of Symbols and Abbreviations.....	8
1 Thesis Overview.....	9
1.1 Background and Motivation .....	9
1.2 Aims and Objectives .....	10
1.3 Thesis Structure .....	10
2 Introduction and Theory.....	13
2.1 Introduction to Infrared Camera Technology and Infrared Temperature Measurement .....	13
2.1.1 Brief History of Infrared Camera Technology .....	13
2.1.2 Principles of Infrared Detection.....	15
2.1.3 Operating Principles of an Infrared Camera .....	18
2.2 Introduction to Additive Manufacturing .....	19
2.2.1 Brief History of Additive Manufacturing.....	19
2.2.2 Operating Principles of Electron Beam Melting .....	23
2.3 Process Monitoring and Control in Additive Manufacturing.....	25
2.3.1 Commercial Process Monitoring Systems .....	26
2.3.2 Research Based Process Monitoring.....	27
2.4 Summary.....	31
3 Camera System Design and Calibration for Arcam EBM Imaging.....	36
3.1 Introduction .....	36
3.2 Camera and Technology Selection .....	36
3.2.1 Silicon Camera Experiment.....	38
3.2.2 Final Camera Selection .....	41
3.3 Imaging System Design.....	43
3.4 Calibration.....	48
3.4.1 Temperature Calibration .....	48

3.5	Initial Investigations.....	55
3.5.1	Overhang Test Build.....	55
3.6	Conclusion.....	58
4	Process monitoring of Electron Beam Melting with Thermal Imaging.....	61
4.1	Introduction.....	61
4.2	In Situ Part Property Investigation.....	61
4.3	Emissivity Tracking.....	64
4.4	Melt Pool Sizing Analysis for Porosity Measurement.....	71
4.5	Visualisation.....	72
4.5.1	High bit Depth Images.....	72
4.5.2	3D Visualisation.....	72
4.6	Build Stage Identification.....	74
4.6.1	Custom Acquisition Software.....	74
4.6.2	Integrating Arcam Sensors.....	75
4.6.3	Machine Learning Image Recognition.....	77
4.7	Dissimilar Metals Welding.....	82
4.8	Conclusion.....	86
5	Gas Tungsten Arc Welding Thermal Imaging and Analysis.....	89
5.1	Introduction.....	89
5.2	Turbine Blade Imaging.....	89
5.2.1	Freezing Point Detection.....	93
5.3	Pipe Welding Slag Detection and Tracking.....	99
5.4	Machine Learning for Automated Detection and Measurement.....	103
5.4.1	First Neural Network Design.....	104
5.4.2	First Network Training & Results.....	107
5.4.3	Second Network Design.....	110
5.4.4	Second Network Training & Results.....	111
5.4.5	Neural Network Segmentation Evaluation.....	113
5.5	Conclusion.....	114
6	Conclusion and Further Work.....	117

6.1	Summary of Work.....	117
6.2	Conclusions.....	119
6.3	Further Work .....	120
7	Appendices .....	122
7.1	Emissivity Tracking Code.....	122
7.2	Freezing Point Detection Code .....	123
7.3	Slag Detection Code.....	126
7.4	Neural Network Training Code .....	128

## **Acknowledgements**

I would like to thank Dr Jon Willmott for the opportunity and his help over the last 4 years, as well as sharing his interest in the field and its applications. The Sensor Systems group of Drs Hobbs, Rocket and Hodgkinson, Andy, Leigh, Mary, Matt, Matt and Todd for providing a good pace to work and sharing their expertise. The prospect of Wednesday lunch was always something to look forward to. To everyone involved with iForge, which I have really enjoyed being a part of and has been a great place for procrastination when I needed it. Also, all the technicians, support staff and everyone else that makes something like this possible. Finally, to family and friends who I almost definitely haven't seen enough of recently, hopefully we can catch up soon.

Without these people, I may still have completed this work but, it wouldn't be what it is and nor would I.

## Abstract

This work presents the design and development of a near infrared thermal imaging system specifically designed for process monitoring of additive manufacturing. The overall aims of the work were to use in situ thermal imaging to develop methods for monitoring process parameters of additive manufacturing processes. The main motivations are the recent growth in use of additive manufacturing and the underutilisation of near infrared camera technology in thermal imaging. The combination of these two technologies presents opportunities for unique process monitoring methods which are demonstrated here.

A thermal imaging system was designed for monitoring the electron beam melting process of an Arcam S12. With this system a new method of dynamic emissivity correction based on tracking the melted material is shown. This allows for the automatic application of emissivity values to previously melted areas of a layer image. This reduces the potential temperature error in the thermal image caused by incorrect emissivity values or the assumption of a single value for a whole image. Methods for determining materials properties such as porosity and tensile strength from the in situ thermal imaging are also shown. This kind of analysis from in situ images is the groundwork for allowing part properties to be tuned at build time and could remove the need for post build testing that would determine if it is suitable for use.

The system was also used to image electron beam welding and gas tungsten arc welding. With the electron beam welding of dissimilar metals, the thermal images were able to show the preheating effect that the melt pool had on the materials, the suspected reason for the process's success. For the gas tungsten arc welding process analysis methods that would predict weld quality were developed, with the aim of later integrating these into the robotic welding process. Methods for detecting the freezing point of the weld bead and tracking slag spots were developed, both of which could be used as indicators of weld quality or defects. A machine learning algorithm was also applied to images of pipe welding on this process. The aim of this was to develop an image segmentation algorithm that could be used to measure parts of the weld in process and inform other analysis, like those above.

## Publications

M. Zavala-Arredondo, **N. Boone**, J. Willmott, D. Childs, P. Ivanov, K. Groom and K. Mumtaz “Laser diode area melting for high speed additive manufacturing of metallic components,” *Mater. Des.*, vol. 117, pp. 305–315, 2017.

**N. Boone**, C. Zhu, C. Smith, I. Todd, and J. R. Willmott, “Thermal near infrared monitoring system for electron beam melting with emissivity tracking,” *Addit. Manuf.*, vol. 22, pp. 601–605, Aug. 2018.

L. Stanger, T. Wilkes, **N. Boone**, A. McGonigle, and J. Willmott, “Thermal Imaging Metrology with a Smartphone Sensor,” *Sensors*, vol. 18, no. 7, p. 2169, Jul. 2018.

## Upcoming Publications (In Preparation)

**N. Boone**, H. Martin-Reyes M. Davies, R. French and J. R. Willmott, “Detecting the freezing transition point in a TIG weld melt pool using high resolution thermal imaging and analysis”, *Addit. Manuf.*

## List of Symbols and Abbreviations

ADC – Analogue to Digital Converter

AM – Additive Manufacturing

$k$  – Boltzmann Constant

CCD – Charge Coupled Device

CMOS – Complementary Metal Oxide Semiconductor

DL – Digital Level

$\varepsilon$  – Emissivity

EBM – Electron Beam Melting

EBW – Electron Beam Welding

FDM – Fused Deposition Modelling

FIR – Far Infrared

FPA – Focal Plane Array

FPS – Frames Per Second

FWHM – Full Width Half Maximum

GTAW – Gas Tungsten Arc Welding

HDD – Hard Disk Drive

IR – Infrared

IRT – Infrared Radiation Thermometer

LPBF – Laser Powder Bed Fusion

LWIR – Long Wavelength Infrared

ML – Machine Learning

MWIR – Mid Wavelength Infrared

ND – Neutral Density

NDT – Non-Destructive Testing

NIR – Near Infrared

OD – Optical Density

$h$  – Plank Constant

PBF – Powder Bed Fusion

QE – Quantum Efficiency

RAM – Random Access Memory

SDK – Software Development Kit

SLM – Selective Laser Melting

SSD – Solid State Drive

SSE – Size of Source Effect

SVM – State Vector Machine

SWIR – Short Wavelength Infrared

UV – Ultraviolet

$\lambda$  – Wavelength

# 1 Thesis Overview

## 1.1 Background and Motivation

This work was motivated by the increase in use of additive manufacturing (AM) processes and methods in industrial settings over the recent years and the availability of high speed thermal imaging cameras. After its invention in the 1960s AM has been developed into many different technologies and over the last 20 years these have become mature enough for use in industrial manufacturing. Manufacturers have now had time to evaluate the technology and engineers are learning how to take full advantage of the design freedoms it brings, compared to traditional processes. This means the use of AM has spread out of the research divisions to become a tool available to everyone, with businesses being built around it as a sole manufacturing method.

The growth in AM usage has also started to show its weaknesses and the gaps in our understanding of the technology. Part of this is due to the need for different design methodology when targeting an additive process compared to a subtractive one. For example, the need to include drainage holes in a hollow part when using powder or resin based processes, or the need to limit the angle of overhanging faces with and FDM process. These problems have been discovered and the field of design for AM has matured but the processes themselves, although functional, are not run in an optimal way; due to lack of visibility into the process and therefore lack of understanding. This lack of visibility is where thermal imaging and other sensing methods can be applied to AM to learn more about the process and the parts it produces.

In a similar time frame to the development and adoption of AM the development of remote sensing technologies has also flourished due to the advances in electronics. This saw thermal imaging technologies go from line scanning based cameras that would take 10s of minutes to capture a low resolution image. To modern cameras capable of capturing hundreds of frames a second at multi megapixel resolutions. This has made them much more suitable for high speed analysis of processes such as AM.

Even with the field of process monitoring growing to try and fill the gaps in the knowledge of AM processes thermal imaging had not been used here until very recently. Both AM and thermal imaging contain many different technologies however, near infrared (NIR) thermal imaging cameras had not been used before, with any existing research using lower wavelength IR technologies. NIR thermal imagers are a very good match to the needs of AM process monitoring bringing higher capture speed and resolution compared to longer wavelength cameras.

## 1.2 Aims and Objectives

The main aim of this work was to demonstrate the use of a near infrared thermal imaging system for process monitoring on AM processes. The design and creation of such a system would be required and would be focused towards the electron beam melting process of the Arcam S12. The system would take advantage of modern imaging technology to provide a high speed and high resolution view into the process. This means being able to capture at speeds and resolutions on the same scale as the process itself, or closer to them than existing monitoring systems. The electron beam in the S12 can be moved at up to 1000 mm/s with up to 50  $\mu\text{m}$  feature sizes being created, ideally a system can capture the process on this scale. This would likely require custom solutions for optics and mounting, however, if the system can be realised with minimal modifications to the machine that would be best and make the work more relevant to industry.

With a system in place the aim was to use it to allow process monitoring for the EBM process and if possible, process feedback and control. This would mean the creation of new analysis techniques, both to analyse the process and the instruments in situ measurement capabilities. Process analysis methods that are able to relate features observed in the thermal data to physical changes in the part are of particular interest. These could aid other research and are likely to be metrics required for industrial monitoring of the AM processes. One element that will affect the instrument is emissivity, corrections for this will need to be incorporated into analysis techniques. Automation of the capture process and analysis was also an aim because an EBM build can take many hours and will generate huge amounts of data in that time. It would not be feasible to capture data manually for a full build.

Due to problems with the Arcam S12 machine the aims had to be changed to include work on a different process using the same technology. Working on the automated welding process the aims were to develop analysis techniques that could, in the future, be built into the feedback control mechanisms for the machine. This work would try to transfer some of the learnings from the EBM work, whilst still having the goals of learning about the welding process.

## 1.3 Thesis Structure

The structure of this thesis follows the development of the thermal imaging system created for the Arcam electron beam melting AM system and the analysis techniques designed around its output. It goes on to conclude with the application of the same technology in a welding AM process and development of analysis techniques for that application.

Chapter 2 is an introduction to the background and theory related to thermal imaging and thermal detectors and additive manufacturing. It outlines a brief history of both fields and

explores some of the technologies within each. It provides context within each field then expands on the specific technologies used in this work, by explaining the operation of CMOS thermal imagers and the electron beam melting (EBM) AM process. Finally, it presents existing work from both commercial and research projects in the area of process monitoring in additive manufacturing.

Chapter 3 details the design, calibration and initial testing of the NIR camera system on the EBM process. The design decisions relating to camera technology choice are discussed as well as some initial testing to verify that using a silicon sensor and near infrared wavelengths would be appropriate for the application. With the camera selected it then discusses some of the optical considerations for this system and how they compare to systems working at different wavelengths. The system is then calibrated to provide a temperature conversion for the images captured. The method used is based on that for single point infrared radiation thermometers because appropriate methods do not yet exist for camera based systems. Finally, this chapter shows the first use of the system on the Arcam S12 EBM machine it was designed for and its ability to detect temperature differences that could be related to defects in parts.

Chapter 4 continues with the work on in situ process monitoring of EBM. It explores analysis techniques developed around the outputs of the thermal imaging system and its use in predicting material properties. Analysis methods for emissivity tracking and build stage identification are shown. Emissivity tracking aims to improve the accuracy of a thermal image taken during an EBM build by selectively applying different emissivity values to different areas of an image based on whether that area has been melted yet. The build stage identification process uses machine learning to detect the different stages of the EBM process with a single layer. This was developed to increase the potential for automation of the image capture process. Thermal images taken during builds are also analysed to investigate the links between cooling rates and tensile strength and also melt pool size and porosity. To conclude, the system is used to image electron beam welding of dissimilar metals and is able to show indicators for the reason this process succeeds.

Chapter 5 moves on to using the NIR imaging system for process monitoring on a gas tungsten arc welding process. The automation of this process is currently being researched and the thermal imager is investigated as an analysis tool that could feed into the automation process. Two analysis techniques are shown for freezing point detection of a weld bead and slag detection on the molten weld pool. Both of these techniques could be used to indicate weld quality and be used in a feedback system. Finally, a neural network is used designed for pixel wise segmentation of the welding images. The purpose of this was to detect areas of the image for further analysis where traditional image processing methods struggled.

Finally, in chapter 6 conclusions of the work are drawn and its impact is discussed relative to existing process monitoring. Further work is also presented discussing when could be done to continue this work and areas that would need to be focused on to continue to advance thermal imaging in the process monitoring field.

## 2 Introduction and Theory

### 2.1 Introduction to Infrared Camera Technology and Infrared Temperature Measurement

#### 2.1.1 Brief History of Infrared Camera Technology

The history of non-contact temperature measurement dates back to the 19<sup>th</sup> century with the discovery of the thermo-electric effect by Thomas Seebeck in 1821. This discovery was made in search of a more sensitive detector than the liquid in glass thermometer to assist with investigations into the solar spectrum and thermal radiation. The term solar spectrum refers to what is now known as the blackbody spectrum. Using the thermo-electric effect Macedonio Melloni created the Thermomultiplier in 1833 which was the first device capable of contactless temperature measurement, able to “indicate the radiation of a person at 25-35ft”[1]. This was the first example of a thermopile, a technology still in use today.

The next technological development in infrared detection was the bolometer, by Samuel Pierpont Langley in 1880. This improved on the speed, detection range and precision, being able to detect temperature changes of  $10^{-5}$  °C[2]. With further developments in the coming years by Langley and his assistant Charles Greeley Abbot. The bolometer elements were reduced in size resulting in detection cells between 1 and 10  $\mu\text{m}$  in width. This allowed for even more accurate investigation into the solar spectrum when accompanied with a prism and used like a modern spectrometer.

The next development towards modern infrared camera technology used for remote sensing came from an early leap in television. The Hungarian inventor Kalman Tihanyi patented the Radioskop in 1929[3]. This technology had similarities to the Cathode Ray Tube television technology that later succeeded, but was much more advanced than the mechanical televisions being developed and manufactured at the time. A version of this system capable of infrared detection was developed by Tihanyi and the British military as part of research into remote controlled aircraft. The infrared television system would give the remote pilots night vision capabilities[4]. This technology was recognised by the US military and was developed by Radio Corporation of America (RCA) and deployed in World War 2[5].

The US Military continued developing infrared detection technology after the war and in partnership with Texas Instruments (TI); developing the first infrared line scanners in the early 1950s. These were designed for military reconnaissance among other applications. The line scanner systems were developed and deployed on aircraft to provide extra sensing capabilities for crew and were termed Forward Looking Infrared systems, gaining the acronym FLIR. Early line scanners were slow both because of their detection and

scanning methods (bolometers and scanning mirrors); taking up to 20 minutes to capture an image.

The first commercial cameras became available in the 1960s using the same principles as those developed by TI and the military. AGA's Thermovision line was the first commercially available IR camera and was used in medical imaging and by power companies to perform predictive maintenance on their power lines amongst other applications[6]. These used a liquid nitrogen cooled Indium Antimonide detector for the short wave (3-5  $\mu\text{m}$ ) and a Mercury Cadmium Telluride detector for the long wave (8-14  $\mu\text{m}$ ) versions[7].

The first IR focal plane arrays (FPA) were developed following the invention of the CCD detector in 1970[5]. An FPA is a 2D detector allowing the capture of an image without optical or mechanical scanning. Because of the close link to CCD technology infrared FPAs took advantages of the rapid developments in this technology to become quicker, higher resolution and less noisy. CCD and IR CCD technology led the industry for years and by 1995 mass production of IR FPAs was taking place with uncooled detectors being developed[5].

Uncooled detectors were the next step towards modern IR camera technology. Under development at TI from the mid-1970s uncooled FPA were considered ready for publication and production in 1992[8]. These took advantage of CMOS readout technology and worked at room temperature because of the composition of the sensor. This reduced the cost and complexity of the technology and enabled its more widespread use, for example in infrared CCTV security cameras.

Uncooled FPAs were the first move in the latest developments in IR cameras. The use of CMOS readout technology came with many advantages over CCD especially when moving into a more digital world. Images sensors with CMOS readout circuitry convert the charge from the photodetector into a voltage at the pixel level rather than at the row based readout level like in CCDs. Being a newer technology, this initially came with higher noise and image quality problems but as the technology developed this was reduced. One of the advantages of using a pixel level voltage readout is that image processing can be integrated into the camera or even sensor. This was not previously possible on sensor because of the size and speed of the readout circuitry. It also lends itself to being digitised on the sensor allowing even smaller packaging possibilities and easier system integration vs a CCD needing external analogue to digital conversion.

The improvement in CMOS technology in other areas of the industry has been taken advantage of to manufacture increasingly higher performance infrared FPAs. Pixel pitches, for example, have decreased from 45 $\mu\text{m}$  in the year 2000 to 12 $\mu\text{m}$  in 2010 [5]. This has allowed higher resolution FPAs to become available with the speed advantages the mature CMOS technology gives. Also, with the advancements in CMOS and semiconductor

processing in general multispectral two colour detectors have become available. These FPAs stack 2 detectors on top of each other at the silicon level, allowing 2 images at different wavelengths to be produced in one exposure. However, this technology is not yet at the stage of single colour FPAs, with large pixel pitches and lower resolutions.

Current commercial detector technologies for IR FPAs are grouped by wavelength range SWIR (Short Wavelength Infrared), MWIR (Mid Wavelength Infrared) and LWIR (Long Wavelength Infrared) which operate at 0.9-1.7  $\mu\text{m}$ , 3-5  $\mu\text{m}$  and 8-12  $\mu\text{m}$  respectively. The SWIR range is primarily made up of InGaAs detectors and have a resolution of up to 640x512 with a pixel pitch of around 15  $\mu\text{m}$ . SWIR is used for inspection, anti-counterfeiting and surveillance as well as temperature measurement in an application like process control. MWIR FPAs made from InSb detectors have seen more development than SWIR FPAs due to their use in military applications. This has caused higher resolution 1280x1024 sensors to be commercially available in cameras. MWIR also has industrial uses in gas detection and inspection, for example. MWIR devices are often cooled making them bulkier and more costly than other technologies. LWIR devices have also seen development because of military applications but, are also heavily used in medical applications. HD resolution (1920x1080) LWIR cameras can be found and this resolution is taken advantage of in many applications like person detection in rescue situations, ball detection in sports and lower temperature industrial process monitoring.

One range of wavelengths lesser used, especially when thermal imaging is considered, is the Near Infrared (NIR) at 0.7-1.4  $\mu\text{m}$ . This band does cross with the SWIR wavelengths but, when considering wavelength bands in relation to detector technologies NIR is often shortened to 0.7-1  $\mu\text{m}$  and SWIR to 1-1.7  $\mu\text{m}$ . This fits with the sensitivity range of silicon at 0.3-1  $\mu\text{m}$ . Silicon FPAs are used for visible wavelength detectors so have seen the most development. State of the art silicon sensors reach multiple 10s up to 100 megapixel resolutions with pixel pitches of around 4  $\mu\text{m}$ . However, these sensors are optimised for use in the visible range, sensors with a greater responsivity in the NIR wavelengths often reach only multi megapixel resolutions.

### **2.1.2 Principles of Infrared Detection**

#### **2.1.2.1 Planck's Law**

Planck's law is the fundamental rule on which all infrared temperature measurement is based. Derived in 1900 by Max Planck it describes the spectral energy density of radiation emitted by a blackbody at a given temperature.

The blackbody spectrum described by Planck's law is the maximum energy an object can emit per unit area and unit wavelength. It therefore assumes a perfect blackbody, which is defined as a body with an emissivity of 1 at all wavelengths and absorbs all radiation incident upon it. Emissivity is the ratio of the radiation an object emits compared to that of

a perfect blackbody at the same temperature. In reality objects with an emissivity of 1 do not exist so the emissivity value is used to apply Planck's law to the real world.

$$B_{(\lambda,T)} = \frac{2hc^2}{\lambda^5} \frac{1}{e^{\frac{hc}{\lambda kT}} - 1} \quad 2.1$$

Where:

$B_{(\lambda,T)}$  is spectral radiance with respect to wavelength and temperature  
 $h$  is the Planck constant  
 $c$  is the speed of light in m/s  
 $\lambda$  is the wavelength in m  
 $k$  is the Boltzmann constant  
 $T$  is the blackbody temperature in K

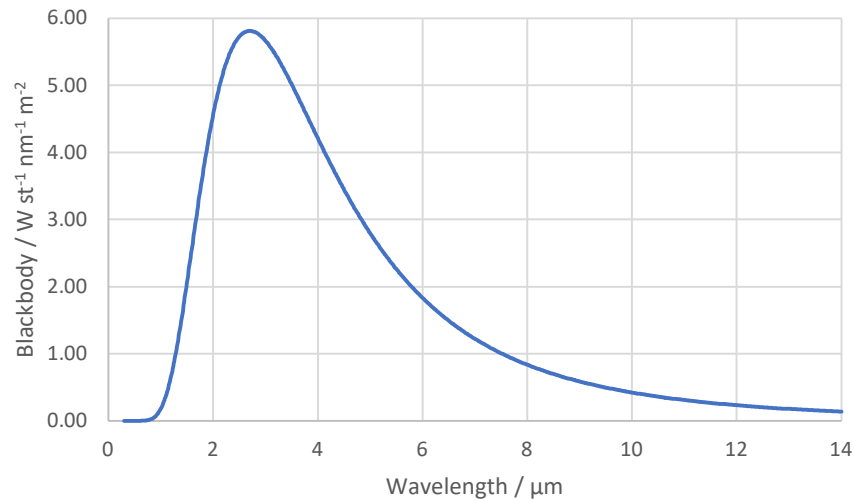


**Figure 2.1 Example blackbody spectrum for 800 °C**

In IR temperature measurement Planck's law is used to model the theoretical radiance of an object at a given temperature and wavelength or band of wavelengths. This allows the calibration and characterisation of instruments when they are used to measure an approximate blackbody source (with an emissivity of 0.99 or greater).

#### 2.1.2.2 Wien's Distribution and Displacement Laws

The Wien distribution law (also now called the Wien approximation) was the best model of blackbody radiation prior to Planck's law. Derived in 1896 by Wilhelm Wien it was designed to describe the full blackbody spectrum but was not accurate at long wavelengths.

$$I_{(\lambda,T)} = \frac{2hc^2}{\lambda^5} e^{-\frac{hc}{\lambda kT}} \quad 2.2$$

Where:

$I_{(\lambda,T)}$  is spectral radiance with respect to wavelength and temperature  
 $h$  is the Planck constant  
 $c$  is the speed of light in m/s  
 $\lambda$  is the wavelength in m  
 $k$  is the Boltzmann constant  
 $T$  is the blackbody temperature in K

The Wien approximation is still used because of its simpler form when working at short wavelengths. The Wein approximation is valid for wavelengths shorter than the peak wavelength of the blackbody spectrum for a given temperature.

Wien's displacement law defines the peak blackbody emission at a given temperature and was derived by Wien in 1893. Through this law the peak emission wavelengths can be seen to decrease as temperature increases.

$$\lambda_{peak} = \frac{2.898}{T} \quad 2.3$$

Where:

$\lambda_{peak}$  is the peak wavelength in m  
 $T$  is the blackbody temperature in K

### 2.1.2.3 Sakuma Hattori Equation

The Sakuma Hattori equation was developed by Fumihiro Sakuma and Susumu Hattori in 1982 to fit detector output to the Planck equation for calibration purposes. It is used to model detector output for a given temperature with the use of fitting variables that can be related to the characteristics of the measurement device. It is also used in its inverse form once the device has been characterised to relate device output to temperature.

$$S_{(T)} = \frac{C}{e^{\frac{hc}{AkT+B}} - 1} \quad 2.4$$

Where:

$S_{(T)}$  is the device output with respect to temperature  
 $T$  is temperature in K  
 $h$  is the Planck constant  
 $c$  is the speed of light in m/s  
 $k$  is the Boltzmann constant  
 $A, B$  and  $C$  are the fit variables

The expanded form is shown here to relate to the full form of the Planck equation (2.1) but it is often used with the second radiation constant  $c_2 = \frac{hc}{k} = 0.014387752$  m/K. The equation can be used directly in this form when considering narrow band measurement devices or can be used with broadband devices by integrating over the wavelength band required. The A and B parameters of the equation can be related to physical properties of the device being characterised and calculated values and be used for a starting point on a fit or, to tie the fit back to the properties of the device. A is generally accepted to be close to the central wavelength of the spectral response of the device[9], and B related to the defining spectral characteristics of the device e.g. the primary filter bandwidth[10] using the below equations.

$$B = \frac{c_2}{2} \left( \frac{\sigma}{\lambda_0} \right)^2$$

2.5

Where:

$$\sigma^2 = \frac{FWHM^2}{12}$$

Where:

 $c_2$  is the second radiation constant $\lambda_0$  is the centre wavelength in m $FWHM$  is the Full Width Half Maximum of the defining filter in m

### 2.1.3 Operating Principles of an Infrared Camera

Most infrared cameras are based on one of 3 detection technologies depending on sensitive wavelength (discussed above) and corresponding electronics to create a usable output signal for another device. CCD and CMOS based cameras will be described here, however microbolometer cameras work in a very similar way. Charge Coupled Devices (CCD) sensors and Complementary Metal Oxide Semiconductor (CMOS) sensors both work in the silicon wavelengths (0.3-1  $\mu\text{m}$ ), but the technology can be extended to the full SWIR range with the use of InGaAs photodetectors paired with either of the two readout methods.

CCD is the older technology of the two with most modern silicon based image sensors using CMOS, however CCD is still used in certain scientific applications where CMOS has not yet been proven to have a low enough noise level. The differences between the two technologies lie in how and where charge from the photodetector is converted into a voltage. These differences lead to the defining characteristics of the FPAs and the cameras as a whole.

CCD sensors rely on moving charge around the sensor, giving them their name. Each pixel on a CCD sensor contains an area of photosensitive material that will create charge (also termed photoelectrons) from the light incident upon them. This charge is accumulated in a potential well under one of the electrodes laid on top of each pixel. There are 3 electrodes on each pixel which allows the charge to be clocked out from each pixel in turn along a row or column. By activating each electrode in turn, the charge from the pixel will move under that electrode and form a shift register to move the charges along. When a charge reaches the end of the row or column it is then shifted using the same method in the other dimension to reach the conversion and readout electronics in the corner of the FPA[11], [12].

The conversion electronics on a CCD consist of a capacitor to convert the charge from the photodetector into a voltage and an amplifier to amplify this voltage to a useful level. The readout electronics then either digitise this voltage using an analogue to digital converter (ADC) to create a digital output or it is passed through more analogue circuitry to create an analogue waveform corresponding to the image data.

The single set of readout electronics give a CCD based camera its main advantages and disadvantages. The advantage of having only one set is that CCDs traditionally produce less noise and more uniform images because there is only one point for the signal to be affected by outside factors like temperature. However, using a single set of readout electronics limits the speed of the device because the device can only be clocked so fast whilst still allowing time for light collection and time to shift out every pixel sequentially. CCDs also suffer from 'blooming' where charge will spill out from pixels with a lot of incident light onto those around it.

A CMOS sensor works in a similar way using a photodetector in each pixel to convert incident light into charge, however rather than moving that charge to a single set of conversion electronics each pixel has conversion electronics to create a voltage. This voltage is then sampled row by row where it is digitised by a corresponding number of ADCs the read off the FPA digitally [12]. This process is fundamentally the same as a CCD but with greater complexity. Each pixel in a CMOS array will contain multiple transistors and in newer designs even ADC capabilities.

This architecture leads to CMOS sensors being much quicker to read out because whole rows are read at once; and multiple sets of readout electronics can be used to read out sub arrays of the sensor in parallel. However, it also means that there is more variability in the readout process, if each set of readout circuitry is not exactly matched fixed pattern noise can be introduced. This is where some columns will read out different values for the same pixel voltage. With multiple amplifiers and ADCs temperature variability across the sensor will also affect the readout of individual pixels or columns by having a different effect on the noise introduces to each device. It is because of these disadvantages that CMOS adoption was slow for scientific devices. However, manufacturing processes have improved to lessen these affects and some cameras now also contain electronics to correct for these effects before presenting the image to the user.

After an image has been read from the sensor an algorithm or lookup is performed to transform the raw image data into a temperature. The raw data will either be in the form of a digital level (DL) for each pixel for an analogue voltage. The conversion algorithm or lookup will be defined in the calibration process of the instrument. This which will usually involve measuring the devices output at defined temperatures then creating a model to interpolate these points and create a full range of temperature values for the devices output.

## **2.2 Introduction to Additive Manufacturing**

### **2.2.1 Brief History of Additive Manufacturing**

Additive manufacturing (AM) is an overarching term that refers to all additive manufacturing processes, opposed to subtractive ones. It is defined by ISO/ASTM 52900 as

the “process of joining materials to make parts from 3D model data, usually layer upon layer, as opposed to subtractive manufacturing and formative manufacturing methodologies”[13]. This means additive processes are differentiated from more traditional manufacturing processes like milling, turning, casting or forging; these techniques would fall into the subtractive (milling, turning) and formative (casting, forging) categories.

Additive manufacturing, also known as 3D printing, is considered by most a relatively recently developed technology, however, its research dates back to the 1960s. The research conducted in the late 1960s used multiple lasers at different wavelengths to cure a photosensitive resin in a vat[14]. At the time this was called photochemical machining but is the predecessor of the technology known today as vat polymerisation. This technology was developed and patented by different organisation throughout the 1970s. These developments are often overlooked because of the differences to today’s technologies.

The person often credited with the invention of 3D printing is Hideo Kodama of the Nagoya Municipal Industrial Research Institute in Japan. In 1980 he filed a patent application for a technology called stereolithography, this technology although similar to those before it was much simpler; using a single laser to cure a single layer of photosensitive resin at a time. The prototypes for this machine can be seen in his 1981 paper “Automatic method for fabricating a three-dimensional plastic model with photo-hardening polymer”[15] and was the first process to work layer wise and driven from 3D model data from a PC. This is the same way most of today’s AM processes are driven, which is likely the reason he is often cited as the inventor of AM and 3D printing. Kodama’s process used a UV curable resin and could reach layer resolutions of 0.1 mm. The first model shown in the paper is of a house consisting of 27 layers at 2 mm thickness with 10 minutes cure time for each layer, the full model taking 4.5 hours to complete.

Other companies worked on stereolithography systems and development through the early 1980s, but most were abandoned, or came to nothing until Charles Hull formed 3D Systems in 1984 and patented the stereolithography apparatus (SLA) technology[16]. 3D Systems were the first company to commercialise and have success with 3D printing with their SLA-1 machine. The process worked in fundamentally the same way as the one Kodama demonstrated, curing layers of UV sensitive resin with a laser. This process started the AM industry with the stereolithography process being developed heavily throughout the 1980s and 1990s and continues to be one of the leading technologies for polymer based AM today.

In the early 1990s other polymer processes started to be introduced into the market. In 1992 Statasys introduced fused deposition modelling (FDM) technology with its first

product the 3D Modeler[17]. FDM technology works in layers, like stereolithography, however rather than using a laser to cure resin, it uses a nozzle to extrude molten polymer. Also in 1992 Selective Laser Sintering (SLS) was introduced by DTM (now part of 3D Systems)[18]. SLS uses a laser to selectively fuse areas of powder layer by layer and form the 3D object. Both of these technologies were successful and are still widely used today.

Later in the 1990s and early 2000s metal AM systems started to be commercialised with EOS developing Direct Metal Laser Sintering (DMLS) in 1994[18], Optomec releasing Laser Engineered Net Shaping (LENS) machines in 1998[19] and Arcam releasing Electron Beam Melting (EBM) machines in 2002[20]. These 3 products represent 3 different methods of metal AM; DMLS and EBM are similar in that they are both powder bed fusion (PBF) systems. In PBF systems a layer of metal powder is laid down on top of a build plate, the energy source for the system then draws the layer, fusing it to the bed or previous layer then the bed is moved down by the layer height and the process repeated. The technology for this style of AM was developed at the Fraunhofer Institute[21]. Both of these processes create fully dense part by melting the powder; other approaches also exist that sinter the powder, rather than melting, which requiring post processing. The difference between the two systems is their energy source; DMLS uses a laser and EBM an electron beam. The LENS system, developed by Optomec, is an example of direct energy disposition (DED) and works by using a moving head to deposit and melt metal powder along a path. The powder is deposited onto the bed or previous layer and instantly melted by a laser. These systems are all still in use and development today. They are some of the most popular metal AM processes, as well as metal SLS.

In the mid to late 2000s the 3D printing market began to grow, one of the possible reasons for this is the RepRap project from the University of Bath[22]. This open source project generated a lot of consumer and hobbyist interest in AM, which has also translated into the industrial world through engineering and public interest. The global AM market was worth \$1 billion in 2009[23] and has continued to grow to \$9.3 billion in 2018[24].

Current AM technologies can be classified into 7 areas; material extrusion, powder bed fusion, material jetting, binder jetting, vat polymerisation, sheet lamination and direct energy deposition[25]. Some of these technologies have been discussed above (material extrusion, vat polymerisation, powder bed fusion and direct energy disposition) and represent some of the major advances in their specific areas and the overall AM development history. The principles of the other methods will be described, and example uses cases given for all methods.

The material and binder jetting processes are similar but have a fundamental difference. Both of these technologies use moveable print heads with deposition nozzles that resemble traditional 2D ink jet print heads. The difference is in what each process deposits

from the print head, the material jetting technology directly deposits the printable material, often mixed with a suitable solvent, onto a substrate. Binder jetting however deposits a binder substance onto a bed of the printable material, selectively binding areas of that material together. The material here is usually in powder form. Both of these processes, depending on the setup, can require post processing steps such as curing of the binder or evaporation of the solvent, for example. An example of material jetting is Optomec's Aerosol Jetting technology[26], this technology is used for 3D printed electronics by depositing layers of conductive and semiconductor materials. HP's range of 3D printers are examples of binder jet technology[27] and work with both metals and polymers. This process is often very high resolution and is used for high quality prototyping and small run production parts in various industries.

Sheet lamination processes create objects using thin sheets of metal (or other materials that can be formed into sheets or rolls) that are bonded together layer by layer, with the part geometry being cut from each sheet by a laser or knife. There can be post processing required to remove excess sheet material after cutting, depend on the exact process and material. This process can be very cheap depending on the material used but cannot be used for structural parts because the bonding method used tends to be weak. This means the technology is used for cosmetic objects and quick turnaround non-functioning prototypes[28].

Material extrusion processes, such as FDM, are primarily used for polymers and are used in many industrial applications as well as being the primary technology for consumer 3D printers. Depending on the exact polymer and machine used parts produced with material extrusion can be mechanically strong[29]. Therefore, they can be used as structural parts and often have good enough resolution to be used for visual mock-ups and modelling.

Powder bed fusion processes work with both metal and polymer powders and can produce fully dense parts. This means parts can be used structurally because they have properties close to that of the solid material. The Aerospace and automotive industries are heavily investigating the use of this technology because it could provide them more design freedom and weight saving. It is also actively being used in the medical industry to create custom implants for joint replacements[30].

Vat polymerisation technologies, like stereolithography, can achieve levels of details that other technologies cannot. This in combination with being able to produce solid parts lends itself to being used in areas with needs for high detail on a small scale. Industries that are applying this technology include robotics and medicine[31].

Direct energy deposition technologies can be used to build fully dense parts, like powder bed processes for example, but they also have the ability to build on existing parts to perform repairs. This is one of the main advantages of the technology and it is being used

in the aerospace industry to automate the repair of turbine blades for example[32]. The process can also be used to deposit coatings of different metals onto parts to give them different finishes or qualities the base material would not have.

### 2.2.2 Operating Principles of Electron Beam Melting

This work is primarily based around the Electron Beam Melting (EBM) process by Arcam, this section will describe in more detail the powder bed fusion (PBF) process and specifically EBM. The PBF process uses selective sintering or melting of powders to create freeform geometry in a layer by layer process. With EBM metal powders are used and the powder is fully melted but both polymer and sintering PBF processes do exist. This means the EBM process can produce fully dense parts, requiring little to no further processing depending on the application and finish required.

A diagram of the Arcam S12 used in this work can be seen in Figure 2.2. The first step of a build is to evacuate the build chamber down to a pressure of approximately  $1 \times 10^{-5}$  mbar. This is done to ensure the electron beam reaches the build plate with as few collisions with particles in the chamber's atmosphere as possible, passing the maximum amount of energy into the plate or powder. Next the electron gun voltage is raised to 60 kV, this high voltage is passed through a tungsten filament at the top of the beam column to generate electrons. The electrons are accelerated, steered and focused by a series of electromagnets lower in the beam column. This produces a focused high-power beam of electrons that can be aimed anywhere on the build plate. The current passed through the filament is used to control the number of electrons generated and therefore the total power of the beam.

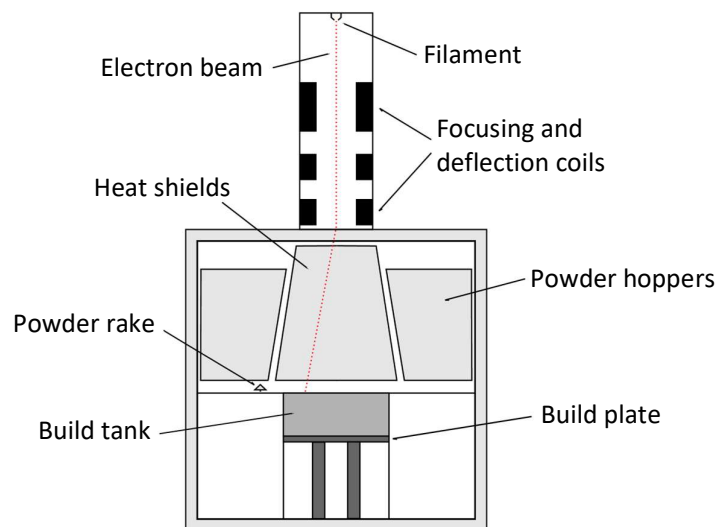


Figure 2.2 Arcam S12 system diagram

Before any powder is laid down the build plate is preheated to  $\sim 600$  °C using the electron beam. This is done with the beam deliberately defocused to spread the beams energy out

so not to risk damaging the build plate by melting it. The purpose of the preheat step is to slow the cooling of the first layers of the build; if powder was melted straight onto a cold build plate it would experience extreme cooling because of the heat sinking effect of the plate. This would cause stress in the material, potentially causing cracks in the part or undesirable material structure.

Once the preheat is completed the build begins by lowering the build plate by the height of the first layer (usually 70  $\mu\text{m}$  but is variable depending on the build). A layer of powder is then deposited on the bed by the rake which rakes powder from the hoppers on either side of the bed. 3 or more passes of the rake are usually performed to ensure an even layer of powder. A second preheat will then take place lightly sintering all the powder in the build area. This is done with a lower power, defocused beam compared to the melting power and helps to keep powder from being ejected from the bed when it is hit with the full power electron beam.

The layer pattern is then melted into the sintered powder. This pattern is defined in the build preparation step where the 3D model is transformed into a series of layers. The standard process of melting a layer will contour the part first, melting the outside walls, then melt the internal structure of the part with a hatch or raster pattern, defined in the preparation stage. This process is variable depending on the part being built or the material used. The beam can travel at different speeds and with different powers and focus ratios to define the amount of energy put into the powder and different algorithms can be used to define the route of the beam. These as well as other parameters can be tuned to the material, part, or even desired material structure and heat treatments.

After a layer is completed, the powder deposition and melting steps are repeated for every layer defined for the build. This leaves a built part welded to the build plate and surrounded by sintered powder in the build tank. To remove the part the build plate is raised back to its starting level so the plate can be removed. To remove the sintered material around the part high pressure air is used to blast raw powder at the block and break it down, the sintered powder can be further broken down, sieved and then reused. Finally, wire erosion is used to remove the part from the build plate.

EBM has certain advantages and disadvantages over other PBF processes. The fact EBM requires a vacuum can be both; it enables EBM to use materials some other processes cannot because of oxidisation concerns at high temperatures for example. It also means that, when coupled with the heating of every layer, cooling rates can be much lower than other processes. Depending on the material and desired structure this can again be either advantageous; allowing a wider range of materials to be built successfully, or a disadvantage because builds take longer, and some material properties and structures are harder to control. Also because of the sintering of each layer of the powder bed the

external surface finish of EBM parts tends to be very rough in comparison to non-sintering processes.

### 2.3 Process Monitoring and Control in Additive Manufacturing

Most AM processes are entirely computer controlled however, very few incorporate any feedback or process monitoring. Most AM systems rely on highly tuned models of the process and open loop control, with little to no feedback when running. The machines will work in this way however, they cannot detect when something has happened in the process that does not match its model. This means that anomalies in a build can build up and cause a catastrophic failure of a build which could damage the machine.

One example of this in EBM could be too much energy input into melting a material causing it to swell. If this happens over consecutive layers the solidified part could start to protrude above the level of the powder bed. The next time a new layer of powder is deposited the part will catch on the rake and damage it. On further layers the rake will now deposit an uneven layer of powder as shown in Figure 2.3. This will worsen the swelling in the area, because there is more powder to melt, or could scatter powder around the chamber if it does not sinter properly. The scattering of powder is a problem because if powder gets close to the electrodes used to create the electron beam it can cause arcing between them or an electrical short circuit. This would require the build to be stopped and the electrodes to be cleaned or replaced.

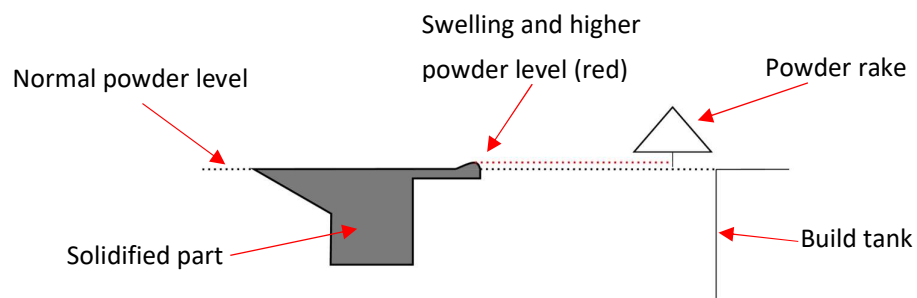


**Figure 2.3 Diagram showing how swelling on a part could cause uneven powder distribution. Here the rake is moving left to right and has been damaged by the swelling on the part due to excess energy input**

If these AM processes are to be truly adopted by industry issues like this must be rare or predictable so they can be mitigated with maintenance. The example given above would cause a build to fail and take hours to fix, this is not acceptable in a manufacturing environment.

The Arcam S12, focused on in this work, does have 3 potential systems for feedback and process monitoring; powder sensors positioned either side of the bed, a thermocouple in the build plate and a greyscale camera looking at the powder bed from above. These sensors only have limited use for process monitoring, if they are used at all. The powder

sensors detect when the rake has successfully deposited a new layer across the bed, however, they often do not detect powder falling through them. This means the controller automatically rakes the bed again to ensure a layer has been deposited, ignoring the sensor input. The thermocouple is used to monitor the build plate temperature during preheating. However, after this step is finished it becomes of little use to system because it gets further away from the current layer as the build progresses. The camera is also not used by the control system, instead it is just presented to the operator for manual inspection.

It is not only the Arcam machines that operate like this, machines from other manufactures are similar and have not progressed over time to include monitoring features. Newer machines and manufacturers, like Aconity 3D[33] for example, do include more sensors that are designed to be part of the process control algorithm for the system. However, they are not currently integrated in a way to provide real time feedback. The Aconity systems provide high speed cameras and pyrometers that are mounted coaxially on the laser path, allowing them to view the melt pool. The data from these sensors is available to the system and the operator and can be recorded or monitored, but they are not currently used by the control systems to implement any kind of feedback or verification.

This level of sensor integration is progress and while it may not help with the manufacturing application of these machines, it does assist those actively developing processes and powders for use with PBF AM processes. This is one of the other use cases for process monitoring in AM, until now powder development and process refinement has largely been a trial and error process with a long feedback loop. Whether the application is new powder development, build parameter optimisation or material characterisation; having the relevant sensors on the AM process helps to shorten the feedback loop and provide more information to the operator.

### **2.3.1 Commercial Process Monitoring Systems**

Commercial examples of process monitoring systems for AM do exist. Some have been developed by machine manufacturers specifically for their machines, others developed for a specific application and designed to integrate with machines. One example of a manufacturer solution is Arcams LayerQam system[34]. This system is marketed for defect detection in Arcams EBM process and is available for Arcam A2 models and newer. This system tracks the porosity of a part throughout its build via a camera system but does not feedback into the machine for correction purposes. LayerQam is installed by default on the latest Q series machines showing Arcam recognises that this kind of technology is required in the AM field, although it is not yet integrated into the control algorithms. Being a proprietary technology there is little information on how the LayerQam system works.

Another manufacturer solution developed by Laser Concept for their SLM machines is the QM Meltpool 3D system[35]. This system uses a CMOS camera and a photodiode mounted in the optical path of the laser to monitor the melt pool. Melt pool monitoring on SLM systems are much more commonplace than on EBM and other AM processes because the existing laser optical path can be used and is always focused on the melt pool. The QM Meltpool 3D system is capable of measuring melt pool size, with the camera, and average melt pool intensity, with the photodiode. This is correlated with data from the machine control system to create a stack of images that relate to each layer of the build and contain the melt pool size and intensity data. This again allows potential defect areas to be detected but relies on manual analysis of the output data by an operator. Therefore, this system can offer a history of a parts build process but no feedback without manual, offline intervention.

Other commercial monitoring system exists, mainly for laser based processes, but are based around the same technologies used in the QM Meltpool 3D system and provide similar outputs. Newer AM machines are integrating more sensors with on axis photodiodes and cameras becoming more common on SLM and other laser based technologies. However, even though the sensors are being included on machine more often, they are still not being used for more than is described above. Most cameras are being used to provide visual feedback to operators, but this data is not recorded and is often only from a low speed, low bit-depth visible light camera, so would be of little use for analysis.

### **2.3.2 Research Based Process Monitoring**

There are more process monitoring projects still at the research stage focused around different AM processes. Some of these exist only on custom machines designed specifically for development of process monitoring or AM metrology techniques. However, others are based on existing commercial AM machines that have been modified to varying degrees. Most systems in the research stages have not developed fully into process control systems but are still at the stage of process monitoring. They are used to inform further development of the systems themselves as well as the machines, strategies and materials used in the processes.

In a review of process monitoring in metal AM Tapia and Elwany[36] highlight the primary advantage of using an infrared thermometry based monitoring system as, in theory, any surface within the field-of-view of the sensor can have its temperature monitored in a contactless way. This makes this approach well suited for AM processes like EBM as it allows a moving melt pool to be monitored with only a single sensor or imager array for example. It also means that neither the part nor build process will have to be modified to accommodate appropriate areas for measurement. They do, however, state that infrared

thermometry does have some drawbacks. For example; the cost of equipment and the need for high frame rates to properly capture a process like EBM at full speed and in the amount of detail required, which will further increase the cost of equipment. This is especially true of infrared cameras with the technology used in MWIR, most likely to be based on thermal detection or 3-5  $\mu\text{m}$  semiconductors and have slow read out speeds or low spatial resolution. However, silicon detectors do not have these drawbacks and in the time since this review was written both silicon and longer wavelength camera technology has matured and dropped in price.

In a later review of AM monitoring techniques Everton et. al.[37] highlight the recognition from industry that process monitoring in AM will be a required feature in the future to ensure part quality. They go on to say that current techniques are not at the stage that they can fully replace traditional offline part verification and non-destructive testing (NDT). But, there is a significant effort from research institutions in this field which is being supported by industry. They again highlight the use of imagers as advantageous for many AM techniques, especially powder bed based systems.

Industry is actively working with research institutions to develop monitoring techniques and in a NIST workshop[38] directly highlighted the need for in process monitoring and NDT methods for AM processes. Systems were identified as lacking real time measurement, high speed video and thermal imaging and detection of build anomalies such as thermal gradients. Off the back of this call from industry NIST started research on the metrology of AM and how process monitoring could be achieved using thermal imagers. Lane et. al.[39] show the calibration procedure of a high magnification SWIR system using commercial off-the-shelf parts. This paper focuses heavily on the metrology and is unlikely to be a feasible setup for a commercial or industrial system, but it does start to explore the level of detail required for accurate measurements in AM via thermal imaging. Methods are shown in the above paper for dealing with emissivity and the cameras optical system. They suggest that corrections at the level of image deconvolution with the point spread function (PSF) will be necessary to accurately measure the small feature sizes seen in some AM processes, even with a high magnification camera.

In a review of the measurement science need for real time control in AM from NIST, Mani et. al.[40] discuss current control systems based on cameras and photodiodes that are mainly used to provide similar information to those of the commercial options above. Camera systems are also being used to monitor layer geometry and match it to layer data generated in the build setup process. Based on the differences between the live build data captured by the camera and the model data the authors can correct for shrinkage in parts by changing build themes[41]. Based on the existing work like this and others Mani et. al. identify the need for process signatures to be identified in specific AM processes before

the measurement challenges can really be addressed. The relationships between process inputs, the process signatures and part quality and properties need to be found. This will lead to more tightly integrated control schemes in the future that can directly control built part properties, by controlling the process signatures in real time. Currently this leaves a wide area open for research in finding the relationships and creating accurate methods to monitor the signatures. Mani et. al. do suggest some relationships between process signatures and part properties based on existing research but note that more investigation will need to take place.

Specifically in EBM, efforts for detecting process anomalies and the effect of process parameters are being made. Schwerdtfeger et. al.[42] show via the use of a LWIR camera that it was possible to detect inclusions in EBM parts based off correlation with thermal images captured during the build. The defects appear hotter to the camera in the thermal images, which they suggest is likely an effect of the increased emissivity of the cavity. With some image processing steps they are able to detect the size and shape of the defects and suggest that this data would be useful in a feedback system. If this data can be created in real-time, then the authors suggest that re-melting of the layer could occur for small defects and repeating the whole layer process for larger ones.

In two papers Cheng, Price, Lydon et. al.[43], [44] explore modelling of the EBM process and the speed factor process parameter, which are validated by the use of an NIR camera mounted on the machine. Accurate modelling of EBM and other AM processes could, in the future, lead to more accurate pre-processing of builds to create accurate parts first time. It could also allow further exploitation of AM processes with strategies and geometries not yet considered possible. However, because of the complex nature of AM processes, current models in development are restricted to specific features of AM builds. This model was used for investigating melt pool temperatures at different layer heights and the effect powder porosity has on the melt pool. Using the NIR camera Cheng et. al. were able to validate the melt pool temperature distributions from the model against builds in an Arcam S12. Via this method they found that the model was sufficient to predict melt pool sizes with an average error of 32% compared to those seen on the thermal camera. They also found that the powder porosity was a critical component in the model and that changing the porosity from 0.35 to 0.65 increased the peak melt pool temperature by 260 °C and size by 0.45 mm. This had previously not been a consideration in EBM but at least in simulation is shown to have a big effect on the process.

In their second paper[44] Price et. al. use the same NIR setup to investigate the speed factor (SF) parameter of the Arcams control system and compare it with an extension to the model discussed above. The SF parameter is a function of beam speed and current, so should therefore control the power being input into an area of a layer. Through the

investigation of building part with different speed factors they found many part properties that were affected. These included surface finishes and grain sizes within the material. The grain size can also be linked to the melt pool size and peak temperature changes seen with the different speed factors. Analysing these effects with the help of thermal imaging and modelling allowed the previous model to be developed to produce simulations that agreed with the data from the camera at different speed factors. This meant a relationship between the input parameter of speed factor and process signature of melt pool size and temperature could be developed. This had previously been an unknown due to the proprietary nature of Arcams build preparation and control algorithms. This kind of research can be developed into the relationships that Mani et.al discussed for linking specific input parameters with output part qualities.

Rodriguez et. al.[45] developed an LWIR camera system for use with EBM. They demonstrate their calibration process and experimental feedback mechanism to achieve uniform temperatures across the melted parts of a layer. This was done in an offline way by building the parts with a standard build theme and imaging each layer after the melt cycle had finished. The images were then analysed, and the build parameters modified to achieve more uniform temperatures in the next build. The effect of the grouping of parts was also investigated here, this added to the unevenness of the melt temperatures across all melted surfaces. By modifying the speed factor and beam current between builds the authors were able to reduce the temperature difference between parts in a group from 57 °C to 27 °C. With knowledge of other studies this variance in temperature across parts is likely to affect the part properties, specifically material microstructure. When using AM in a production environment, producing parts with consistent properties will be crucial. Initial experiments into the effect parts have on each other in a build like this begins to inform the types of feedback that will be necessary in future production ready AM processes.

Rodriguez et. al. also used a novel method of calibration for their thermal camera. Rather than calibrate the camera externally then compensate for the effects of the machine environment, the calibration was done in place. A cavity was created using the EBM machine that could be placed in the chamber and heated with the electron beam whilst being viewed by the camera. The shape of the cavity was designed to replicate an integrating sphere that may be used in a traditional calibration setup. This created a high emissivity area within the cameras field-of-view that could be used as a calibration point, with the temperature based off a thermocouple embedded in the cavity. This method will have corrected for some of the environment of the machine but not reflections from the heat shields or material emissivity.

In further work Rodriguez et. al.[46] continued with the calibration method working to obtain an absolute temperature within the EBM chamber. Here they considered the effect

of the heat shields and emissivity of the Ti-6Al-4V powder. Using thermocouple temperature measurements of the heat shields and calculating the view factors of the heat shield onto a region of interest, they were able to calculate the amount of energy seen by the camera from the heat shields. This allowed a correction to be made to the radiance value of the surface and remove the effect of the heat shield from the area. Emissivity was calculated by using the cavity described above with a known temperature from the heated cavity and the apparent temperature from the top surface of the cavity block. To verify the corrections being made to the IR camera data a thermocouple was melted into a block by mounting it protruding from the build plate. When comparing corrected temperature values from the camera to the thermocouple a  $< 0.3\%$  difference was seen.

Another calibration process for Inconel powder in EBM by Dinwiddie et. al.[47] used a built cavity to create a high emissivity area for an in situ camera to view. This took the form of a long cylindrical hole in an EBM built Inconel cube. Using the electron beam to heat the cube and embedded thermocouples to measure temperature, the authors were able to calculate an emissivity for the as built surface of the Inconel. This was based on the radiance seen by the camera from the high emissivity cavity and from an area of the top face of the cube. This measurement was also completed for powder surrounding the cube. The results gave a fixed emissivity for the powder and a linearly increasing emissivity with temperature for the as built surface. Emissivity correction for a material like Inconel will be required for accurate IR temperature measurement as its emissivity is known to fluctuate with both temperature and wavelength in traditional manufacturing processes. This method of calibration is useful in AM because geometries like this and the one above can be created easily. But, to be most useful they would need to be constructed as a part of build, to provide a real-time in scene high emissivity reference for an IR camera. This way parts of a build could be directly compared with the high emissivity temperature source. However, this would be challenging because of the environment and build process, for example; a contact temperature method would be needed close to the cavity at all times, but if it is embedded into a part the further away from the current layer it becomes the less accurate it will be.

### **2.4 Summary**

This chapter details the history, basic use cases and principles of infrared camera and additive manufacturing technologies. These two fields are brought together in this work where the recent advances in IR camera technology is put to use in an AM context. Infrared technology and specifically cameras have long been used in monitoring applications. The principles of IR detection and camera technology were key when designing and operating the instrument created in this work; informing decisions on technology selection as well as providing the background scientific theory for infrared signal to temperature conversion. Knowledge of AM processes also fed into the system

design and the development of uses and analysis methods for the system This relied on specific knowledge of the EBM process and its intricacies.

Finally, this chapter discussed the current commercial and academic work around process monitoring in AM. This sets the landscape in which this work was completed and shows the interest in the area from both industrial and academic points of view. The industry needs advances in monitoring technology to improve their products and AM has opened many new areas of scientific research. The development of new research focused instruments is the joining of the two and will lead to the improved monitoring the AM industry requires.

- [1] E. S. Barr, "The Infrared Pioneers-II," *Infrared Phys.*, vol. 2, no. 1842, pp. 67–73, 1962.
- [2] E. S. Barr, "The Infrared Pioneers-III," *Infrared Phys.*, vol. 3, pp. 195–206, 1963.
- [3] K. Tihanyi, "Improvements in television apparatus," GB313456, 1930.
- [4] L. Sipka, "Innovators and Innovations." *The Hungarian Quarterly*, p. 14, 2001.
- [5] A. Rogalski, "History of infrared detectors," *Opto-Electronics Rev.*, vol. 20, no. 3, 2012.
- [6] "AGA Museum." [Online]. Available: <http://www.aga-museum.nl/page/thermovision>. [Accessed: 12-Mar-2019].
- [7] J. A. Roux, "Applicability of Infrared Scanning Cameras for Thermal Vacuum Testing in the 12V and Mark I Chambers," Tennessee, 1975.
- [8] C. M. Hanson, H. R. Beratan, R. A. Owen, M. Corbin, and S. McKenney, "Uncooled thermal imaging at Texas Instruments," 1992, vol. 1735, p. 17.
- [9] P. Saunders and D. R. White, "Physical basis of interpolation equations for radiation thermometry," *Metrologia*, vol. 40, no. 4, pp. 195–203, Aug. 2003.
- [10] J. R. Willmott, D. Lowe, M. Broughton, B. S. White, and G. Machin, "Potential for improved radiation thermometry measurement uncertainty through implementing a primary scale in an industrial laboratory," *Meas. Sci. Technol.*, vol. 27, no. 9, p. 94002, 2016.
- [11] CCD Group, "An introduction to CCD operation." [Online]. Available: [https://www.mssl.ucl.ac.uk/www\\_detector/ccdgroup/opttheory/ccdoperation.html](https://www.mssl.ucl.ac.uk/www_detector/ccdgroup/opttheory/ccdoperation.html). [Accessed: 02-Feb-2019].
- [12] Edmund Optics, "Imaging Electronics 101: Understanding Camera Sensors for Machine Vision Applications." [Online]. Available: <https://www.edmundoptics.com/knowledge-center/application-notes/imaging/understanding-camera-sensors-for-machine-vision-applications/>. [Accessed: 02-Feb-2019].
- [13] ASTM International, "ISO/ASTM52900-15 Standard Terminology for Additive Manufacturing." ASTM International, West Conshohocken, PA, 2015.
- [14] T. Wohlers, "Rapid Prototyping, Tooling & Manufacturing State of the Industry," Colorado, 2005.
- [15] H. Kodama, "Automatic method for fabricating a three-dimensional plastic model with photo-hardening polymer," *Rev. Sci. Instrum.*, vol. 52, no. 11, pp. 1770–1773, Nov. 1981.
- [16] C. W. Hull, "Apparatus for production of three-dimensional objects by stereolithography," US4575330A, 08-Aug-1984.
- [17] FundingUniverse, "History of Stratasys, Inc." [Online]. Available: <http://www.fundinguniverse.com/company-histories/stratasys-inc-history/>. [Accessed: 29-Sep-2019].
- [18] T. Wohlers and T. Gornet, "History of Additive Manufacturing," *Wohlers Rep. 2014 - 3D Print. Addit. Manuf. State Ind.*, pp. 1–34, 2014.

- [19] EOS, "30 years of EOS." [Online]. Available: <https://30years.eos.info/en>. [Accessed: 29-Sep-2019].
- [20] Arcam AB, "History - Arcam AB." [Online]. Available: <http://www.arcam.com/company/about-arcam/history/>. [Accessed: 29-Sep-2019].
- [21] W. Meiners, K. Wissenbach, and A. Gasser, "Shaped body especially prototype or replacement part production," DE19649865C1, 02-Dec-1996.
- [22] R. Jones *et al.*, "RepRap – the replicating rapid prototyper," *Robotica*, vol. 29, no. 1, pp. 177–191, Jan. 2011.
- [23] E. Herderick, "Additive manufacturing of metals: A review," in *Materials Science and Technology Conference and Exhibition 2011, MS and T'11*, 2011, vol. 2, pp. 1413–1425.
- [24] Davide Sher, "The global additive manufacturing market 2018 is worth \$9.3 billion - 3D Printing Media Network," *3D Printing Media Network*, 2018. [Online]. Available: <https://www.3dprintingmedia.network/the-global-additive-manufacturing-market-2018-is-worth-9-3-billion/>. [Accessed: 01-Oct-2019].
- [25] Loughborough University, "The 7 categories of Additive Manufacturing | Additive Manufacturing Research Group." [Online]. Available: <https://www.lboro.ac.uk/research/amrg/about/the7categoriesofadditivemanufacturing/>. [Accessed: 16-May-2020].
- [26] Optomec Inc, "3D Printed Electronics - Aerosol Jet Technology - Optomec." [Online]. Available: <https://www.optomec.com/printed-electronics/aerosol-jet-technology/>. [Accessed: 05-Oct-2019].
- [27] HP Development Company, "HP Industrial 3D Printers - Leading The Commercial 3D Printing Revolution | HP® Official Site." [Online]. Available: <https://www8.hp.com/us/en/printers/3d-printers.html>. [Accessed: 05-Oct-2019].
- [28] Loughborough University, "Sheet Lamination - Additive Manufacturing Research Group." [Online]. Available: <https://www.lboro.ac.uk/research/amrg/about/the7categoriesofadditivemanufacturing/sheetlamination/>. [Accessed: 10-May-2020].
- [29] S. C. Joshi and A. A. Sheikh, "3D printing in aerospace and its long-term sustainability," *Virtual Phys. Prototyp.*, vol. 10, no. 4, pp. 175–185, 2015.
- [30] P. D. Olson, "100,000 Patients Later, The 3D-Printed Hip Is A Decade Old And Going Strong," *GE Reports*, 05-Mar-2018. [Online]. Available: <https://www.ge.com/reports/100000-patients-later-3d-printed-hip-decade-old-going-strong/>. [Accessed: 06-Oct-2019].
- [31] W. L. Ng *et al.*, "Vat polymerization-based bioprinting—process, materials, applications and regulatory challenges," *Biofabrication*, vol. 12, no. 2, p. 022001, Feb. 2020.
- [32] G. Bi and A. Gasser, "Restoration of nickel-base turbine blade knife-edges with controlled laser aided additive manufacturing," in *Physics Procedia*, 2011, vol. 12, no. PART 1, pp. 402–409.
- [33] Aconity GmbH, "Equipment - Aconity3d." [Online]. Available: <https://aconity3d.com/equipment/>. [Accessed: 26-Oct-2019].

- [34] Arcam AB, "Arcam - Additive Manufacturing solutions for the production of orthopedic implants," 2017.
- [35] T. Toepfel *et al.*, "3D analysis in laser beam melting based on real-time process monitoring," in *Materials Science and Technology Conference and Exhibition 2016, MS and T 2016*, 2016, vol. 1, pp. 123–132.
- [36] G. Tapia and A. Elwany, "A Review on Process Monitoring and Control in Metal-Based Additive Manufacturing," *J. Manuf. Sci. Eng.*, vol. 136, no. 6, p. 060801, 2014.
- [37] S. K. Everton, M. Hirsch, P. Stravroulakis, R. K. Leach, and A. T. Clare, "Review of in-situ process monitoring and in-situ metrology for metal additive manufacturing," *Mater. Des.*, vol. 95, pp. 431–445, Apr. 2016.
- [38] K. Jurrens and Energetics Incorporated, "Measurement Science Roadmap for Metal-Based Additive Manufacturing," *Addit. Manuf.*, p. 86, 2013.
- [39] B. Lane and E. P. Whintont, "Calibration and Measurement Procedures for a High Magnification Thermal Camera," *Natl. Inst. Stand. Technol.*, 2015.
- [40] M. Mani, B. M. Lane, M. A. Donmez, S. C. Feng, and S. P. Moylan, "A review on measurement science needs for real-time control of additive manufacturing metal powder bed fusion processes," *Int. J. Prod. Res.*, vol. 55, no. 5, pp. 1400–1418, 2017.
- [41] Y. Ning, Y. S. Wong, J. Y. H. Fuh, and H. T. Loh, "An approach to minimize build errors in direct metal laser sintering," *IEEE Trans. Autom. Sci. Eng.*, vol. 3, no. 1, pp. 73–80, 2006.
- [42] J. Schwerdtfeger, R. F. Singer, and C. Körner, "In situ flaw detection by IR-imaging during electron beam melting," *Rapid Prototyp. J.*, vol. 18, no. 4, pp. 259–263, Jun. 2012.
- [43] B. Cheng, S. Price, J. Lydon, K. Cooper, and K. Chou, "On Process Temperature in Powder-Bed Electron Beam Additive Manufacturing: Model Development and Validation," *J. Manuf. Sci. Eng.*, vol. 136, no. 6, p. 061018, 2014.
- [44] S. Price, B. Cheng, J. Lydon, K. Cooper, and K. Chou, "On Process Temperature in Powder-Bed Electron Beam Additive Manufacturing: Process Parameter Effects," *J. Manuf. Sci. Eng.*, vol. 136, no. 6, p. 061019, 2014.
- [45] E. Rodriguez *et al.*, "Integration of a thermal imaging feedback control system in electron beam melting," *23rd Annu. Int. Solid Free. Fabr. Symp. Addit. Manuf. Conf.*, no. Figure 1, pp. 945–961, 2012.
- [46] E. Rodriguez, J. Mireles, C. A. Terrazas, D. Espalin, M. A. Perez, and R. B. Wicker, "Approximation of absolute surface temperature measurements of powder bed fusion additive manufacturing technology using in situ infrared thermography," *Addit. Manuf.*, vol. 5, pp. 31–39, 2015.
- [47] R. B. Dinwiddie, M. M. Kirka, P. D. Lloyd, R. R. Dehoff, L. E. Lowe, and G. S. Marlow, "Calibrating IR cameras for in-situ temperature measurement during the electron beam melt processing of Inconel 718 and Ti-Al6-V4," p. 986107, 2016.

### 3 Camera System Design and Calibration for Arcam EBM Imaging

#### 3.1 Introduction

This chapter details the design and calibration of a thermal imaging camera system for use on an Arcam S12 Electron Beam Melting (EBM) Additive Manufacturing (AM) machine. This will involve camera selection, an overview of the lens design and moving onto the implementation of the system and its calibration. The capabilities of the system will also be demonstrated with some initial investigations which will be continued in later chapters.

#### 3.2 Camera and Technology Selection

The first step to creating a system for EBM monitoring was to select an imaging technology. Working in the infrared wavelengths and with the different IR wavelength bands, as discussed earlier, each band has different detection technologies. Each technology is suited for detection of different temperature ranges, this is because different temperatures have a different peak emission wavelength as defined by Wiens Law. As the temperature gets higher the peak emission wavelength gets lower; meaning shorter wavelength detectors are more suited to detection of high temperatures and vice versa.

When selecting a technology, and therefore wavelength band, to work with for this application the identification of the temperature range required was crucial. Two known temperature points from the EBM process are the preheat temperature of 450 – 600 °C and the melting point of the commonly used Ti-6Al-4V powder of ~1600 °C[1]. Using Wiens Law to calculate the peak wavelength of the blackbody emission for these two temperatures (Table 3.1), shows that that the peak wavelengths lie in the short to mid wavelength IR ranges. This would suggest a short or mid wavelength IR camera would be best here. However, there was more to consider than just the peak emission wavelength, each detection technology has different advantages.

**Table 3.1 Temperature points of interest from the EBM process and their peak blackbody emission wavelengths**

	Temperature / °C	Peak wavelength of emission / $\mu\text{m}$
Preheat	450	4
Preheat	600	3.32
Ti-6AL-4V Melting point	1600	1.55

The blackbody spectra of these temperatures are a starting point for deciding which technologies would be suitable for the application. However, they show a broad spectrum (Figure 3.1) for all temperatures; where any of the common technologies would work.

Therefore, the technology can be selected on the advantages it would bring to the EBM monitoring application. Acquisition speed is one such advantage that would be useful for EBM monitoring; the beam speed of the S12 is quoted as >1000 m/s [2]. This means to be

able to acquire clear images of the melt pool a low exposure time was required and ideally a high frame rate to match. Both of these parameters depended on the detector technology; SWIR or MWIR is likely to provide sufficient signal levels at the low temperatures and allow shorter exposure times to be used. However, the readout speeds from these technologies are slower than NIR because of less advanced electronics, meaning higher frame rates from NIR.

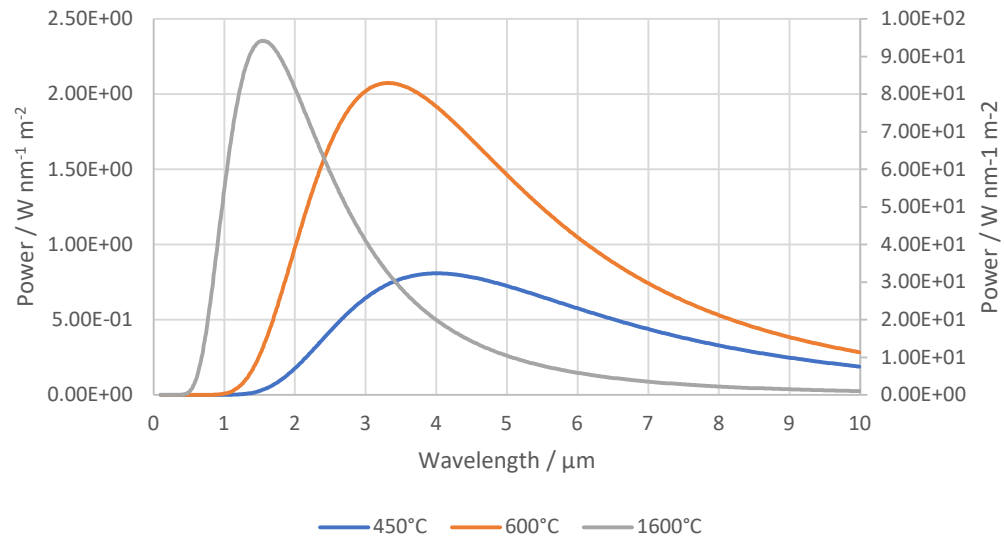


**Figure 3.1 Blackbody spectra for 450 °C, 600 °C and 1600 °C (1600 °C shown on secondary axis)**

Another feature that differed between technologies is available resolutions. High resolution was key in this application because the system will be mounted to view the build platform as a whole, opposed to just the melt pool as is common in laser systems. The main reason for this is that with the Arcam using an electron beam there are no traditional optics in the beam path that could be used to mount a system coaxially with the beam. This is in comparison to Laser Powder Bed Fusion (LPBF) systems where optical elements that are used to focus and steer the laser can also be used by a camera for monitoring. To achieve similar levels of detail around the melt pool, which is likely to be an area of interest, a high-resolution imager was required. NIR cameras are available with higher resolutions than SWIR and MWIR devices. This is because NIR cameras use silicon focal plane arrays (FPAs); which are a much more mature technology compared to InGaAs (SWIR) or InSb (MWIR), because of their use in visible light cameras. The development around silicon detector technology has driven the resolution and frame rates up and noise levels down.

The 2 key factors of speed and resolution as well as readout noise, cost, availability and others made a silicon NIR imager a good fit for this application. There may be a slight trade off in signal levels, especially at the lower temperatures compared to SWIR or MWIR technologies but the superior speed, resolution and lower cost will be more beneficial. A

silicon based camera will be trialled to confirm the trade-offs before making the decision to choose NIR over SWIR or MWIR.

### 3.2.1 Silicon Camera Experiment

To perform a trial of a silicon camera on the EBM process a Sony SSC-M188CE security camera was repurposed. This device is an analogue video security camera containing a PAL resolution (500 x 582 pixels after digital conversion) Sony ICX405AL silicon FPA. The sensor is optimised for visible wavelengths, but the responsivity curve shows it is still responsive to wavelengths up to 1  $\mu\text{m}$  although at a low efficiency (Figure 3.2). Newer sensors are likely to be more efficient overall and some have been designed to have enhanced response at NIR wavelengths, so this will be representative of silicon, but better performance can be expected from a more recent and mature FPA technology[3].

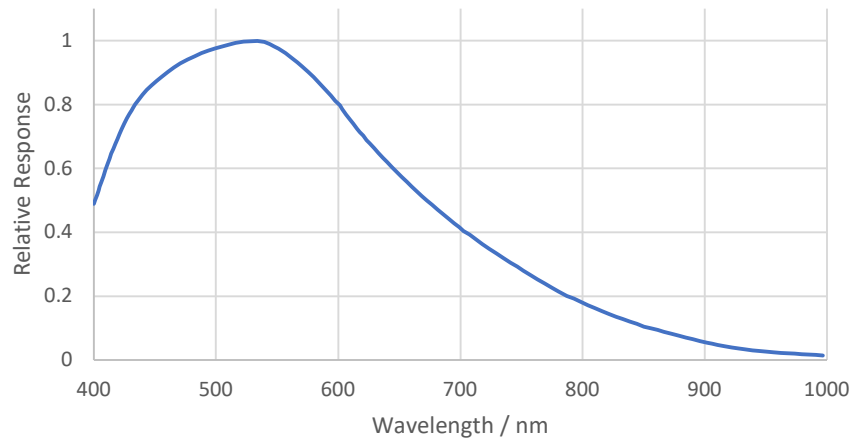


Figure 3.2 Sony ICX405AL responsivity curve

A digitiser from The Imaging Source was used to capture the analogue output of the camera and create an 8-bit digital signal at a resolution of 500 x 582 pixels and 25 Hz[4]. This is not ideal, especially being only an 8-bit signal because a system with a higher bit depth readout was eventually selected to achieve higher resolution temperature readings and wider ranges as is detailed in section 3.2.2. This data was enough for proof of concept on a silicon based system though. Using the capture devices SDK, a piece of software was written to provide basic camera functionality and also real-time temperature conversion and false colouring for easy viewing of the data.

With silicon sensors being most sensitive in the visible wavelengths, a filter needed to be fitted to the camera so only NIR wavelengths were detected and temperature could be measured. For simplicity and to maximise the signal available from the low efficiency NIR end of the camera's responsivity curve an 850 nm long pass filter was used. This was mounted behind the lens directly in front of the sensor. A lens with an electronically

variable aperture was used to provide some signal level control because the exposure time or gain could not be controlled on the camera.

Using a fixed aperture size the camera was calibrated to a temperature range of 600 – 825°C. This temperature range was within the preheat range of an EBM build. A single point calibration using Planck’s Law was planned however this was not possible because there were too many unknowns associated with the camera because it was not designed for this use. For example, optical throughput and any signal conditioning done in the camera; like auto brightness or pixel correction. Instead the camera was set to view the opening of a blackbody calibration furnace and a series of average pixel values were recorded for a range of temperatures. A curve was then fit to map from pixel value to temperature based on these measurements (Figure 3.3).

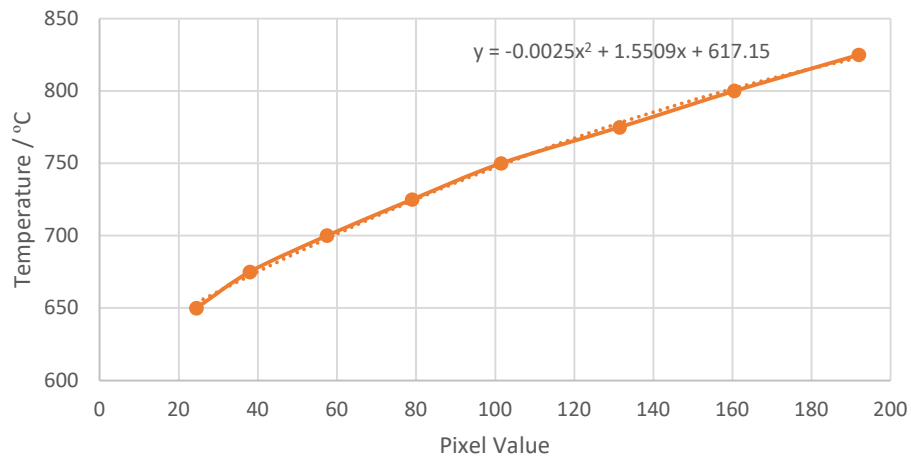


**Figure 3.3 Sony camera calibration curve**

The camera was tested by mounting it on the Arcam in place of the inspection camera on top of the build chamber. This location gave the best view of all the available ports into the chamber; allowing the full build plate to be seen without any obstruction and for the camera to be as perpendicular to the build plate as possible. When a build was started and the camera running on the preheat stages it was immediately obvious that there was more NIR radiation than expected. The camera saturated even at low temperatures according to the build plate thermocouples. This can be seen in Figure 3.4, where the orange circle in the image is the build plate and reads 191 DLs, the level at which this setup saturated.

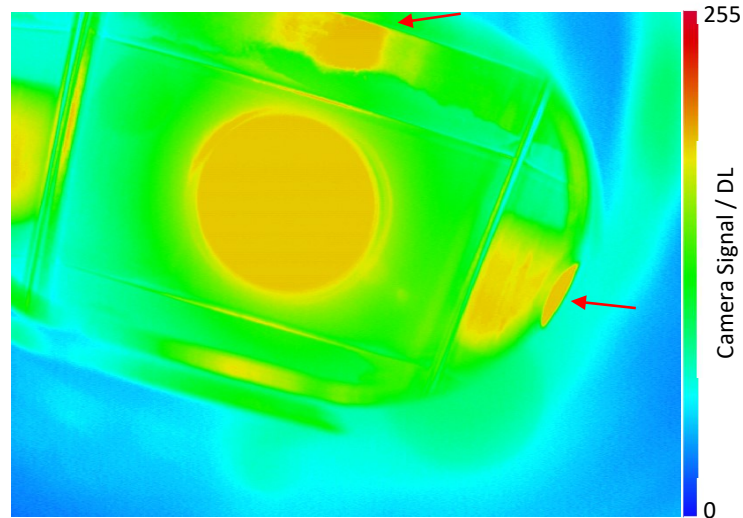


**Figure 3.4 Sony camera test during preheat stages of the build. The build plate is saturated despite only being  $\sim 500$  °C. Reflections from the heat shield can also be seen (visible reflections marked with arrows)**

The levels of saturation at much lower temperatures ( $\sim 500$  °C in the image) than seen in the calibration were unexpected but were a promising sign for the use of a silicon camera, as long as they can be explained. They show that more energy is being received by the camera than from the blackbody furnace. A likely explanation for this, and one that can be seen in Figure 3.4, is reflections from the heatshields that sit around the build plate. The heat shields are necessary for the EBM process to keep the build area at a high temperature without constant energy input and are designed to reflect heat back down onto the build plate. This would make the build plate appear hotter than it is because the camera will detect the reflected radiation as well as the emission from plate itself.

To continue with the test the voltage on the aperture of the cameras lens was adjusted to close the aperture more and further images were treated as radiance images. This means the images can only show relative changes in temperature, relative to the coldest object in frame. Therefore, no temperature information could be determined from the rest of the images, but they did give an idea of what could be seen of the EBM process with a silicon imager of this resolution. This was good enough for testing because the biggest problem was likely to be low signal, which was already ruled out. The two images in Figure 3.5 were taken after the aperture was reduced in size and show two different parts of the build; Figure 3.5.A is still in the preheat stage but here the scan lines of the electron beam are visible as they raster across the build plate. Figure 3.5.B shows the contour stage where the outside edges of the part are melted. Here multiple saturated melt pools can be seen because of the relatively long exposure time of the camera and the persistence of vision effect. This image is particularly interesting because it is representative of the kind of images expected from the real system. From images like this lots of different analysis could occur, melt pools could be tracked, part geometries segmented from the image and more.

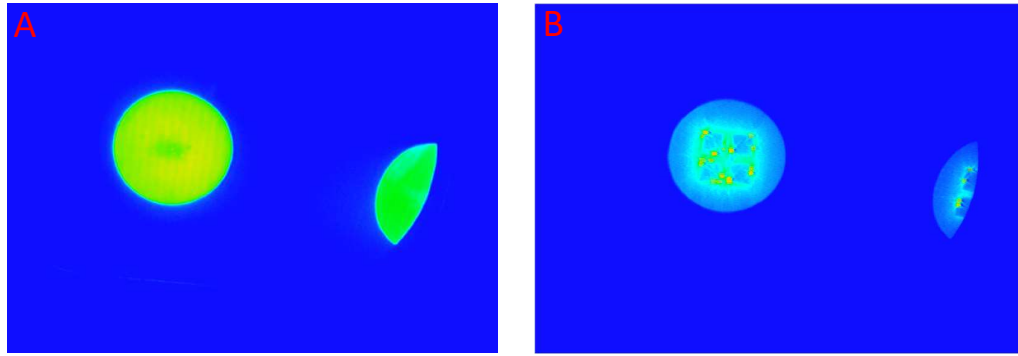


**Figure 3.5 A. Build plate showing electron beam scan lines. B. First layer of build showing contouring build step.**

Although no radiometric images were obtained from the trail of the silicon camera the test was considered successful. It was proven that even with an older, less efficient sensor the signal levels were high enough to provide good contrast from the cold background at least. Also, even at the relatively low resolution of this camera and with a small build area features of the build could be identified. These were the main aims for the test, but it has also shown some of the difficulties that will need to be addressed with the final system. The biggest one identified here is stray radiation and reflections from inside the build chamber, this will have been made worse in the test by the non-optimal optics and mounting used, but it will still be present even if these are addressed.

### 3.2.2 Final Camera Selection

With the success of the silicon camera trial the decision was made to use a silicon camera for the final system. This will allow the system to take advantage of the more mature silicon CMOS technology compared to InGaAs or InSb for example. As mentioned in the previous section the application takes advantage of the higher resolutions and faster acquisition rates of this technology.

Cameras with scientific CMOS (sCMOS) FPAs were rating highly when comparing near infrared camera models[5]–[7]. The sCMOS branding is a sign the FPA has been optimised for radiometric used, whether it be in the NIR or visible wavelengths. It signifies the cameras FPA and readout electronics have been designed with low noise and repeatability in mind. The FPAs in these cameras often also have enhanced responsivity outside of the visible wavelength range. They are often marketed at life science applications for high resolution, low noise microscopy[8]. However, with enhanced responsivity in the NIR they were also a very good fit for this application.

As an example of the of the benefits an sCMOS sensor will bring to an NIR imaging application like this, Figure 3.6 shows the comparison between two Hamamatsu FPAs responsivity curves[5], [8]. The CMOS FPA is quoted as having much wider wavelength

response but the sCMOS's quantum efficiency is more than double the CMOS's at wavelengths longer than visible wavelengths.

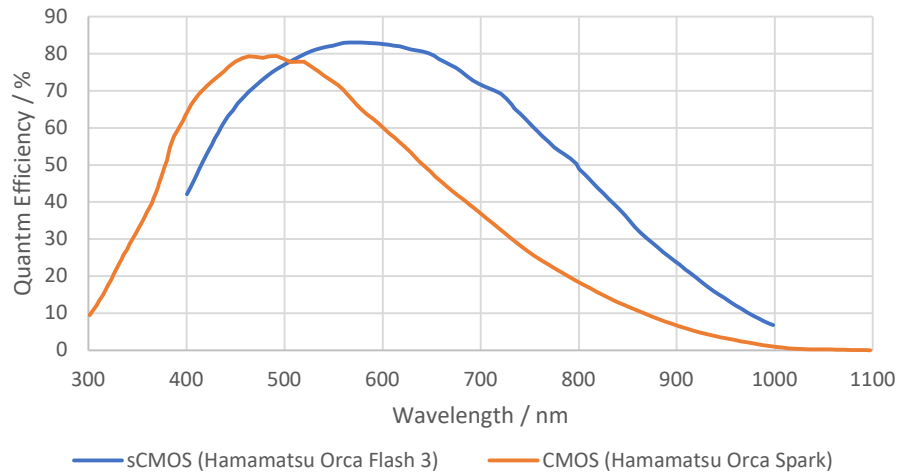


**Figure 3.6 Comparison between sCMOS and CMOS responsivity**

A factor that was important when considering any camera was the bit depth of the sensor/readout electronics. This is the maximum number of digital levels (DLs) that can be read from a single pixel and therefore defines the resolution of the intensity measurement. In this application it then maps to the available temperature resolution. This means the higher the bit depth of the camera the higher resolution temperature measurements can potentially be made. However, because the relationship between temperature and intensity is nonlinear it will also affect the range of temperatures that can be measured at a given wavelength with a given exposure time. For example, if a maximum change in temperature of 5 °C/DL allowed (minimum temperature resolution of the camera), the dynamic range will be much larger for a 16-bit camera compared to an 8-bit camera. This is calculated using Planck's law with a scaling factor to scale to DLs and is shown in Figure 3.7 below.

Using the ranges seen for each bit depth in Figure 3.7 as a guide it was clear that a high bit depth camera was necessary to achieve the temperature ranges required. Ideally a single exposure time would be able to capture the whole range from preheat to melt, however, this was likely be challenging and would sacrifice temperature resolution. But it was acceptable to get close to the full range and be able to adjust the exposure time to focus on the extreme high or low areas as required.

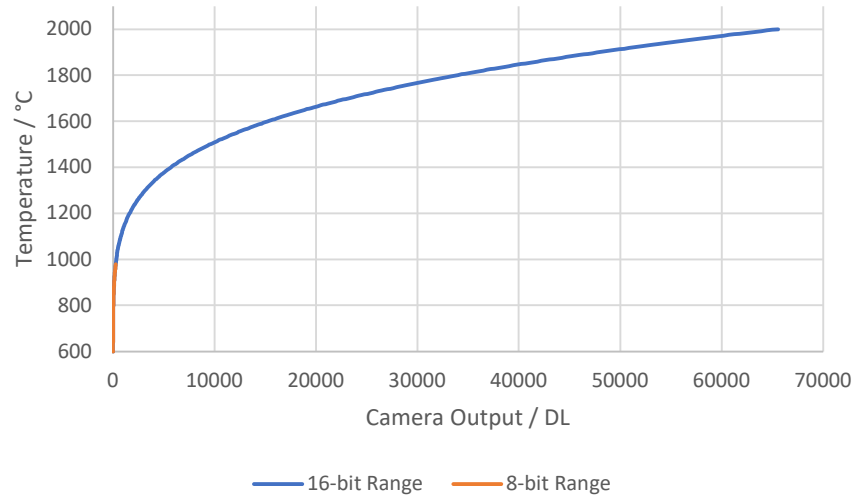


**Figure 3.7 Camera bit depth comparison, showing the temperature ranges of 8 and 16 bit cameras**

Based predominantly on the factors presented in the last sections the decision was made to use a Hamamatsu Orca Flash 4 V2 C11440-22CU[6] camera. This is a 4 megapixel, 16-bit sCMOS camera, its key parameters are summarised in Table 3.2.

**Table 3.2 Hamamatsu C1140-22CU Key Specifications**

Hamamatsu C11440-22CU Key Specifications	
Sensor Technology	Scientific CMOS
Resolution	2048x2048
Pixel Pitch	6.5 $\mu\text{m}$
Frame Rate	100 fps at full resolution 25655 fps at 2048x8 resolution
Sensor Bit Depth	16-bit
Exposure Time Range	1 ms to 10s at full resolution 38.96 $\mu\text{s}$ to 10s with sub array

The C11440-22CU was a good choice because it takes advantage of sCMOS technology. This brought with it the benefits of high resolution and high bit depth, as well as wide exposure time ranges and a variable readout window. The variable sub array size allows higher frame rate imaging that would normally be associated with more expensive and less sensitive (in terms of wavelengths and QE in the NIR) cameras. This allowed high speed melt pool imaging whilst also having the capability to image the full bed.

### 3.3 Imaging System Design

The design of the imaging system needed to fit within the existing Arcam enclosure, with minimal modifications. This was a physical design constraint meaning a custom lens was required. However, this would likely have always been the case because mounting positions on the machine and space near any ports in the vacuum chamber was limited.

Using an off-the-shelf lens would have been bulky and may have not been optimal for the system. This was because the field-of-view needed to be relatively narrow to make the most of the resolution when mapped to the build plate. Also, if using an off-the-shelf lens, it would not be optimised for the correct wavelengths which could cause more distortion and reflections than a lens designed to work in the NIR.

The same port in the vacuum chamber was used as when performing the tests with the Sony camera. This was the port where the existing inspection camera was mounted, proving there was a good view of the build plate and space on the outside of the chamber. It is also the port closest to being perpendicular to the build plate. Ideally the camera would be mounted perpendicular and centred relative to the build plate however, because of the electron gun column this is not possible. Having the port as close to perpendicular as possible will minimise the skew of the image and reduce the effect of reflections from the heat shield panels.

With the location and the required field-of-view known a custom lens could be designed. A borescope style lens was designed to account for the small space and mounting difficulty of the camera in the machine. This is a long thin multi element lens that was able to allow the camera to mount away from the port on a shelf in the machine enclosure. The borescope design consisted of eleven lenses and a mirror, four of the lenses were custom designed, with the remainder acquired from a catalogue supplier. The design was completed by another member of the group, C. Zhu, and is shown in Figure 3.8. The borescope had an f number of 6 and a field-of-view covering 230 mm in diameter. The design consisted of an outer housing which held the lenses, with the lenses separated by sections of lens tube according to the spacing required by the design. The assembled borescope with its side cover removed is shown in Figure 3.9.

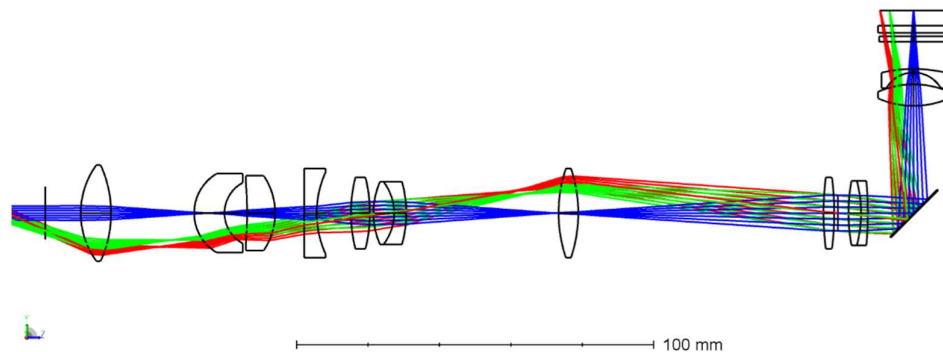


**Figure 3.8 Borecope optical design showing 3 chief rays propogating through the optical system, from input (left) to camera sensor (top right)**



**Figure 3.9 Assembled borescope (shown in the same orientation as optical design above)**

The borescope was angled approximately  $20^\circ$  from vertical, with some adjustment, and the 230 mm diameter field-of-view allowed the whole build plate to be visible in frame with the focal point set at the centre of the build plate. With a 400 mm working distance the effective pixel radius on the build plate was  $66\ \mu\text{m}$  at the centre, increasing to a maximum of  $79\ \mu\text{m}$  at the furthest point from centre. All the elements in the borescope were antireflective coated for the NIR wavelengths.

To accommodate the borescope design a modified mount was created for the vacuum chamber. This needed to include a film feed system and a mounting point for the windows into the vacuum chamber. These were crucial elements of the existing mount and made imaging of the process possible. The chamber window was the element which sealed against an O-ring on the outer chamber wall and made pulling a vacuum in the chamber possible with the camera mounted. The glass used in the window was leaded glass and was used to block x-rays generated in the process by the high energy impacts of the electron beam into the powdered metal. With the system mounted on the machine the window was directly in front of the lens, therefore it needed to be optically characterised to account for any transmission losses. This was done using a monochromator to obtain a transmission curve across a wavelength range of 700-1300 nm (Figure 3.10). This was a wider range than the camera was operating at, but it was done to get an understanding of the effect it would have across the NIR wavelengths. The camera works within the 850-1100 nm range and as can be seen in Figure 3.10 the leaded glass has a transmission of approximately 0.91 over this range. The flatness of the transmission in this region was useful as it could be considered constant in any later calibrations. The transmission of the window in the NIR is also much higher than the MIR as found by Dinwiddie et al. [9] using a 3-5  $\mu\text{m}$  camera only saw a transmission value of 0.0108 over that range.

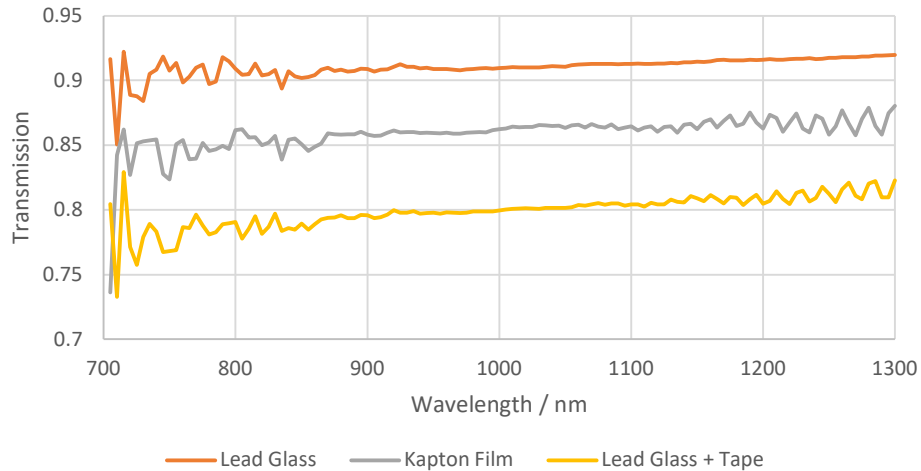


**Figure 3.10** Leaded glass window and Kapton film transmission spectrums

The film feed system protected the window from metallisation caused by the process. It does this by feeding a strip of Kapton film across the leaded glass window on the inside of the chamber. This way any metal released from the melting process settles on the film which can be advanced to keep the window clean for the camera. This would be a problem because the metallisation of the window caused its transmission to change and affect the amount of energy reaching the camera. This would lead to a lower temperature reading without any correction. This whole part of the mounting system even though being outside the chamber is under vacuum so the film can be fed through to the process side of the window. This meant special attention needed to be paid to the redesign of this part when accommodating the borescope. All the mating surfaces were precision machined and polished to make good vacuum seals. The design allowed the camera and borescope to be removed and positioned with the machine under vacuum, which was needed to allow proper alignment. Because the Kapton film was also in the optical path it was analysed for transmission in the same way as the window. Like the window the transmission was flat across the region of interest in the NIR and the overall transmission of the window and film was approximately 0.8 as shown in Figure 3.10.

The high level of transmission of both the leaded glass and film made it possible to use this system continuously throughout the process. This has not been possible for other systems where longer wavelength cameras have been used [9], but their advantage in the amount of energy available to those wavelengths was negated somewhat by the transmission of the window. Other methods of keeping the window clean have also been used such as using a shutter [10] but this prevents continuous imaging of the process, which is especially useful when trying to get insight into the metallurgical properties of parts during a build.

The last part of the system to be modified to accept the borescope was the mounting flange on the camera. The borescope was not designed with a standard C-mount fitting for camera mounting because this would have made it difficult to mount the camera in situ, and also meant there would be a need for other mechanical components in the lens to allow for focusing. Instead the lens was made fixed focus with a square mounting piece on the back, a corresponding flange was machined for the camera to accept this. Because there was no thread on the mounting piece the camera could be smoothly adjusted in relation to the back of the lens to focus the image. The camera could then be locked in place using set screws. The full system is shown in Figure 3.11 and Figure 3.12 mounted in place on the Arcam.



Figure 3.11 Final camera system with borescope mounted to camera

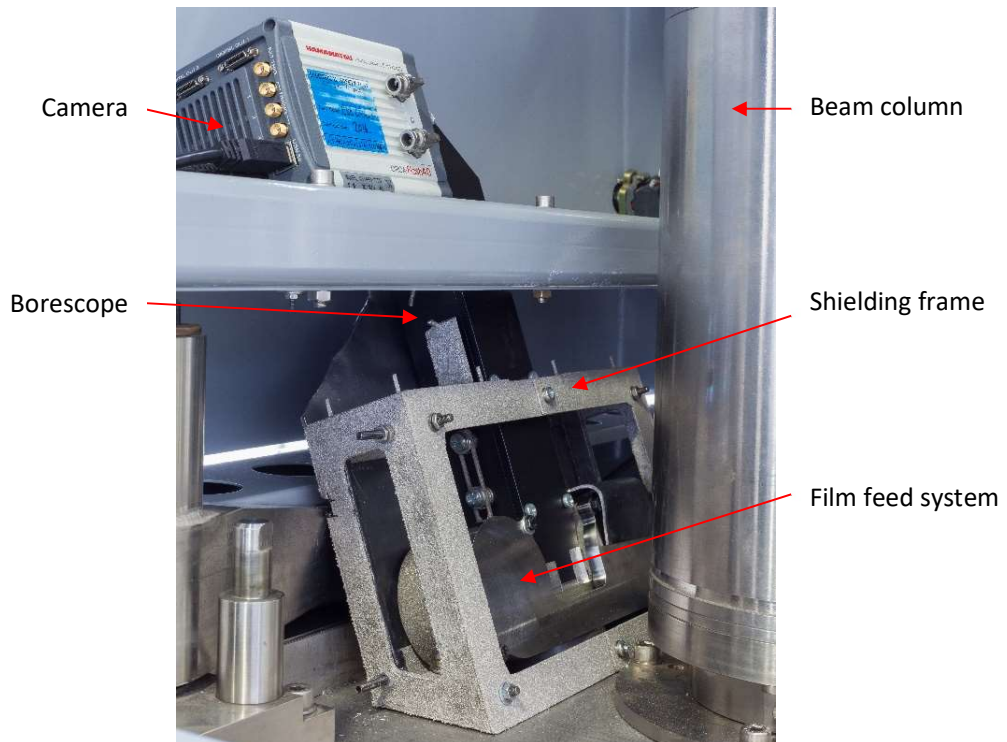


Figure 3.12 Camera system fitted to Arcam S12

### **3.4 Calibration**

With the final lens designed and manufactured the calibration and characterisation of the system could be started. A thorough characterisation of the camera system was needed as a starting point to learn about the environment in the Arcam and therefore make accurate temperature measurements of the process. The calibration and characterisation procedures for a single point infrared thermometer (IRT) were used as a base for this process. Some of the procedures and measures of accuracy for an IRT are not directly transferable to an FPA based system, however, they provide a good starting point and a method of comparison with existing instruments.

#### **3.4.1 Temperature Calibration**

The temperature calibration process was based on IRT calibration methods. For any instrument a calibration process is the process of defining how the instrument performs compared to a standard or theoretical model. For an IRT, or any IR temperature measurement device, this is no different; the calibration is the process of defining how the instrument responds to an ideal blackbody input[11]. From this a model can be used to interpolate between calibration points and create a model of the instrument that can be used to convert signal into temperature. This was the process used here, a combination of theoretical models and practical measurements were used to define the conversion model for the camera, as well as other parameters.

##### **3.4.1.1 Setup and Method**

The calibration process relies on a known standard of IR radiation or an instrument to provide calibrated measurements of an IR source for comparison. In this case the process is based upon a transfer standard R-type thermocouple (Isotech milliK thermometer[12] and UKAS calibrated thermocouple[13]) and a blackbody calibration tube furnace (Land Instruments LandCal P1200B[14]). Using the milliK and calibrated thermocouple as a transfer standard the P1200B furnace could be used as a source to calibrate the camera against. This is a common method used for industrial calibration where using primary or secondary temperature standard sources is impractical.

This combination of equipment provides a measurement traceable back to a standard source via the UKAS calibrated thermocouple. The camera was placed in front of the furnace aperture at 400 mm to replicate the working distance of the system in situ and to focus the camera at the correct distance. The thermocouple was placed in the furnace's calibration port, this placed the end of the thermocouple directly in contact with (and surrounded by) the back of the metal target of the tube furnace. This cavity is assumed to be isothermal and at the same temperature as the furnace target. This gives an accurate measure of the temperature being measured by the camera observing the front side of the target along the tube of the furnace. The setup is shown in Figure 3.13.

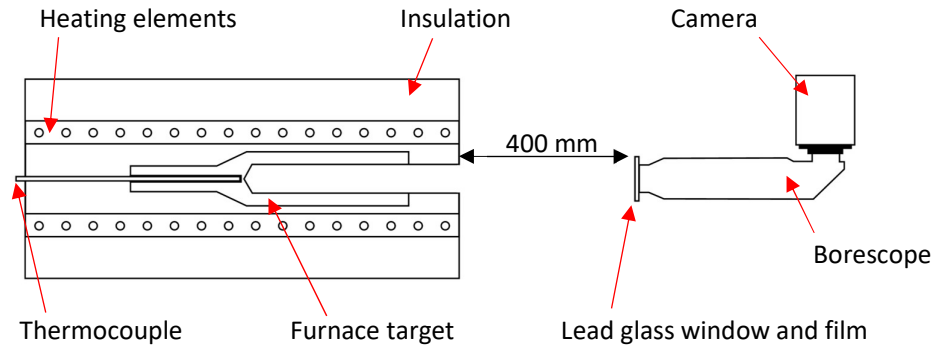


**Figure 3.13 Calibration setup diagram, showing cross section of furnace and camera system position**

Using this setup images can be captured with the camera to be used as calibration images. When capturing calibration images, the lead glass and Kapton film were placed in front of the borescope to allow the calibration to account for transmission of the materials. The centre of the borescope lens is aligned coaxially with the aperture of the furnace. This is not how the camera viewed the bed when in situ on the Arcam, but for calibration it is required to minimise the view of the tube walls in the measurement and maximise the view of the target. If the tube walls are visible in the measurement spot it can change the effective emissivity of the furnace, adding error to the measurement. The measurement position used for calibration was the pixel in the centre of the furnace aperture as defined by the bright circle of the furnace aperture on the calibration image.

Calibration points were taken between 450 °C and 1200 °C using the setup described above. This is not an ideal temperature range for calibration because the process being imaged will contain temperatures above this (the melting point of Ti-6Al-4V at ~1600 °C and beyond). However, this was the highest temperature achievable with this calibration setup that will produce a traceable measurement. For higher temperature values the model was used for extrapolation, this can be done because of the known linear response of silicon to increased incident radiation[15].

To collect a dataset for calibration the camera and thermocouple were setup as described above. The furnace was then set to heat to the desired temperature setpoint, once this was reached and the initial instability had settled the furnace was left for 90 minutes to settle. This settling time is to ensure a constant temperature over the measurement period. According to the furnace specifications, and previous testing using the milliK, 90 minutes is suitable for the furnace to settle to a temperature change within  $\pm 0.2$  °C over an hour. After 90 minutes 100 images were captured sequentially using HCLImage (the manufacturer provided capture software) and saved to provide the dataset for that temperature point. At the same time as the capture the temperature from the milliK was

logged to act as the temperature datapoint. This was repeated for multiple exposure times for each temperature.

To process a dataset a dark image was first subtracted from each image. This is done to remove any constant signal introduced by the camera from the images. Using a dark image versus using a fixed dark offset value accounts for fixed pattern noise/offset on the image sensor which could lead to certain pixels having a higher or lower dark value compared to those around it. A dark image is captured by blocking all light sources from entering the lens. CMOS cameras, especially sCMOS have a lot less fixed pattern noise/offset compared to the older CCD technology[16]. However, a dark signal still exists so correcting for it in this way corrected for both problems. A set of dark images were collected for each exposure time, and a mean image created from the 100 image set.

After the mean dark image had been subtracted from each image a mean image is created of the dataset. This is done to lessen the effect of noise on the calibration point. From the mean image the centre of the furnace aperture is found in the frame. This was done using row and column profiles to find the row and column with the largest number of consecutive pixels over a threshold. Given the aperture was circular the row and column found by this method was the centreline of the aperture horizontally and vertically. Therefore, the intersection of these two lines is the centre of the aperture. The pixel value from the mean image at the intersection was then recorded as the single datapoint to be used in the calibration. If multiple rows or columns were found using this method the one closest to the centre of the frame was used if there were an even number returned and the middle one used if an odd number were returned.

Once this process has been completed for the dataset at every temperature point a model is fit to interpolate the data and create a DL to temperature calibration curve. The Sakuma Hattori method[17] is used to do this. This method was developed to work with a single point silicon detector; however, it still applies to a camera where the output from the device is measured in DL rather than photocurrent (A/W). The inverse of the Planckian form of the equation is used here (3.1), making temperature the output. An unconstrained fit is used to optimise the fitting parameters and produce the calibration equation. From this a lookup table is produced evaluating the equation for all the possible signal values (100-65535). A minimum value of 100 is used here as the average dark value, this value is defined by the manufacturer and also verified during the calibration.

$$T = \frac{c_2}{A \ln\left(\frac{C}{C_0} + 1\right)} - \frac{B}{A} \quad 3.1$$

Where:

$c_2$  is the second radiation constant  
 $A, B$  and  $C$  are fit parameters  
 $C_0$  is camera signal

### 3.4.1.2 Filter Selection

Filter selection for the system was crucial to maximise the detectable temperature range of the system. Initially an 850 nm long pass filter was used to produce a calibration curve. The 850 nm filter, like the experiments earlier with the Sony camera, was used to evaluate the responsivity of the detector in the NIR and the environment in the Arcam. A much higher level of signal was found with this testing, leading to a maximum temperature range of 526 – 998 °C when using the above method with an exposure time of 1 ms. An OD 2 neutral density (ND) filter was added to the optical setup to reduce the amount of light reaching the detector, this also increased the range of detection because of the nonlinear nature of blackbody radiation defined by Planck’s law[18]. This resulted in a temperature range of 602-1308 °C at 1 ms. The calibration curves for the 850 nm long pass and OD 2 ND filter can be seen below in Figure 3.14 and the summary of the temperature ranges achieved with the different exposure times in Table 3.3

**Table 3.3 850 nm Long pass filter with OD 2 ND filter calibration ranges**

Exposure Time / ms	Minimum Temperature / °C	Maximum Temperature / °C
1.1	602	1308
10	492	1040
50	471	901

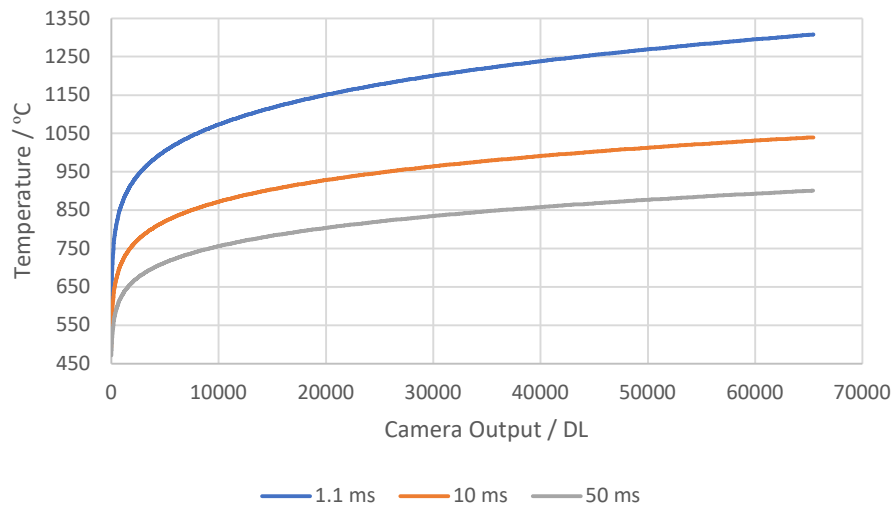


**Figure 3.14 850 nm Long pass filter with OD 2 ND filter calibration curves**

These ranges were more useful for investigating different parts of a build but still did not reach the melting point of the powder. The longer exposure time (50 ms) was suitable for bed preheating and the cooling of sintered powder and also the flow of heat from the part to the sintered powder. However, even with the ND filter the shortest exposure time (1.1 ms) the camera saturates approximately 300 °C below the melting point of the powder.

This was a problem because the melt pool and surrounding area during a build were of much more interest than the bed preheating. To address this a series of narrow band filters were evaluated. Using a narrow band filter will also address the modelling problems with using a long pass filter and therefore an upper wavelength only defined by the FPAs responsivity. The upper wavelength, however, was not well defined because the manufacturer only provided responsivity data up to 1µm, though silicon is sensitive up to approximately 1.1 µm.

Modelling was used to evaluate 4 band pass filters between 850 nm and 1 µm. This was accomplished by using the Planck’s Law to model the blackbody radiation at a given temperature, the transmission model for the filter was the used to simulate the losses in the optical system. The detector quantum efficiency (QE) curve was the used to account for the detector efficiency at each wavelength. The resulting curve was the integrated over the detectors wavelength range and multiplied by the etendue and a gain factor. The model is shown in equations 3.2 and 3.3.

The conversion between power incident on the detector and the counts output by the analogue to digital converters was not known, this is the reason for the gain factor. This parameter was determined experimentally by modelling the 850 nm long pass filter with OD 2 ND filter for which the camera output was already known. The etendue represents the area over which the optical system accepted light from the blackbody source. The values used for gain and etendue were 0.025 and 0.2097 respectively.

3.2

$$S(\lambda) = BB(\lambda) \cdot \varepsilon(\lambda) \cdot Ft(\lambda) \cdot QE(\lambda)$$

3.3

$$Co = g \cdot e \cdot \int_{\lambda_{min}}^{\lambda_{max}} S(\lambda) d\lambda$$

Where:

- $S(\lambda)$  is signal
- $BB(\lambda)$  is the blackbody spectrum according to Planck’s Law
- $\varepsilon(\lambda)$  is the emissivity function
- $Ft(\lambda)$  is the filter transmission function
- $QE(\lambda)$  is the detectors QE function
- $g$  is the gain factor
- $e$  is the etendue
- $\lambda_{min}$  and  $\lambda_{max}$  are the detectors minimum and maximum detectable wavelengths
- $Co$  is the camera output in DLs

The filters chosen to be evaluated using this model were 4 band pass filters with a full width half maximum (FWHM) band of 10 nm. The centre wavelengths of the filters were 870 nm, 900 nm, 960 nm, 990 nm. These were chosen to evaluate the trade-off between increasing energy levels at the longer wavelengths and the decrease in detector QE. Figure 3.15 shows the modelled camera output for each of the filters with the 850 nm long pass as for reference.

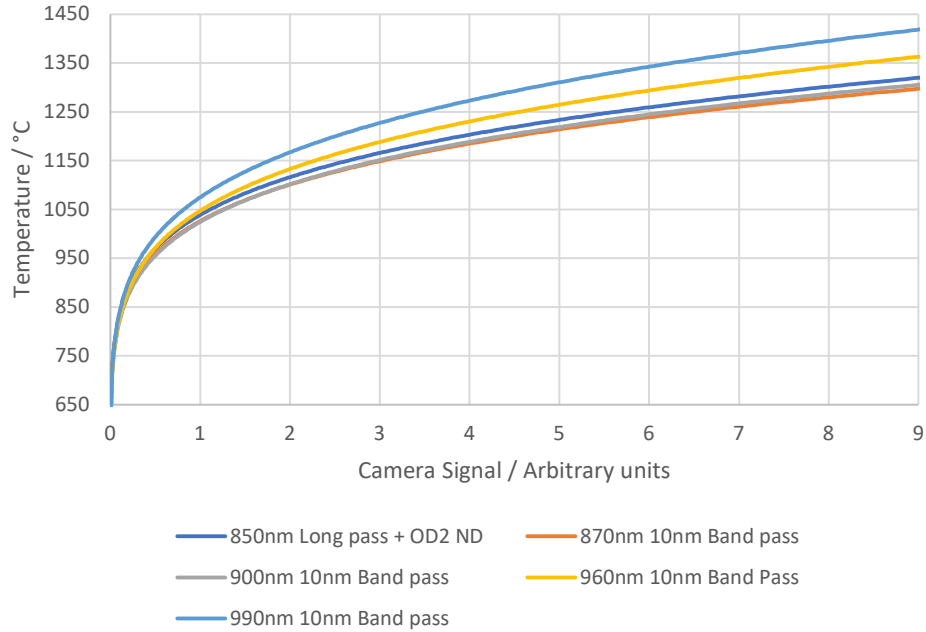


**Figure 3.15 Filter temperature range comparison**

The 960 nm and 990 nm filters were the only filters evaluated to have a larger temperature range than the existing setup, this demonstrates the increase in radiation from a hot source at these wavelengths much outweighs the decrease in detector QE. To verify the results of the modelling calibrations were completed with the 960 nm and 990 nm filters. Table 3.4 shows the temperature ranges achieved with the 2 filters. The 990 nm filter was chosen to be used as the main filter for the system and the calibration results are analysed more in the next section.

**Table 3.4 960 nm and 990 nm Filter calibration ranges**

Filter Centre Wavelength / nm	Exposure Time / ms	Minimum Temperature / °C	Maximum Temperature / °C
960	1.1	577	1368
	10	490	1092
	50	445	927
990	1.1	577	1407
	10	493	1141
	50	446	959

### 3.4.1.3 Calibration Fit Analysis

With the 990 nm 10 nm FWHM selected, the fit to the calibration points using the Sakuma Hattori method was evaluated. This was used to evaluate the quality of the fit and therefore the uncertainty of the temperature measurement due to the fitting of the Sakuma Hattori model to the calibration data. As mentioned above an unconstrained fit

was used which is shown to produce a better fit than a constrained fit where the A and B parameters are calculated based on spectral response[19].

**Table 3.5 Sakuma Hattori fit parameters for 990nm band pass filter with goodness of fit measures**

Exposure Time / ms	Fit Parameters			Goodness of Fit Measures		
	A	B	C	R <sup>2</sup>	SSE	RMSE
50	9.604E-7	1.833E-7	8.27E9	0.9999	32.75	1.908
10	9.525E-7	1.833E-7	1.825E9	0.9999	54.3	2.044
1.1	8.297E-7	7.34E-5	4.68E8	0.9999	88.5	2.609

The fits at the 3 exposure times used in calibration are shown below (Figure 3.16) as well as the fit residuals. Each exposure time was fit separately to ensure the best fit possible, although with only exposure times changing only the C parameter should change between fits. This was because the DLs output by the camera will change linearly with exposure time. Table 3.5 shows the fit parameter values, A and B remain relatively constant across the 50 ms and 10 ms fits but change with at 1.1 ms. This was likely due to the very low value of the first calibration point, the mean DL of the measurement at 457 °C is 0.25. Being at the very low end of the cameras range this measurement will be heavily affected by noise from the sensor.

The fits all have a high R<sup>2</sup> values showing the fit represents the calibration data well, more importantly the also have low root mean squared error (RMSE) values and low sum of squares error (SSE) values in comparison to the datapoints. This value does increase as exposure time gets lower; this was likely because of the same reason as the parameters changing for the 1.1 ms exposure time. With the lower exposure time more of the calibration points are closer to the noise floor of the camera and are therefore more heavily affected by noise. However, when the system was used at shorter exposure times there will be less focus on the lower temperature values because of the lower resolution offered lower in the range. For example, between the first 2 calibration points for the 1.1 ms exposure time there is less than 1DL representing 50 °C.

These were the fits and conversion curves used throughout the rest of the work. Other exposure time values were sometimes required when investigating parts of a build that did not fill the full range of one of these exposure times. To create conversion curves for other exposure times the linearity of the DL change with exposure time was used. The DL values for each temperature were interpolated for the required exposure time, then a new fit created for that data.

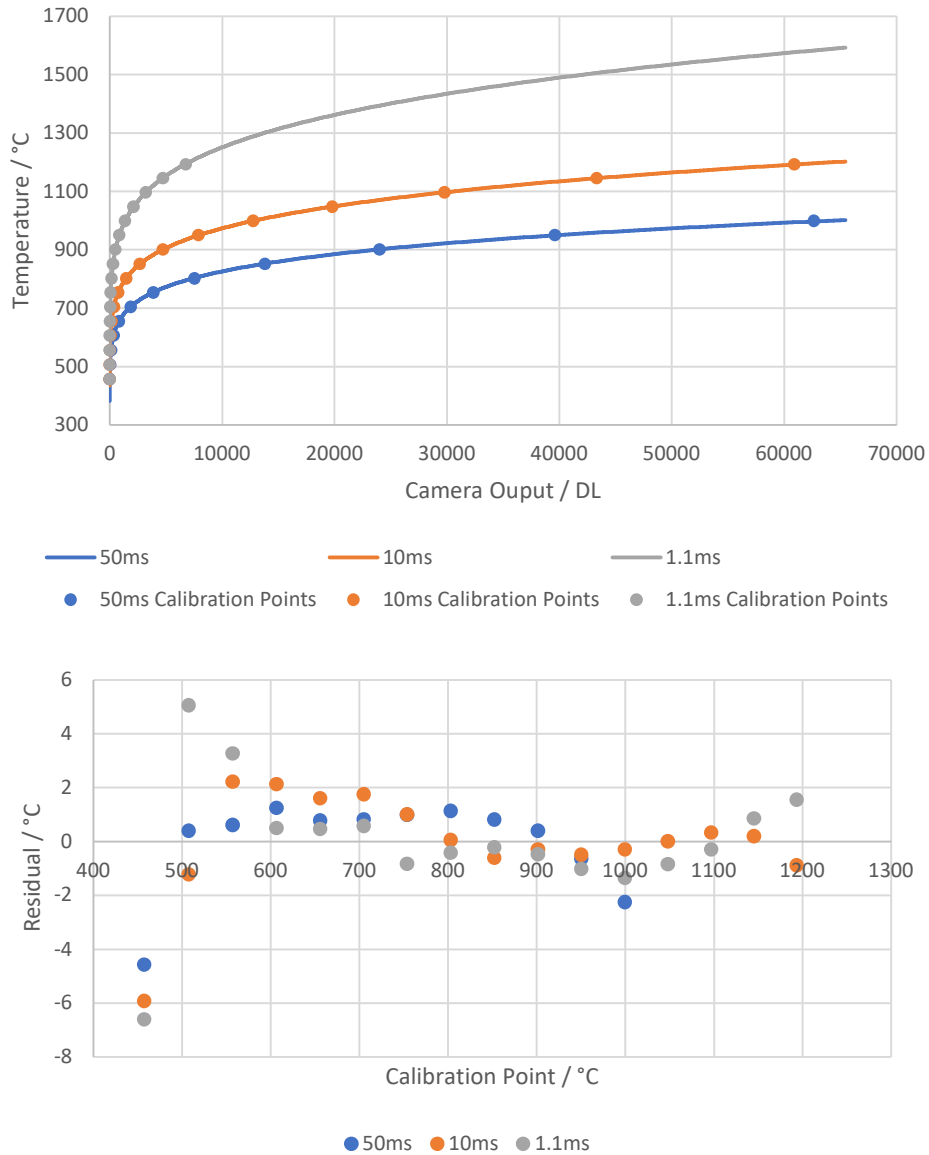


Figure 3.16 Calibration curves and fit residuals for 3 the main exposure times used

### 3.5 Initial Investigations

To prove the imaging system functioned as expected builds were imaged to test the calibrations, recording setup and initial image processing steps. More details on the other parts of the setup and image capture process are detailed in later chapters; here the outputs from those build will be presented.

#### 3.5.1 Overhang Test Build

To demonstrate the capability of the imaging system and illustrate some of the potential problems with EBM that could be detected by using an IR process monitoring system a build with 4 cross shapes was designed. The cross shapes in the build were designed to demonstrate the ability of EBM to successfully melt overhanging faces when the build

parameters are properly tuned. The general shape of the 4 pieces being built can be seen in Figure 3.17. Each part differed by the level of support structures included under the horizontal overhanging face.

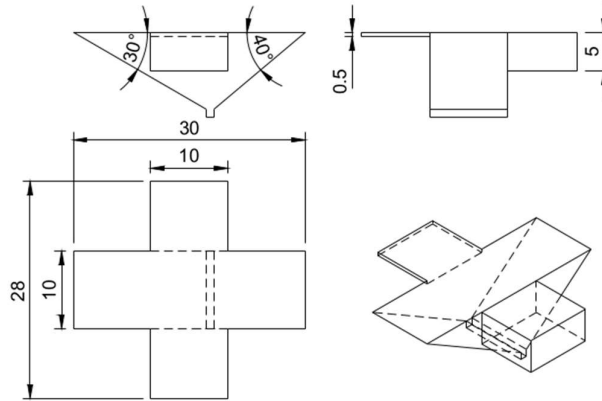


**Figure 3.17 Cross overhang test part drawing (dimensions in mm)**

Using these shapes, the build demonstrated the need for thermal management in the EBM process. The support structures automatically placed beneath the horizontal faces by the build pre-processor do little to actually support the material being melted above them. Their main purpose is to draw heat away from the layer currently being melted. When melting overhanging features on parts some or all of the feature will not be directly above previously melted powder. This is a problem because the thermal conductivity from molten material to sintered powder is much less than to previously melted material [20]. Because the algorithm controlling the beam power does not take this into account it often leads to too much energy being input into an overhanging area. The potential effects of excess energy input were discussed in section 2.3.

This build was part of a series of build where the parameters controlling the beam speed and power were being optimised to allow parts to be built without support structures and with minimal overheating. This made it a perfect candidate for thermal imaging, because the thermal effects of overheating on the overhangs with unoptimized parameters should be visible on the images.

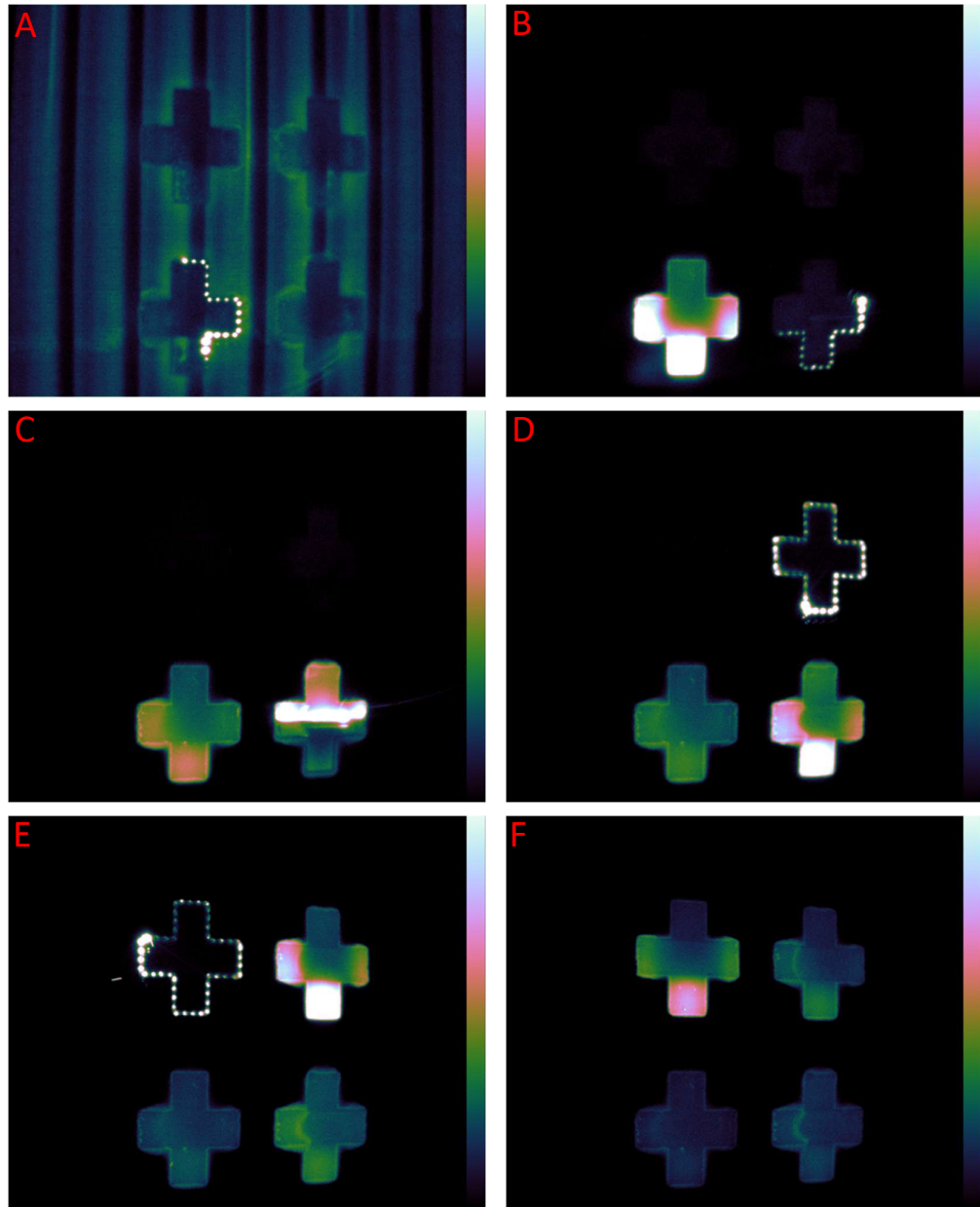


**Figure 3.18** Sample images from overhang test build. Images A-F in order show the progression of the layer, building 4 of the test pieces.

Figure 3.18 shows sample frames from this build, it shows 4 parts orientated with the completely horizontal overhanging face towards the bottom of the frame. Images A-F show a progression through the layer from the contour of the first part to the completion of the last. In Figure 3.18.A 4 parts can be clearly seen in the images even though the current layer has not yet been melted. This shows the temperature difference between the part and the sintered surrounding and the affect the previous layers have on powder laid down on top of them. All the images presented of this build are taken from the first layer of the horizontal overhang, this should demonstrate the worst-case scenario for heat transfer back through the rest of the part. The top left part in this build has support

structures for comparison with the other 3 parts that do not, these 3 have different changes made to the melt strategy to try and produce the best build without supports.

In Figure 3.18 across all 6 images the residual heat in the parts after melting can be seen, especially on the 30° and 40° overhanging faces. This is exactly the kind of issues that it was hoped could be identified with in situ thermal imaging.

### **3.6 Conclusion**

This chapter has shown the selection, calibration and first experiments with a silicon sCMOS thermal imaging camera for use in additive manufacturing. Silicon detectors are an uncommon choice for thermal imaging due to their limited detection range in the NIR and therefore are only able to resolve high temperature objects. This is not an issue in AM and makes the sCMOS camera a very good fit due to its high speed and resolution. Although this was the first experiment with the system it shows that it is capable of producing higher resolution thermal images of an AM process than previously published systems. It showed the system working in situ and able to detect features of the build in progress and potential defect areas. This makes it a good platform to work on for further work on AM process monitoring. It is also something that has not been shown before, the use of high resolution sCMOS NIR imaging in AM. The advantages this system brings have the potential to be used to give more insights into EBM and shed light on parts of the process that were previously very hard to capture.

- [1] MatWeb, "ASM Material Data Sheet Ti-6AL-4V." [Online]. Available: <http://asm.matweb.com/search/SpecificMaterial.asp?bassnum=MTP641>. [Accessed: 26-Jul-2019].
- [2] Arcam AB, "Arcam EBM S12 System Information," 2016. [Online]. Available: [www.arcam.com](http://www.arcam.com). [Accessed: 27-Jul-2019].
- [3] A. Rogalski, "History of infrared detectors," *Opto-Electronics Rev.*, vol. 20, no. 3, 2012.
- [4] The Imaging Source, "DFG/USB2pro - Video-to-USB 2.0 converter." [Online]. Available: <https://www.theimagingsource.com/products/converters-grabbers/video-to-usb-2.0-converters/dfgusb2pro/>. [Accessed: 27-Jul-2019].
- [5] Hamamatsu Photonics K. K., "Hamamatsu C11440-36U Information Sheet," 2016.
- [6] Hamamatsu Photonics K. K., "ORCA Flash 4.0 V2 C11440-22CU Information Sheet," 2015.
- [7] FLIR Systems Inc, "FLIR A6250sc SWIR InGaAs Infrared Camera Datasheet," 2015.
- [8] P. K. K. Hamamatsu, "Hamamatsu C13440-20CU Information Sheet," 2016.
- [9] R. B. Dinwiddie, M. M. Kirka, P. D. Lloyd, R. R. Dehoff, L. E. Lowe, and G. S. Marlow, "Calibrating IR cameras for in-situ temperature measurement during the electron beam melt processing of Inconel 718 and Ti-Al6-V4," p. 986107, 2016.
- [10] J. Schwerdtfeger, R. F. Singer, and C. Körner, "In situ flaw detection by IR-imaging during electron beam melting," *Rapid Prototyp. J.*, vol. 18, no. 4, pp. 259–263, 2012.
- [11] J. Dixon, "Radiation thermometry," *J. Phys. E.*, vol. 21, no. 5, pp. 425–436, 1988.
- [12] Isotech, "Isotech milliK Percision Thermometer Datasheet." [Online]. Available: <https://www.isotech.co.uk/assets/uploads/Data Sheets/milliK.pdf>. [Accessed: 17-Aug-2019].
- [13] Isotech, "Reference Probes - Semi Standards Termocouples." [Online]. Available: <https://www.isotech.co.uk/assets/uploads/Data Sheets/Isotech Semi Standard TC.pdf>. [Accessed: 17-Aug-2019].
- [14] Land Instruments, "LANDCAL Blackbody Temperature Calibration Sources | AMETEK Land." [Online]. Available: <https://www.ametek-land.com/products/calibration-sources/landcal-infrared-blackbody-calibration-source>. [Accessed: 17-Aug-2019].
- [15] F. Wang and A. Theuwissen, "Linearity analysis of a CMOS image sensor," in *IS and T International Symposium on Electronic Imaging Science and Technology*, 2017, pp. 84–90.
- [16] E. R. Fossum, "CMOS active pixel image sensors," *Nucl. Instruments Methods Phys. Res.*, vol. 395, pp. 291–297, 1997.
- [17] F. Sakuma and S. Hattori, "Establishing a practical temperature standard by using a narrow-band radiation thermometer with a silicon detector," *Temp. Meas. Control Sci. Ind.*, vol. 5, pp. 421–7, 1982.
- [18] P. Saunders, *Radiation Thermometry: Fundamentals and Applications in the Petrochemical Industry*. SPIE Press, 2007.
- [19] B. Lane, E. Whinton, V. Madhavan, and A. Donmez, "Uncertainty of temperature

measurements by infrared thermography for metal cutting applications,”  
*Metrologia*, vol. 50, no. 6, pp. 637–653, Dec. 2013.

- [20] C. J. Smith, S. Tamas-Williams, E. Hernandez-Nava, and I. Todd, “Tailoring the thermal conductivity of the powder bed in Electron Beam Melting (EBM) Additive Manufacturing,” *Sci. Rep.*, vol. 7, no. 1, 2017.

## **4 Process monitoring of Electron Beam Melting with Thermal Imaging**

### **4.1 Introduction**

In this chapter the capabilities of the thermal imaging system detailed in the previous chapter are explored. Processing techniques for the images are shown and are developed into applications of the system. These include material property investigation, emissivity tracking and build stage identification; amongst others. These processes are demonstrated and their use in an AM/EBM workflow discussed.

### **4.2 In Situ Part Property Investigation**

One of the driving forces behind the current trend towards AM in industry is the ability to manufacture freeform geometry not possible with traditional manufacturing methods. With the ability of the machines, like the Arcam EBM, to build parts to near net shape it should also reduce the time and cost involved in the manufacture of these freeform parts. However, moving to a new process means leaving behind many years of experience in traditional manufacturing methods for industry. Trust and experience in AM techniques needs to be built up so large industry can have the quality assurance in their parts that they currently do with traditional processes [1].

Due to the additive nature of AM processes they offer a much greater potential for in situ process monitoring versus some traditional processes. With AM processes, especially additive layer processes like EBM, a view into the part is available to every stage of the process. With a subtractive process like milling or turning the outside surface and geometry can be monitored, but most of the focus for in process monitoring is around monitoring of the tools used to make the part, and not the part itself [2], [3]. This leaves testing processes to inspect the parts after manufacture to assure quality, often adding another step to the process. Integrating the part inspection into the AM process starts to solve the two problems of trust and quality control [4].

An experiment to investigate the mechanical and metallurgic properties of Ti-6Al-4V parts produced with EBM was designed. This experiment was interested in the variation of properties seen within one large volume part. It was theorised that over a large volume the properties would differ due to the heating and cooling characteristics of the EBM process. A large solid block (120 x 120 x 60 mm) was built to facilitate this investigation. This may not be a common part for an AM process, but it was designed to produce a large area to investigate the heating and cooling patterns in different locations within the build chamber and on the part. This was investigated with post build analysis on mechanical test coupons created from the block. These were cut as per Figure 4.1 below using electron discharge machining (EDM) and allowed tensile testing in both orientations and different locations in X, Y and Z after being machined according to ASTM E8 [5].

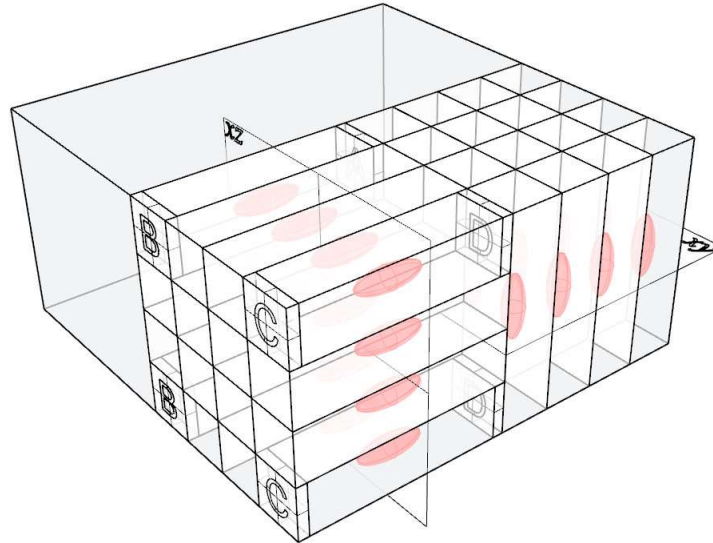


**Figure 4.1 Positions of test coupons cut from the solid block**

Cooling rates were the main focus of this investigation so an exposure time of 50 ms was used to balance temporal resolution against temperature range. It was important to be able to capture as much of the cooling profile as possible, down to the steady state temperature that the material reached between layers. The 50 ms exposure time allowed this with a calibrated temperature range of 400-1000 °C.

During the build the thermal imaging setup was used to monitor layers every 0.49 mm (7 layers) for the first 10 mm. This allowed a view into the thermal properties of the first row of cuboids in multiple locations. From this data the bottom 4 cuboids were inspected (between the B and C markers in Figure 4.1), and this data used to investigate trends for the rest of the block. To allow this investigation 9 locations across the block were evaluated in detail, 3 along each edge and one in the centre (forming a 3x3 grid of points across the part). From close inspection of these locations patterns in the cooling rate across the build plate should be identifiable. There was the expectation that any effects seen would be symmetrical between the left and right sides of the build plate. This is due to the nature of the heat shields in the Arcam being symmetrical left to right but not front to back. The heat shields play a crucial part in the energy input when melting. When they become dulled, due to heat cycling and condensation of vaporised metals from the process, builds will quickly begin to fail because they absorb too much heat rather than reflecting it back down to the powder bed.

Using the 9 locations described above, the mean of a small 10x10 pixel area at each location was used to calculate an average temperature for each area, reducing the effect of pixel to pixel noise on the measurement. Temperature and cooling rate plots were created from these data points and used as the main analysis tools in this process. When

plotting all 9 areas on a single axis the individual stages of the layer can easily be identified. Figure 4.2 shows this and also highlights one of the flaws in the current design of the system.

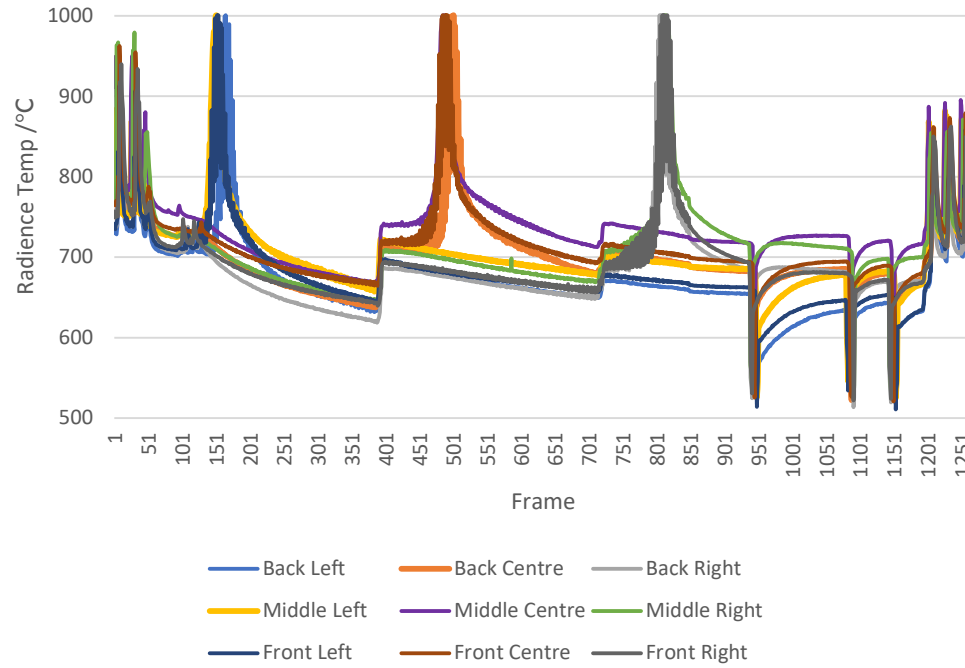


**Figure 4.2 Radiance temperature plot from a single layer at 10.01 mm. All stages of the build can be seen; preheat - rapid changes at the start and end, melt - large peaks at each of the locations in order (it is evident this layer melted from left to right), new powder deposition - rapid decreases toward the end when the rake passes through the areas of interest. The advancing of the film can be seen between frames 350-400 and 700-750.**

The large changes in apparent temperature around the film being advanced shows the flaw. The large change in temperature was due to the metallisation build up on the film in front of the window. The advancing of the film is a manual process and is not continuous, therefore during the melt the transmission of the window changes and because of the very large melt area of the layers in this build noticeable changes can be seen in the temperature plots in a single layer. The step changes in the curves are the film being advanced and full transmission being restored. The film was advanced just before the start of melting of each point of interest to ensure reliable temperature data from these areas.

Cooling rates were the focus of this investigation, this is because the cooling rate of a material can define a lot about its properties. The rate at which a material cools through certain temperatures will define grain size and type which will go on to affect the materials mechanical properties. The mechanical properties of Ti-6AL-4V parts are already well known and have been evaluated with different production methods [6], [7]. They show that especially with the temperatures seen in the EBM process, higher cooling rates mean

higher tensile strength. When the coupons cut from the block were tested, this is what was seen, especially with coupons created from the cuboids parallel to the build plate.

When the cooling rate across layers were examined for each area of interest the trends show groupings of locations (Figure 4.3). The cooling rates of the 4 corners were similar, both front and back, and left and right sides are similar, and the centre lies on its own. This matches with the expectations going into the experiment and with the results of the tensile tests and showed more symmetry than expected. This means the heat shields have less of an effect on the cooling rate than previously thought.

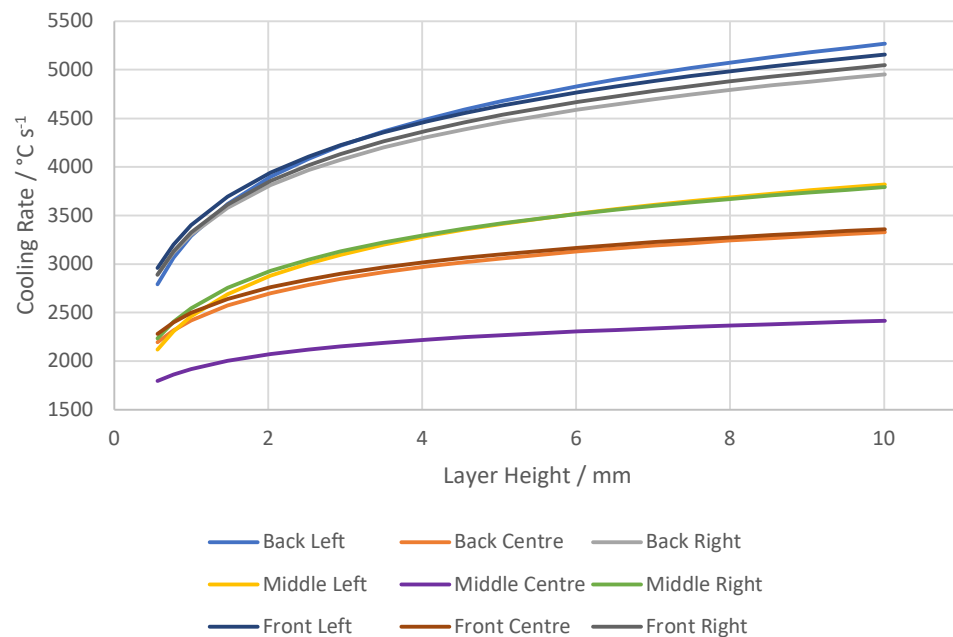


**Figure 4.3 Cooling rate trends across all layers imaged.**

The cooling rate across all areas of interest increases with layer height, this shows the effect the build plate had on the lower layers. The lower cooling rate here was likely due to the energy input into the build plate by the preheating and these layers having the lowest amount of cool powder around them to dissipate the heat into.

With the cooling rates seen by the imager correlating to the tensile strength of the coupons in both the X/Y plane and the Z axis, this was progress toward being able to predict the mechanical properties of parts based on thermal imaging alone. Work like this will start to remove the barriers seen by manufacturers when looking to move to AM parts.

### 4.3 Emissivity Tracking

The nature of the EBM process and its goal of creating solid free form geometry from metal alloy powders provides a challenging environment for a thermal imager. The state changes of the powder within just a single layer of a build leads to multiple surface

changes and different surfaces within a single image, this leads to differing emissivity across a single image and for a given area across a series of images.

When the powder is freshly dispensed and raked from the hopper it will be considerably cooler and is likely to have a different packing than the layer below; due to the melting and sintering that has occurred previously on that layer. The preheat phase of the new layer will then lightly sinter the new powder, inputting heat and changing the surface topology. The melting phase will then melt areas of powder, once again changing the surface of the layer visible to the imager. This is shown in Figure 4.4 below.

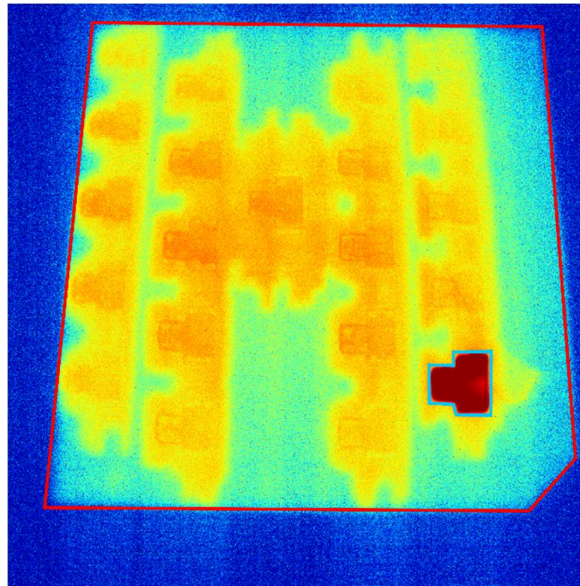


**Figure 4.4 Image annotated with areas of different emissivity. Outside of the area marked red is unsintered as deposited powder, inside the red area the powder has been lightly sintered by preheat, inside the blue area the powder has been melted. Heat transfer from the previous layer is also apparent in this image, because only one part has been melted but multiple part outlines can be seen.**

The changes in the surface visible to the imager provide an almost constantly changing emissivity to account for when making temperature measurements. Emissivity is an area that is often overlooked in thermal imaging and is especially relevant in an application like this where it can fluctuate greatly. Using the method shown by Sih & Barlow [8] the emissivity of the unsintered powder bed can be estimated as follows.

The total emissivity of the powder bed is a function of the emissivity of the solid powder particles  $\epsilon_S$ , and of the holes in the surface of the bed created by the random packing of the powder  $\epsilon_H$ . This is because the geometry of the holes will create an emissivity enhancement and could make the holes have an emissivity approaching 1.

$$\varepsilon = A_H \varepsilon_H + (1 - A_H) \varepsilon_S \quad 4.1$$

Where:

$A_H$  is the fractional area of the surface covered by holes  
 $\varepsilon$  is the total emissivity of the bed as a whole.

$$A_H = \frac{0.908\varphi^2}{1.908\varphi^2 - 2\varphi + 1} \quad 4.2$$

$$\varepsilon_H = \frac{\varepsilon_S \left[ 2 + 3.082 \left( \frac{1-\varphi}{\varphi} \right)^2 \right]}{\varepsilon_S \left[ 1 + 3.082 \left( \frac{1-\varphi}{\varphi} \right)^2 \right] + 1} \quad 4.3$$

Where:

$\varphi$  is the fractional porosity of the powder bed.

From the datasheet for the titanium alloy from Arcam [9] used in the builds (Ti-6Al-4V) the particle size is quoted as 45-100  $\mu\text{m}$ . Using this as a guide for particle size a fractional porosity value of 0.075 for 76  $\mu\text{m}$  particles was used from Heim et al. [10]. A value of 0.35 for  $\varepsilon_S$  was used based on work by González-Fernández et al. [11]. Calculating the area of holes,  $A_H$ , and the hole emissivity  $\varepsilon_H$  using equations 4.2 and 4.3 produces the following values:

$$A_H = 0.00593$$

$$\varepsilon_H = 0.996$$

Therefore, the estimated emissivity of the surface using equation 4.1 is:

$$\varepsilon = 0.354$$

The effect of the holes on the emissivity of the powder bed surface is small, this is due to the high packing efficiency of the small powder particles, as demonstrated by Heim, leaving the area of the bed containing the holes at only 7.5%. If this is reevaluated with the larger particle size of 98  $\mu\text{m}$ , towards the higher end of particle sizes in the powder, and therefore a larger  $\varphi$  of 0.159  $\varepsilon$  increases to 0.370.

This may be an apparently small change in emissivity, however, because of the non-linear DL to temperature conversion performed large changes will be seen especially at higher DL values. Shown in Table 4.1 is the evaluation of a temperature conversion, using the Sakuma Hattori method, with the two emissivity values above and no emissivity correction. The minimum and maximum detectable temperatures are shown. At low DL values the radiance temperature is  $\sim 50$   $^{\circ}\text{C}$  below the temperature with emissivity correction applied and this rises to  $\sim 250$   $^{\circ}\text{C}$  at the top end of the detectable range. The difference in emissivity corrected temperatures shows the sensitivity of this correction; with a difference in emissivity of 0.016 resulting in a maximum temperature difference of 12.83  $^{\circ}\text{C}$ .

**Table 4.1 Comparison of emissivity corrections for a 650 us temperature conversion curve**

	Radiance Temperature / °C	Corrected Temperature / °C $\varepsilon = 0.354$	Corrected Temperature / °C $\varepsilon = 0.370$
Minimum	533.54	584.43	582.15
Maximum	1677.84	1946.49	1933.48

The powder bed emissivity is one of the more fixed emissivity's when looking at an in-progress layer of an EBM build. The molten metal will have a much wider range of values because of its almost constantly changing temperature and surface. The heating and cooling rates are high in EBM; the large energy input can cause the powder to melt and solidify in ~20 ms. Giving heating and cooling rates of ~3000 °C/s (calculated from radiance temperatures on a high speed 500 fps imaging run). In the same amount of time the surface visible to the camera also changes greatly. The powder bed, although raked flat, is full of small holes because of the packing of the powder as discussed above. Once the powder is heated through its melting point to a liquid state the surface finish changes again and the surface shape is also affected by the electron beam. This could create geometric features in the melt pool. Then once the material has solidified the surface finish and shape will settle.

To account for the constantly changing surface visible to the imager a dynamic emissivity correction would be required. This is difficult to realise because of the multiple parameters that calculating the emissivity relies on, especially when one of those is temperature which is also the measurement of interest. This means when making corrections some assumptions must be made if no other information is available on the temperature or surface topology of the powder bed. Providing additional information is difficult in this process because a temperature measurement that is not affected by emissivity, for example a contact temperature measurement, is not possible; hence the use of thermal imaging. Also predicting the surface of a given section of the build is difficult because of the different build parameters of each build and how each part of a given build will be affected by the geometry of the whole build. With this in mind a constant emissivity is assumed before melting and after freezing in the rest of this section.

To begin to address the changing emissivity detailed above an emissivity tracking algorithm was developed. This tracked the melt pool across a single layer of a build and applied different emissivity values based on previously detected melted areas. This allowed for dynamic emissivity correction on a frame by frame basis, outputting thermal images with a corrected temperature.

The algorithm was built into the existing MATLAB image processing software, written to convert the raw DL output of the camera into temperature images, along with other image

processing features. Both global and local emissivity correction has been implemented; the global correction is used for applying a single emissivity to the whole image, for example, when only imaging a small area on cooldown, the local correction is described here.

The local correction worked by using thresholding, blob detection and morphological image processing techniques. The purpose of the processing on each frame is to create a mask selecting only the melt pool in each image. Depending on the build and camera exposure settings there can be multiple apparent melt pools in an image even though there is only one being created by the electron beam. This was because of the persistence of vision effect on longer exposure times and the multibeam setting being used on the build theme. The multibeam setting changes how the machine melts the contour of the part; rather than melting one continuous contour it splits the contour into up to 10 segments and melts each one in stages of a set length. A diagram of how this works is shown below in Figure 4.5, the contour is split into 4 segments as shown by the blue lines, the other coloured lines show the equal length stages that each segment is split into and the numbers represent the melt order.

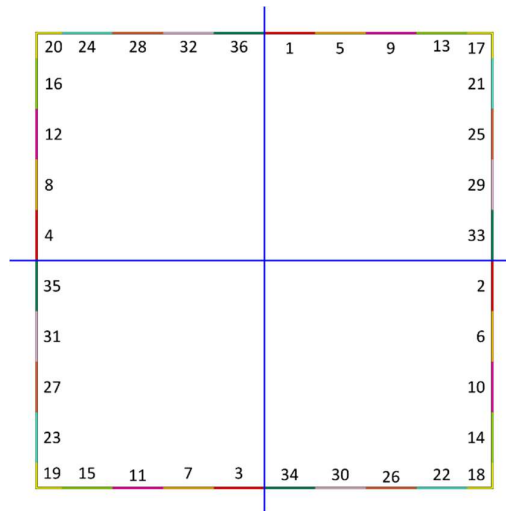


**Figure 4.5 Example of contour melt order with multibeam enabled**

The local correction was designed to handle the multibeam contour setting, with up to 10 melt pools present in the image. Each melt pool could appear at a different point in time within one exposure therefore, the brightness seen in one frame can vary for each melt pool. The detection process accounts for this, with the threshold creating a binary image that contains all the possible locations of the melt pool, then the blob detection and morphological closing select which are of the expected size and shape. The expected melt pool area and diameter can be set individually when processing the files because these will vary depending on the current build theme and camera setup.

Blob detection is an image processing technique used on binary masks to identify connected regions of pixels and then calculate their properties. A connected region is

defined for this algorithm as a group of pixels that are joined by at least 1 pixel in their neighbouring 8 pixels. Each group of pixels that are detected have their centroid, major and minor lengths and angle calculated. This information was used to redraw the melt pool blobs onto a new image as ellipses. This was done to smooth the detected areas, as well as account for the effect of seeing multiple melt pools of different intensity in one image (Figure 4.6.C) as described above. Without the redrawing step there would be holes in the melt pool mask at the end of layer, where from inspection of the final part, it was clear powder had been successfully melted.

The final step of the detection process was to use a morphological closing operation on the mask of redrawn melt pools (Figure 4.6.D). A morphological close of a binary mask is the process of performing a dilation and erosion on that mask using the same structuring element. A structuring element is a small mask of pixels that is used to convolve an image, here a disk-shaped structuring element with a diameter the size of the expected melt pool diameter was used, usually in the region on 10s of pixels. To dilate a binary image the centre of the structuring element is superimposed over every background pixel, a 0 pixel in a binary image, if any pixel under the structuring element is a foreground pixel, a binary 1, the current pixel of interest is set to 1. This has the effect of growing the boundaries of foreground regions by the size of the structuring element. Morphological erosion is the inverse of this operation; the structuring element is superimposed over each foreground pixel and if there are any background pixel under the structuring element the current pixel is set to 0 and the foreground mask is shrunk.

Combining these processes into a closing operation has the effect of closing any holes in the foreground mask and removing foreground regions that are smaller than the structuring element, all whilst keeping the shape of the original mask intact. This means that any detected regions that are smaller than the expected melt pool diameter are removed and small holes in the mask closed. Examples of a mask at each step in this process is shown in Figure 4.6.

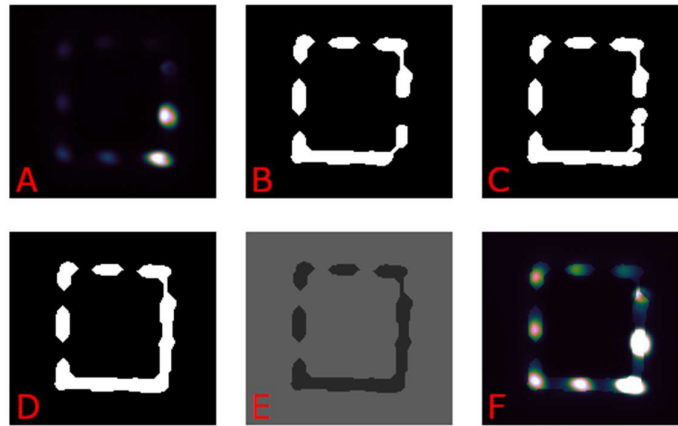


**Figure 4.6** Examples of states within the emissivity correction process. A. Input image B. Input mask (from previous layers) C. Mask after initial melt pool detection and redrawing process D. Mask after morphological operations E. Emissivity image F. Output image

The mask of each frame was then added to all the masks that have been created before it to create a mask of the melted areas so far on that layer. The mask of each frame was also recorded and used to calculate other melt pool properties described later in this chapter. To apply an emissivity correction to the current frame the foreground pixels of the melted mask were set to the melted emissivity and the background pixels to the unmelted emissivity, creating an ‘emissivity image’ (Figure 4.6.E). The raw DL image was then divided by this ‘emissivity image’ to correct for the differing emissivities of the two areas. An example of the mask build up images and emissivity corrected images are shown in Figure 4.7. The MATLAB code that implements the emissivity tracking function is listed in appendix 7.1.

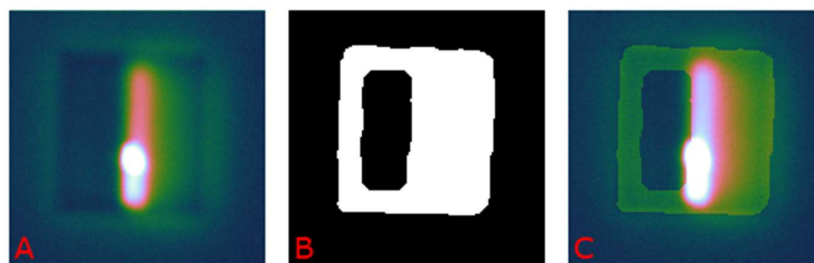


**Figure 4.7** Emissivity correction applied to an image. A. Uncorrected image B. Mask image created by the emissivity correction algorithm C. Image with emissivity correction This is an image from later in the same layer shown in Figure 4.6 where the squares internals are being melted from right to left

As well as providing the emissivity correction which was necessary for accurate temperature measurement this process makes manual visual inspection of the images much easier once a suitable colour map was applied. This was because the emissivity

correction increases the dynamic range of the image, which once converted to a temperature can be as low as 200 digital levels.

#### **4.4 Melt Pool Sizing Analysis for Porosity Measurement**

The melt pool detection techniques developed for emissivity tracking have proven to be useful for more than just emissivity tracking. As an automated way of detecting the melt pool location across the whole build area, position and size information can be extracted from the output of the detection process on each image. This was used in work on determining the porosity of metal 3D printed parts, an important characteristic if AM parts are to be trusted by manufacturers. This work was conducted as a continuation of the work by Thompson et al. [12] into analysing the porosity of EBM parts using post analysis X-ray Computed Tomography (XCT). In this paper the authors find, by analysing individual weld lines, that melt pool width can be an indicator for porosity. This conclusion was drawn from manual analysis of surface weld lines and the authors comment that automated measurement would be desirable in the future.

Melt pool size measurements were extracted from the internal melt pool detection step not previously used in the emissivity tracking. This was possible because of how the emissivity tracking method detects the melt pool in each image. After detection position and width measurements were taken from the individual image mask before it was added to the historical mask image.

The in-situ measurement method of thermal imaging has key advantages over the ex-situ XCT. The primary being the ability to image throughout the build and provide measurements on subsurface layers or surfaces that would be obscured by the final geometry without having to use destructive analysis techniques. This was used in both sets of tests that were carried out, the first using a standard build theme that rotates the melt direction by 90° each layer, where the ability to measure in-situ, layer by layer allowed each melt direction to be measured independently. The individual layers for each direction would be very difficult to locate for ex-situ measurement, likely meaning the build parameters would need to be forced to only melt in one direction per part; making the parts unrepresentative of real builds. In the second test different melt parameters were evaluated across 3 parts in the same build, the in-situ measurement here allowed the measurements to take place at varying heights in the build, approximately every 1 mm, and for the exact layer of each measurement to be known.

The analysis of the parts is still ongoing but initial results showed higher levels of porosity towards the edges and corners of the parts. This matched with smaller sized melt pools detected by the tracking algorithm in these locations.

## 4.5 Visualisation

### 4.5.1 High bit Depth Images

When dealing with high bit depth, high resolution data (in this case 16-bit, 2048x2048) visualisation is a problem. Standard computer monitors are only 8-bits per colour, meaning single colour images, traditionally greyscale, can only display 256 levels on screen. The dynamic range of 16-bit image data is 256 times this, a normal person also struggles to differentiate many different shades of the same colour in a small space. This problem has traditionally been solved with the use of colourmaps, where >8-bit data is mapped into the RGB colour space, where 16M colours are available. There are many different colourmaps that are used for different image data as well as generic ones. One criticism of mapping a greyscale image to colour for viewing is that colourmaps can change the viewers perception of the data and promote misinterpretation. For example, a colourmap running from blue through green and yellow to red, as the default MATLAB colourmap Jet does, can exaggerate small changes in the data at the high end. This is where the colourmap runs from green through yellow to red and because the human eye is much more sensitive to green light changes in this range are easier to detect for the viewer[13].

For this reason, it was important to select a colourmap that did not exaggerate small changes in radiance, which there are a lot of in this data. The Clube Helix colourmap [14] was selected and has been used for a majority of the images processed. This colourmap, originally designed for use with astronomical data, is designed to provide a linear increase in perceived brightness across its range of colours. This solved the main problem described above with other colourmaps. The MATLAB implementation was used [15] with the initialisation parameters in Table 4.2, producing the colourmap shown in Figure 4.8. When used with an appropriate scale this colourmap has been interpreted easily and accurately by most viewers of the thermal images coloured with it.



**Figure 4.8 Cube Helix colourmap**

**Table 4.2 Cube Helix initialisation paramaters**

Number of points	Start Colour	Rotations	Saturation	Gamma
Temperature max – temperature min	0.5	-1.5	1.29	1

### 4.5.2 3D Visualisation

Representing data from a single image is not the only challenge presented by datasets collected from EBM. Individual layer data can be represented as a video showing the

progression of the layer with time, however because EBM is ultimately a 3D process as soon as the machine advances to the next layer all information about previous layers becomes invisible when the data is represented like this. A lot of analysis can be done on a single layer of data especially when layers are compared from multiple heights in the build, however, this work can only be done in the X, Y plane and no 3 dimensional, or Z data, can be considered.

To visualise the datasets fully in 3D a workflow using Qt [16], Open CV [17] and ParaView [18] was developed. This process allowed a build to be visualised in 3D by using the melt pool detection provided by the emissivity tracking process above. Using knowledge of where on a layer (the X, Y plane) has been melted and layer height data can be stacked in the Z direction and selectively displayed to show solid areas as layers progress or data over time for the final solid build volume. This allowed layers to be visualised as they were built or can be used to easily look for patterns over different layers. Each voxel (3D pixel) can also be coloured according to temperature recorded on that layer. Examples of these visualisations can be seen below in Figure 4.9.

The process to create these visualisations starts with processing the raw images output from the camera with a version of the image processing scripts used in the rest of this work but rewritten in C++ and Open CV to take advantage of the speed improvements and parallelism versus MATLAB. This was done because processing large multilayer datasets in MATLAB can be very memory intensive and time consuming. The first step was to run the local emissivity correction algorithm detailed above and create a set of mask images for the layer. These mask images are binary masks showing where the emissivity correction algorithm determined the powder has been melted in an image. The mask images were used by the next step of the process to create a ParaView dataset containing the melted area and temperature data for each image.

The process of creating the ParaView dataset first crops the mask to the extents of the melted area on the final image of the layer, this minimises the output size whilst ensuring no data loss because the last image from the layer will contain all the melted points on that layer. It then recorded the voxel coordinates of each voxel inside the cropped area as well scalar information containing the temperature of each voxel into a VTK data file used by ParaView. This step can be run on multiple layers from the same build and will automatically stack layers inside the VTK data files based on layer heights. This conversion step was the main reason for recreating the process outside of MATLAB because the processing of each image does not rely on the last it can be easily parallelised. In this case the map feature of the Qt Concurrent library in the Qt framework was used to distribute the work between all processing cores of the computer and provide a speedup approximately equal to the number of cores.

The data was then imported into ParaView and a processing pipeline used to select the data to be visualised and how to display it, e.g. colour maps, 2D/3D. This can be in a time-based mode which will show the progression of the layers as they were built, with or without temperature colouring. Another way is to visualise the whole melted volume as it was at the end of the build and have temperature information represented on this 3D model as colour, here layers can either be played back as they were created (layer by layer) or simultaneously, synchronising the start times of each layer. This visualisation method proved useful for finding areas of interest that occurred through multiple layers, for example, swelling or multilayer unmelted powder defects.

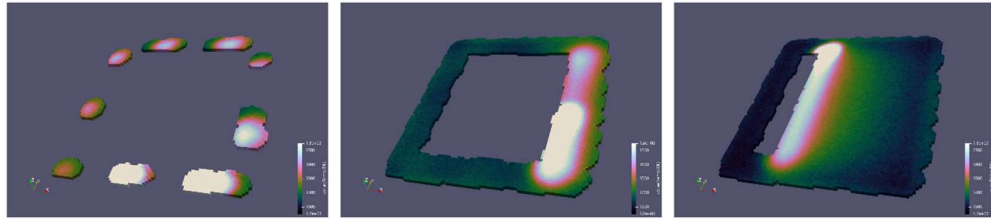


Figure 4.9 Example frames from a 3D visualisation video

## 4.6 Build Stage Identification

One of the challenges identified early with this setup was the amount of data that was generated because of the high speed, high resolution nature of the thermal imaging setup. When running with a camera link connection the camera can generate up to 800Mb/s; well over the write speed of leading SSDs, rated at 550Mb/s [19]. This meant saving all frames to disk as they are captured was not possible. Therefore, for work that has required the camera to be in high data rate mode (most of the work presented here) incoming image data had to be buffered to RAM before being saved. This in turn limits the number of images that can be captured because of the comparatively limited capacity of RAM. For example, the capture PC used was equipped with 32Gb RAM, 500Gb SSD and a 1Tb HDD. A 3 step system was used when capturing large amounts of data; images would be buffered into RAM then written to the SSD to take advantage of the high write speeds and allow the next capture to start as soon as possible. Full datasets would then be moved to the HDD for longer term storage before backup.

### 4.6.1 Custom Acquisition Software

The limitations of the setup meant that it was often impossible to capture successive layers and even limited the capture time of a single layer depending on the required settings. To begin to address this problem some custom capture software was created to be used instead of HClmage Live, provided by Hamamatsu with the camera. This software written in C++ with the Qt framework and Hamamatsu SDK implemented all the basic features required to capture images and adjust relevant camera settings such as exposure time and frame size. It also added features like a real time temperature conversion and a

frame rate limiter for when longer data acquisitions were more advantageous versus high speed capture. Being written solely for the research task also allowed it to be extendable and accommodate other inputs or processes where required.

The main reason for its creation however, was to change how incoming frames were recorded to disk, HImage Live created a buffer at the start of a capture and waited until it was full to write it to disk and end the acquisition. This meant that even if the data rate was only just over the disk write speed only the number of frames that would fit into available RAM could be acquired. The custom software changes this to split available memory up into a pool of smaller buffers at the start of an acquisition. During the capture data was written to one of the smaller buffers and asynchronously written to disk when that buffer was full, at which point the next buffer is activated and the process repeats. If a buffer is completely written to disk before the acquisition ended the buffer is returned to the pool of available buffers, allowing it to be used again. This meant that if the disk write speed was high enough to write portions of the dataset to disk during the capture a larger dataset can be captured overall. The number of buffers can be tuned for the incoming data rate and disk write speed to maximise overall acquisition size.

The custom acquisition software worked well in extending the size of dataset that could be captured in one acquisition, however, depending on the build being imaged and the required camera parameters it still wasn't always sufficient. Builds with complex single layers can often take >60 s to complete which is the approximate time offered by an acquisition to RAM with full camera resolution. This was where being able to extend the software to incorporate other processes or sensors became useful. Up until now all acquisitions had been manually triggered, using the live preview of the build chamber to look for the end of the preheat step and trigger the capture. When the acquisition window was only just big enough to fit the full layer, this was problematic. Automated trigger mechanisms that plugged into the acquisition software were explored to solve this. The ideal way for this to happen was signal from the EBM control software running on the machine, but no suitable signal could be found.

#### **4.6.2 Integrating Arcam Sensors**

Integrating into the Arcam hardware to detect layer start and end was explored first. Multiple sensors that could provide this information were examined for suitability and the powder sensors were selected. The powder sensors sit on either side of the build plate and detect when powder has been raked from the hopper across the build plate. The actual sensor sits in a tube below the build area and detects fresh powder falling through it (Figure 4.10).

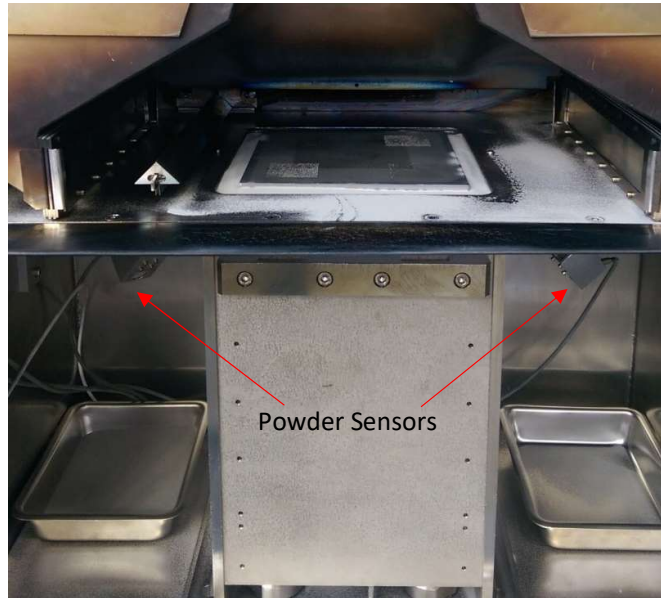


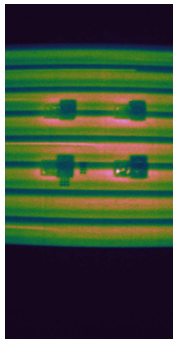
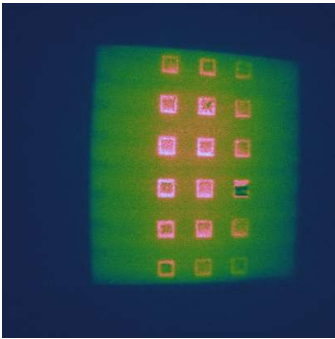
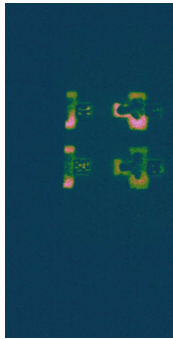
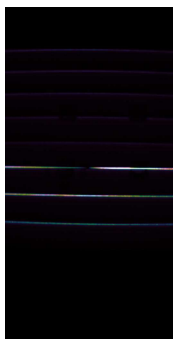
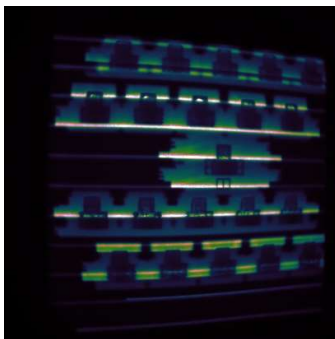
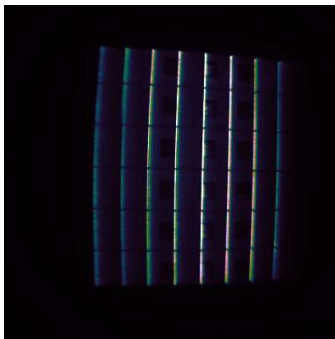
**Figure 4.10 Powder sensors on the Arcam S12 used as inputs for layer tracking, mounted on the left and right of the build tank**

The process of detecting a layer start was to connect into the outputs of the two powder sensors in the electrical cabinet on the Arcam; each sensor would pulse an input of the control system when it was activated. A microcontroller was connected to these outputs that would detect the pulses and report them to the acquisition PC. A piece of LabView code was written to take serial input from the microcontroller and pattern match it to the known sequence of powder sensor activations that would signal a new layer had just been raked and was about to start being melted. The acquisition software would be waiting for a signal from the LabView code to start the capture. A delay could be introduced between the signal from LabView and the start of the capture to avoid imaging the preheat step if it was not of interest.

This method worked well in simulated builds however, not as well once it was applied on the real machine. The hardware and software worked as expected triggering an acquisition when a powder sensor pattern was found (left, right, left for example; the bed is often raked 3 times). However, when used in situ the signal would often be sent at the wrong time, meaning the full layer was not captured. This was because during a build the powder sensors would misfire or not fire at all even when powder had been raked. The machines control system was able to detect this because of the other sensors at its disposal and would re-rake the bed or continue but this could not be detected from the powder sensors alone. Another issue with this method was that because the trigger was only seen just before the layer started, acquisitions would overrun and image the time between layers until the acquisition memory was full or another trigger was seen. This meant unnecessary data was captured and layers missed because the data could not be recorded quick enough to instantly restart an acquisition.

### 4.6.3 Machine Learning Image Recognition

To address the problems with the powder sensor triggering a new approach was taken and the camera input itself used to look for when to start recording data. The EBM process in the Arcam has well defined stages to a layer during a build; powder distribution, preheat, contouring and infill, with some dead time in between each. When reviewing images of a full layer each step can be easily identified by an experienced operator and is how datasets have been pruned throughout this work. The powder distribution step is seen on a thermal image as the cold rake passing over the hot build area from the last layer. In all but the highest framerate captures the preheat step appears as a series of lines moving across the entire build area. The contouring step appears as multiple melt pools moving in lines to melt the outside walls of a part. And the infill or melt step is one melt pool moving back and forth across the cross section of the part in one direction. Because of the distinct appearance of each step it was likely a machine could be trained to recognise each one and the transitions between them. Examples of each step are shown below in Figure 4.11, these show that each stage is visually distinct but not so much so that they are easily differentiated with standard image processing.

Build Stage Classification Example Images			
Wait/Powder Distribution State			
Preheat State			

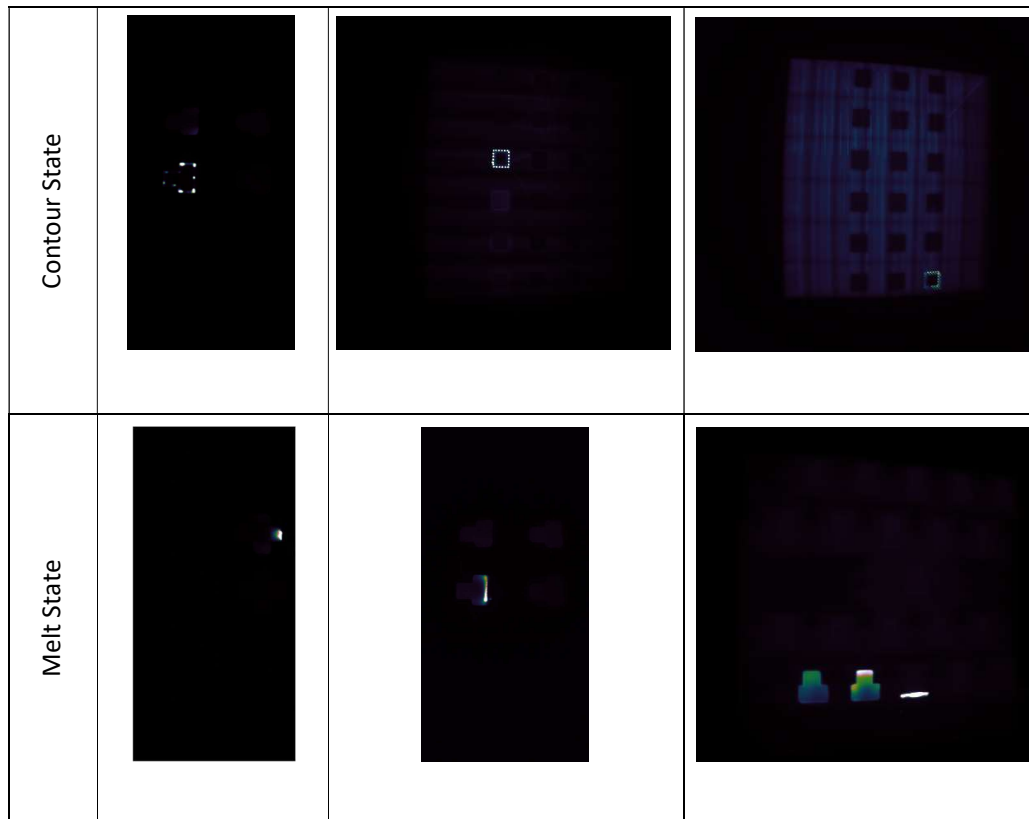


**Figure 4.11 Example images from each class used to training the machine learning algorithm. All images are raw radiance (DL) images, shown with the colour maps set to the full 16-bit range.**

Machine learning (ML) for image recognition is now quite an established field with current state of the art moving onto image segmentation and individual pixel classification versus full image classification. This means that there are multiple methods for image classification, however, it does not appear to have been applied for this purpose before and is only recently starting to be investigated for use in AM [20]. Machine learning image classification is the process of using ML techniques to categorise images based on what appears in them. This is often a supervised machine learning process, where data is manually labelled with the correct classification and is fed into the ML algorithm which creates the function to transform the input to the output; in this case the image to the category.

Machine learning was applied to the problem in two stages, the algorithm was first trained on the data and after a suitable model has been devised it can be exported for use as a standalone classifier. These two steps are often separate, meaning once a model is trained it does not get changed. However, if more data is collected a model can be retrained using the previous model as a starting point. Models can also be run in a more online way with their classifications constantly being fed back to improve them, this is referred to as reinforcement learning [21]. Here the trained model is used on its own, but there is possibility for future retraining with more data. Models are often run this way because the

training portion of the ML process is much more compute and time intensive than classification. Meaning models can be run quicker and potentially on lesser hardware once they are trained. This is because the training process is constantly changing the algorithm parameters to optimise the output and is a multi-pass process; whereas once these parameters are defined only a single pass through the algorithm is needed for classification.

The first step to training the algorithm was to prepare a dataset for it to train on. A large set of images (between 500 and 1000) for each category were collated into a labelled folder structure. It was important the images came from different builds with different camera and build parameters, to ensure the algorithm did not focus on specific features that will only appear in one set of images. This is termed overfitting and means that a ML algorithm will perform well on a training dataset but much worse on real, unseen, data where more generic features are consistently seen. The image classifiers used here do not directly work on image data, instead they rely on feature descriptors to identify features of an image. A SURF feature detector [22] was run over each of the image categories in the training dataset. This searches for features in the images and records their descriptions in a way that is not affected by scale or rotation, allowing them to be easily matched to other features in the future. The strongest features from each category are then used to create a 'vocabulary' to describe each image category. This is done by k-means clustering to group features by the image category they represent, in this case the strongest 250 features from each cluster were selected to create the vocabulary of each image category.

With the vocabulary created MATLABs classification learner was used to evaluate different classification methods in search of accuracy and speed, because the final algorithm will be used on real time data and the quicker the classification the more likely it is to capture all the useful parts of a layer. All available classifiers were evaluated initially, but a Support Vector Machine (SVM) quickly showed to be the most suitable classifier with > 80% accuracy on the training dataset. With further training and modification to the SVMs parameters; i.e. the features it favoured and how those features were represented to the model, an accuracy of > 95% was achieved on the training dataset. The accuracy of each category can be seen in the confusion matrix in Figure 4.12.

After training the model was compressed and exported to be used as a standalone classifier. The process of classifying an image with this model works in two stages. First the image direct from the camera was encoded into a set of features, these features are then matched using the SVM to the features in the image categories. Using this process, the image was labelled with one of the categories and a confidence score for each category was output. The label assigned to the image was the one the algorithm has the highest confidence in. The scores for the other categories can be used to see how the algorithm

was misinterpreting the images and can start to indicate features that are common to multiple categories and should be removed to increase accuracy.

Output Class	Contour	89 21.1%	2 0.5%	0 0.0%	3 0.7%	94.7% 5.3%
	Melt	1 0.2%	159 37.7%	5 1.2%	0 0.0%	96.4% 3.6%
	Preheat	0 0.0%	0 0.0%	105 24.9%	5 1.2%	95.5% 4.5%
	Wait	1 0.2%	1 0.2%	0 0.0%	51 12.1%	96.2% 3.8%
		97.8% 2.2%	98.1% 1.9%	95.5% 4.5%	86.4% 13.6%	95.7% 4.3%
	Contour	Melt	Preheat	Wait		
	Target Class					

**Figure 4.12 Confusion matrix of the trained SVM. This represents the prediction accuracy of each category by comparing the number of correct predictions to the categories of the incorrect predictions.**

To test the algorithm for speed and accuracy, it was evaluated against pre-recorded image sequences containing full layers of an EBM build. The images were fed to into classification algorithm and the classification time and label for each image recorded. Through observation of the outputs of these tests a pattern for detecting the start and end of a layer was developed. The start of the contour phase and the end of the melt phase of the build is where the images from a real build would need to be captured. The algorithm would often detect a 'wait' state in between the preheat and contour phases of the build, so this was built into the pattern for detecting layer start. For layer end the algorithm would correctly identify a large number of wait states after the melt phase had finished, a series of 10 of these was chosen as the pattern to signal layer end. This was because during slight pauses between melting steps in the build the algorithm would also detect wait states.

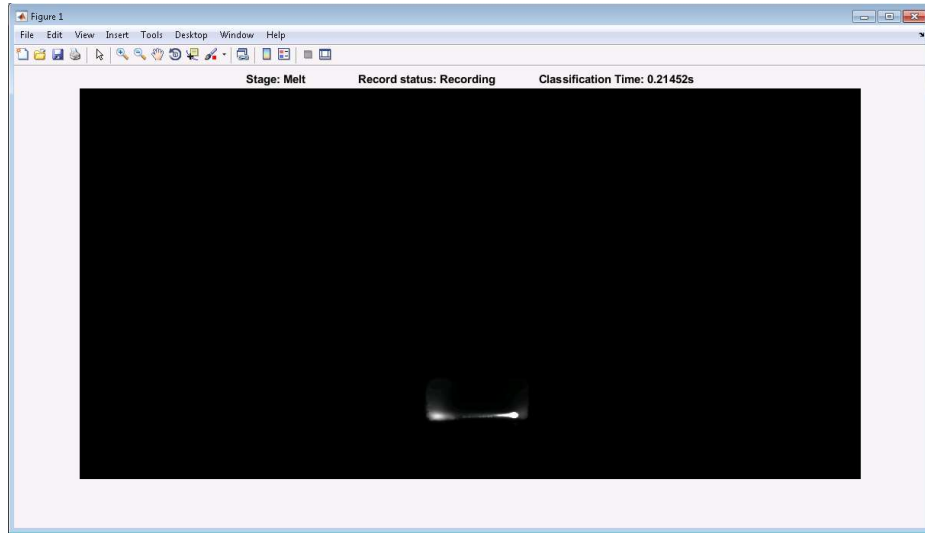


**Figure 4.13** Build stage classification testing in MATLAB

With these patterns defined the real time classification and layer start and end detection was tested on the pre-recorded image sequences. In this test the classification time was taken into account to simulate the data that would be fed to the algorithm from the real system. With a mean classification time of  $\sim 0.2$  s the effective framerate of classification was 5 fps. Therefore, with the pre-recorded data being captured at 100 fps every 20<sup>th</sup> frame was passed to the algorithm. In these tests the algorithm was able to correctly detect the start points of the layers within 2s of the true start and points, that had been determined manually. Figure 4.14 shows an example sequence with manual classifications and the ML classifications, the manually identified recording start and end points are marked (frames 44 and 149) as well as where the algorithm started and ended the recording (frames 51 and 158).

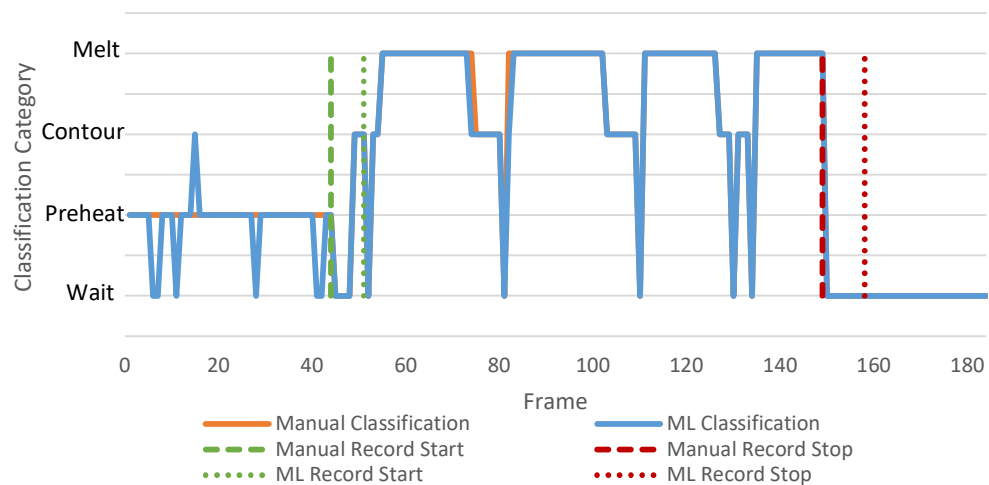


**Figure 4.14** Build stage classifier output example versus manual classification of each frame. Manual versus ML record start and stop frame numbers plotted in dashed lines.

The delay in recording start and end can be expected because a pattern of at least 5 frames was being searched for in the image labels. This meant that the start of the contour phase can be detected, and a capture started by the algorithm within 200 frames of it happening in a build. It is possible to cache this number of frames in real time so even if the algorithm missed the start of the contour it can be recorded from the first image in which it was detected. Missed detections are less of a problem at the end of a layer, but they do need to be detected to allow as much time as possible to write the frames to disk during layer change. This meant that when the end is detected using the longer pattern and the capture stopped, any frames recorded after the last frames detected as a part of the melt can be deleted and not recorded to reduce write times. Unless the final cooling of the layer is needed for the experiment.

The now trained and tested SVM was integrated into the custom capture software, this was accomplished using the MATLAB Engine interface, which allows a C++ program to create and control an instance of MATLAB. Ideally the MATLAB code would be compiled directly to C++ and run natively but some MATLAB features used stopped this. The interface was initialised before a build was started which will start MATLAB and load the model and other required variables. The C++ code was then able to pass images to the classification function in MATLAB and a label for that image is returned. The pattern detection for starting and ending a capture was done in C++ to reduce the amount of time that was spent in MATLAB and the amount of data that was transferred, because of the associated overheads.

The ML system integrated into the capture software was tested with a build, but unfortunately no useful data was acquired due to the build being stopped in the early layers because of a problem causing arc trips on the Arcam. The system did however identify build stages correctly in real time before this happened. Further in situ testing was not able to be completed because of the long-term downtime of the machine after this failure.

#### **4.7 Dissimilar Metals Welding**

The EBM process shares a lot of similarities with Electron Beam Welding (EBW) a process that uses an accelerated electron beam to join materials. Like EBM, EBW is traditionally completed in a vacuum chamber; to allow the highly charged electron beam a clear path to the material without air to deflect or absorb the beams energy. Also like EBM, the position of the workpiece in a vacuum chamber allows processing of more exotic materials and alloys, such as titanium alloys, because of the tendency of such alloys to oxidise at the high temperatures needed for the welding process when conducted in air. The EBW process is used in industrial spaces such as aerospace where titanium alloys are used heavily because of their high strength to weight ratios. The degree of control over the EBW process and

small beam spot that causes very localised heating are very advantageous in such industries because parts can be welded to final size or very close to it without causing damage or stress to the areas around the weld zone.

Despite the advantages that the EBW process provides, there has been limited success in welding dissimilar metals. Experiments conducted in the literature often show brittle joints that would be unsuitable for practical use [23]. Despite this successful welding of titanium (Ti-6Al-4V) to vanadium was shown using the EBM process. To complete this, two titanium and vanadium plates were clamped together (Figure 4.15) and placed on the lowered build plate, to align them with the standard powder bed level. Using the beam alignment settings the electron beam was aligned with the boundary between the two plates in the X direction on the machine. The positioning in the build chamber was also optimal for imaging because of how the frame can be narrowed to achieve higher frame rates on the Hamamatsu camera. An exposure time of 650  $\mu$ s was used with a frame size of 2048x128 allowing a frame rate of 1530 fps.



**Figure 4.15 Clamped and welded and Vandium (top) and Titanium (bottom) plates.**

The thermal imaging setup was used here to give insights into the weld track in progress. This was a difficult process to image because of the multiple materials and phase changes involved, as well as the intermetallic area where the two metals join, in the area of interest. These factors cause an even larger uncertainty in emissivity values versus a standard EBM build; therefore, a fixed emissivity value based on that of titanium was used ( $\epsilon=0.75$ ).

The interesting observations from this series of imaging were the size of the melt pool and temperatures of the area surrounding it, as well as temperature profiles of the weld line. The melt pool size and shape were of interest to further verify that the welding process worked as expected within the Arcam system. A pear-shaped melt pool is expected with

EBW and EBM processes and after applying the emissivity tracking process explained previously to the images, this is what was seen (Figure 4.16).



**Figure 4.16 Emissivity correction algorithm manually applied to welding image. Showing comparison of different threshold values and the 'bumps' seen perpendicular to the direction of travel.**

Across the different weld tracks images melt pool widths of 2-4 mm were found from analysis of the thermal images, this agreed with cross section images of the welds created in post processing. The melt pool shapes that were extracted from the images were very irregular in shape, this has also been seen in some EBM builds when imaging at sufficient frame rates. It hasn't been possible to fully prove the reason for seeing these 'bumps' perpendicular to the direction of travel of the e-beam; but in this case it is possible that they are reflections of the point the beam is interacting with in the melt pool from the surface of the molten pool because of its concave shape (seen in the cross section images in Figure 4.17). These areas were not counted when making measurements of the melt pool in this case.

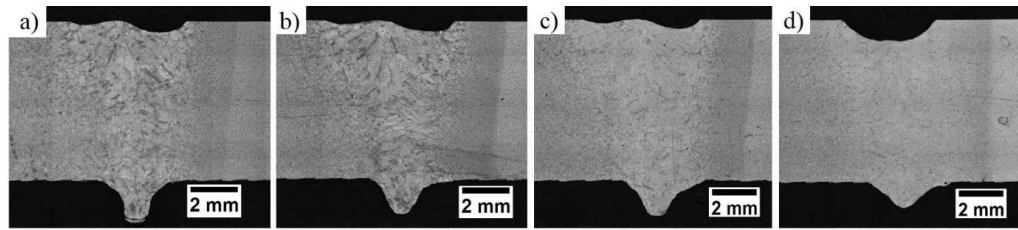


**Figure 4.17** Weld cross sections for various beam currents a) 31 mA, b) 33 mA, c) 35 mA and d) 37 mA, all using 7 mm/s beam speed

The temperature profiles running through the melt pool along the length of the weld were also of interest. A profile run along the weld from a single image gives a snapshot of the state of the weld and the change from the pre-weld area through the melt pool, to the cooling welded area can be investigated. The pre and post melt pool areas are of particular interest in this case. To achieve good quality in this kind of weld the material needs to be heated prior to being welded by the e-beam. In other areas and processes this is done with a dedicated preheat treatment or the overall power of the welding method is enough to suitably preheat the material in place before it is welded [24]. The profiles from the thermal imaging showed that this was also the case in this experiment. On the profiles shown in Figure 4.18 an area of approximately 3-4 mm can be seen to be heated before the plateau of the melt pool.

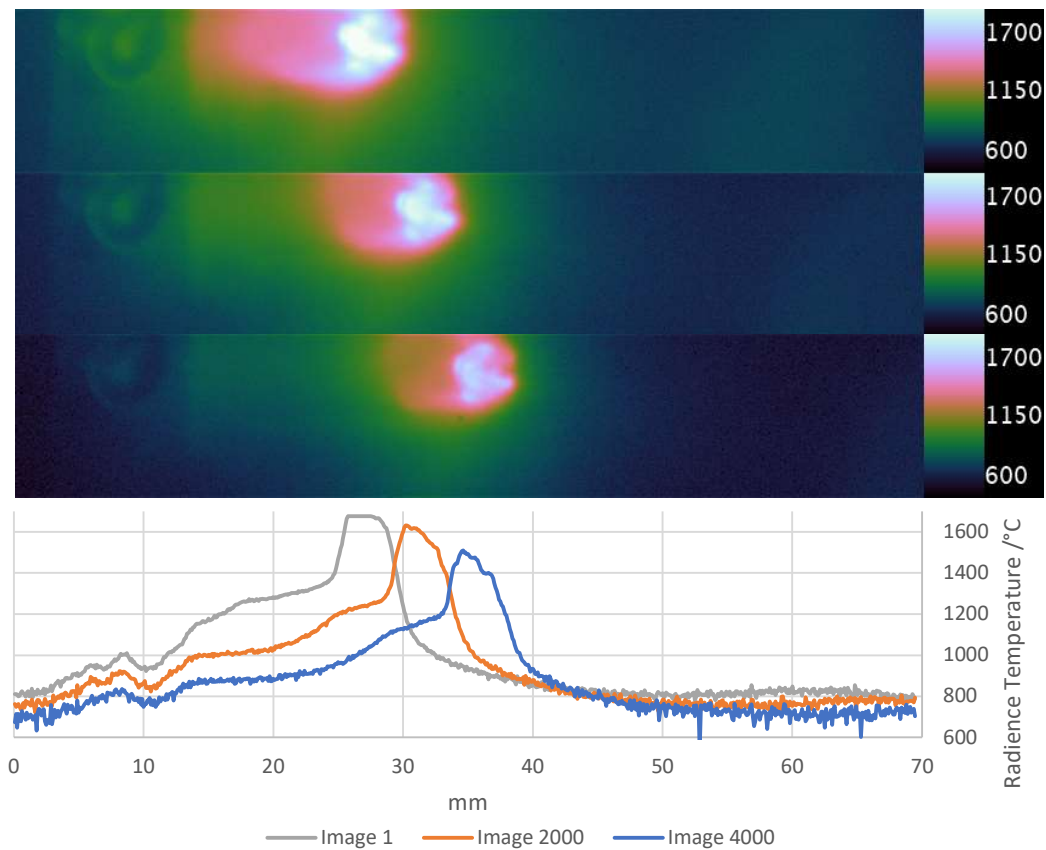


**Figure 4.18** Welding images with temperature profiles

Even without knowing the exact temperatures because of emissivity uncertainties the fact a heated area ahead of the melt pool can be identified was a very good indication that the EBM process is performing well when used as EBW and that a good weld was taking place.

In the future, with more weld samples, the thermal imaging setup on the Arcam will be able to assist the development of dissimilar metal welding. The in-situ information that can be collected using the thermal imaging setup can assist with beam parameter tuning, meaning better melt pool parameters such as size and shape and ultimately a better weld.

#### **4.8 Conclusion**

This chapter has shown further development of the imaging system designed and tested in the previous chapter. Analysis methods for part property investigation and in situ porosity measurement have been shown based on thermal images captured with the system. These are some of the analysis types that would be possible with this kind of thermal imaging data. With more refinement and development, the accuracy of the techniques could be improved, and the analysis run in real time for immediate feedback to an operator or process control system. One of the key challenges to thermal imaging in an AM environment was addressed with the emissivity tracking algorithm. This is able to correct for emissivity on a frame by frame basis based on the state of the material at all locations in frame. The algorithm is able to reduce the effect of the biggest source of error for a thermal imager. Integration of the imaging system with the EBM machine was also shown; a machine learning algorithm was developed to detect key events in a build and trigger image capture based on them. This will help decrease the amount of data captured by only recording important parts of the build, it could also be used in the future to inform analysis. Finally, this chapter discusses dissimilar metals welding via electron beam welding and how with the use of the thermal imaging setup the preheat zone could be identified. This preheat is key to the performance of EBW especially when welding dissimilar metals. The identification of the preheat zone was an indication of a good weld and would not have been possible without this kind of in situ monitoring.

- [1] L. E. J. Thomas-Seale, J. C. Kirkman-Brown, M. M. Attallah, D. M. Espino, and D. E. T. Shepherd, "The barriers to the progression of additive manufacture: Perspectives from UK industry," *Int. J. Prod. Econ.*, vol. 198, pp. 104–118, Apr. 2018.
- [2] C. Bisu, A. Gerard, M. Zapciu, and O. Cahuc, "The Milling Process Monitoring Using 3D Envelope Method," *Adv. Mater. Res.*, vol. 423, pp. 77–88, 2012.
- [3] R. Teti, K. Jemielniak, G. O'Donnell, and D. Dornfeld, "Advanced monitoring of machining operations," *CIRP Ann.*, vol. 59, no. 2, pp. 717–739, Jan. 2010.
- [4] Q. Y. Lu and C. H. Wong, "Additive manufacturing process monitoring and control by non-destructive testing techniques: challenges and in-process monitoring," *Virtual Phys. Prototyp.*, vol. 13, no. 2, pp. 39–48, Apr. 2018.
- [5] ASTM, "Tension Testing of Metallic Materials," *ASTM International*, no. C. pp. 1–27, 2016.
- [6] C. de Formanoir, S. Michotte, O. Rigo, L. Germain, and S. Godet, "Electron beam melted Ti–6Al–4V: Microstructure, texture and mechanical behavior of the as-built and heat-treated material," *Mater. Sci. Eng. A*, vol. 652, pp. 105–119, Jan. 2016.
- [7] O. N. Senkov, J. J. Valencia, S. V. Senkova, M. Cavusoglu, and F. H. Froes, "Effect of cooling rate on microstructure of Ti-6Al-4V forging," *Mater. Sci. Technol.*, vol. 18, no. 12, pp. 1471–1478, Dec. 2002.
- [8] S. S. Sih and J. W. Barlow, "The prediction of the emissivity and thermal conductivity of powder beds," *Part. Sci. Technol.*, vol. 22, no. 4, pp. 427–440, 2004.
- [9] Arcam AB, "Ti6Al4V Titanium Alloy Datasheet." [Online]. Available: <http://www.arcam.com/wp-content/uploads/Arcam-Ti6Al4V-Titanium-Alloy.pdf>. [Accessed: 15-Feb-2019].
- [10] K. Heim, F. Bernier, R. Pelletier, and L. P. Lefebvre, "High resolution pore size analysis in metallic powders by X-ray tomography," *Case Stud. Nondestruct. Test. Eval.*, vol. 6, pp. 45–52, Nov. 2016.
- [11] L. González-Fernández, E. Risueño, R. B. Pérez-Sáez, and M. J. Tello, "Infrared normal spectral emissivity of Ti-6Al-4V alloy in the 500-1150 K temperature range," *J. Alloys Compd.*, vol. 541, pp. 144–149, Nov. 2012.
- [12] A. Thompson, S. Tammis-Williams, N. Senin, I. Todd, and R. Leach, "Correlating volume and surface features in additively manufactured metal parts," in *Proceedings - 2018 ASPE and euspen Summer Topical Meeting: Advancing Precision in Additive Manufacturing*, 2018, pp. 116–120.
- [13] D. Borland and R. M. Taylor, "Rainbow color map (still) considered harmful," *IEEE Comput. Graph. Appl.*, vol. 27, no. 2, pp. 14–17, Mar. 2007.
- [14] D. A. Green, "A colour scheme for the display of astronomical intensity images," *Bull. Astron. Soc. India*, vol. 39, no. 2, pp. 289–295, 2011.
- [15] S. Cobeldick, "CubeHelix Colormap Generator: Beautiful and Versatile! - File Exchange - MATLAB Central." [Online]. Available: <https://uk.mathworks.com/matlabcentral/fileexchange/43700-cubehelix-colormap-generator-beautiful-and-versatile>. [Accessed: 28-Mar-2019].
- [16] The Qt Company, "Qt | Cross-platform software development for embedded & desktop." [Online]. Available: <https://www.qt.io/>. [Accessed: 09-May-2019].

- [17] OpenCV Team, "OpenCV." [Online]. Available: <https://opencv.org/>. [Accessed: 09-May-2019].
- [18] J. Ahrens, B. Geveci, and C. Law, "ParaView: An end-user tool for large-data visualization," in *Visualization Handbook*, C. M. Hanson and C. R. Johnson, Eds. Elsevier, 2005, pp. 717–731.
- [19] Samsung UK, "2TB SSD 850 PRO SATA III 2.5 inch MZ-7KE2T0BW | Samsung UK." [Online]. Available: <https://www.samsung.com/uk/memory-storage/850-pro-sata-3-2-5-inch-ssd/MZ-7KE2T0BW/>. [Accessed: 13-Apr-2019].
- [20] U. Delli and S. Chang, "Automated Process Monitoring in 3D Printing Using Supervised Machine Learning," *Procedia Manuf.*, vol. 26, pp. 865–870, Jan. 2018.
- [21] I. Goodfellow, Y. Bengio, and A. Courville, "Learning Algorithms," in *Deep Learning*, Cambridge, Massachusetts: The MIT Press, 2016, p. 775.
- [22] H. Bay, A. Ess, T. Tuytelaars, and L. Van Gool, "Speeded-Up Robust Features (SURF)," *Comput. Vis. Image Underst.*, vol. 110, no. 3, pp. 346–359, Jun. 2008.
- [23] H. . Chung, J.-H. Park, R. . Strain, K. . Leong, and D. . Smith, "Mechanical properties and microstructural characteristics of laser and electron-beam welds in V–4Cr–4Ti," *J. Nucl. Mater.*, vol. 258–263, pp. 1451–1457, Oct. 1998.
- [24] W. Zhang *et al.*, "Influence of multi-beam preheating temperature and stress on the buckling distortion in electron beam welding," *Mater. Des.*, vol. 139, pp. 439–446, Feb. 2018.

## **5 Gas Tungsten Arc Welding Thermal Imaging and Analysis**

### **5.1 Introduction**

This chapter details the experiments involving thermal imaging as a sensor input for a robotic welding system. It draws on work done in previous chapters with electron beam melting, using a very similar camera setup. Multiple welding setups are shown with analysis of the thermal data that could be useful in an automated welding setup as a feedback mechanism. The analysis techniques are working towards full automated detection of thermal events that would inform in situ weld quality measurements and real time feedback.

### **5.2 Turbine Blade Imaging**

As with recent commercial increase of the use of Electron Beam Melting (EBM), Gas Tungsten Arc Welding (GTAW) is increasingly being used as an AM process. Here it was used for the repair of turbine blades on aerospace jet engines. There is research underway to automate the repair process, traditionally completed by highly skilled welders. The reason for automation was the current high rate of defects and repairs failures, meaning turbine blades cannot be reused. The repair process involves the welding of new layers of material onto the blade tips, where the wear takes place. It is then machined to match the original blade profile and heat treated and coated ready for reuse. Approximately 85% of blades recovered from service can be repaired, however only 50% of those blade repairs are successful[1]. The research into automation aims to use sensor systems tightly integrated with robotic welding to decrease this failure rate.

Thermal imaging has been evaluated as a potential sensor for input into the control system for the robotic welding. As a part of this process thermal imaging has been tested on turbine blade blanks. The use of blanks was required because of the expense and relative scarcity of the Inconel blade components. The representative blanks were made from a similar austenitic nickel-chromium based steel alloy, 316L stainless steel and were formed into the profile of the blade. The remainder of the welding setup was kept the same as would be used on real components.

The thermal imaging setup was of particular interest to this application because of its ability to monitor a large number of points over an area versus contact or single point contactless solutions. The blade repair process requires very specific heat input from the welding system in order not to damage the blade. The thin tip of the blade requires a low rise in temperature so not to detrimentally effect the properties of the tip where large forces are seen during use. The welding setup was designed to minimise heat build-up by using a high frequency pulsed DC GTAW welding system. This system monitors and closely controls the weld current in conjunction with its heat management system. Depending on the investigation being carried out the thermal imaging system could be configured to

monitor a large area of the blade tip or to focus on the weld bead, allowing the potential for simultaneous monitoring of blade temperature and weld temperatures.

The robotic welding setup used a fixed position for the GTAW torch and moved the workpiece therefore, the camera was easily positioned externally and perpendicular to the direction of travel of the workpiece. It was focused on the tip of the torch and the surrounding area. The setup can be seen in Figure 5.1. A longer working distance and smaller field-of-view were required than with the EBM setup so an off the self DSLR lens with a focal distance of 180 mm was used. This achieved a field-of-view of 12 mm x 6 mm using a resolution of 1024x512 pixels, the reduced resolution was used to increase the framerate of the camera and to reduce dataset size. A 950 nm centre wavelength, 10 nm wide bandpass filter was used to block non NIR wavelengths and was selected to be in a low emission area of the welding arc [2]. To protect the lens and camera setup a piece of shade 9 welding shield was used. When measured this was transparent at the cameras working wavelengths but was included in any calibrations for completeness.

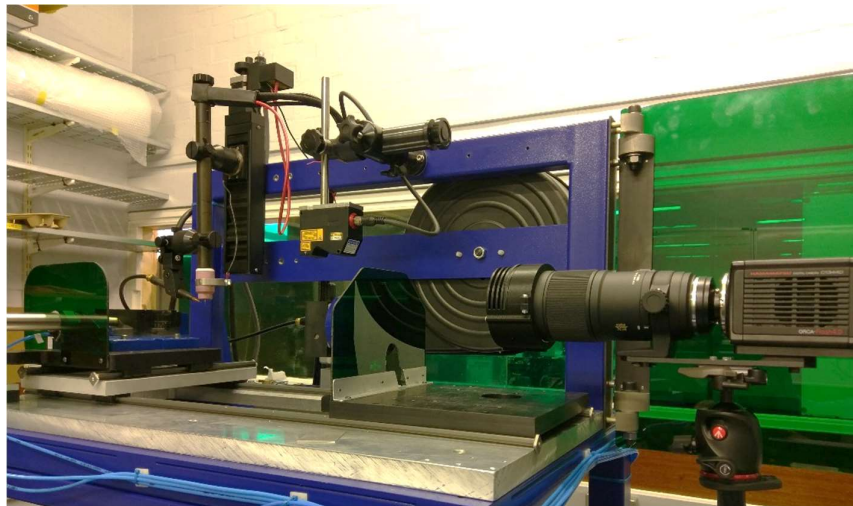


**Figure 5.1 GTAW thermal imaging camera setup**

The camera and lens setup was calibrated for a radiance temperature range of 700-1500 °C, with the full range being 700-2400 °C, (calibration curve shown in Figure 5.2) using the procedure detailed in chapter 3. A 5 mm aperture was used on the furnace opening after a lot of reflections were found when using this lens with large bright areas. This was found when running the size of source effect (SSE) measurements for the setup. Whereas an SSE curve would normally flatten and tend to the true radiance value with the larger the object it measured, here the apparent radiance continued to rise. This could be an effect of reflections due to the size and glass of the lens used. The lens was chosen for the field-of-view it could produce from the working distance required. In this respect the off-the-shelf availability and standard mounting type worked well, however, it is designed for use in the visible wavelengths, not the near infrared. This means the anti-reflective (AR) coating that

was applied may not be effective at the 950 nm working wavelength used here. The incorrect AR coating could cause more light at the working wavelength to be reflected internally within the lens, between optical elements [3]. When reflecting back towards the sensor some of this light will pass through the lens and hit the sensor, because of the internal reflections it will hit the sensor in a different location. This can cause ghost images, or in this case a 'blurring' of the image where bright spots appear larger and more defuse.

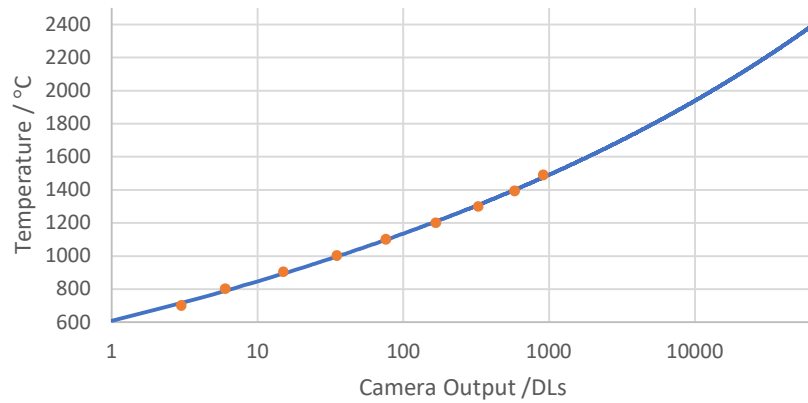


**Figure 5.2 GTAW turbine blade camera calibration curve**

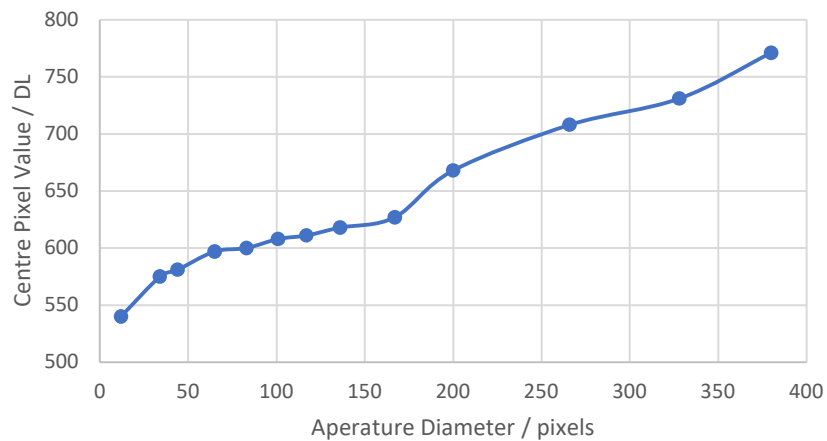


**Figure 5.3 GTAW camera setup size of source effect plot**

The SSE measurement is traditionally used with a single point detector to determine the effect the size of a bright object has on apparent radiance values. It is used here to determine the smallest area of pixels that should be trusted as a true radiance measurement, but also shows the effect of internal reflections. The SSE data in Figure 5.3 flattens between 60 and 170 pixels, this flattening is the expected behaviour; the rise in DL values above this is the effect of reflections. The drop off below 34 pixels shows the effect of a small sources energy being spread over an area of the sensor because of the non-ideal optical setup. This occurs in all real optical systems, with only a perfect system achieving a

flat line in this test. In terms of imaging this shows that small objects < 34 pixels in diameter will appear cooler and objects > 170 pixels will appear hotter.

A selection of thermal images can be seen below in Figure 5.4, these are frames with interesting features selected from a single weld. Images A and B show the formation of a bubble of molten material on the blank before any filter material is introduced. Also, in these two frames spots of slag can be seen on the surface of the molten material, the movement of these spots show the currents within the molten material. In image C the blank has started to move and filter material is starting to be introduced, the cooled bubble from A and B can also be seen. Image D is mid weld and shows the cooling profile of the weld in steady state. Images E and F show the end of the weld, with the filler added in E and the cooling of the weld in F.

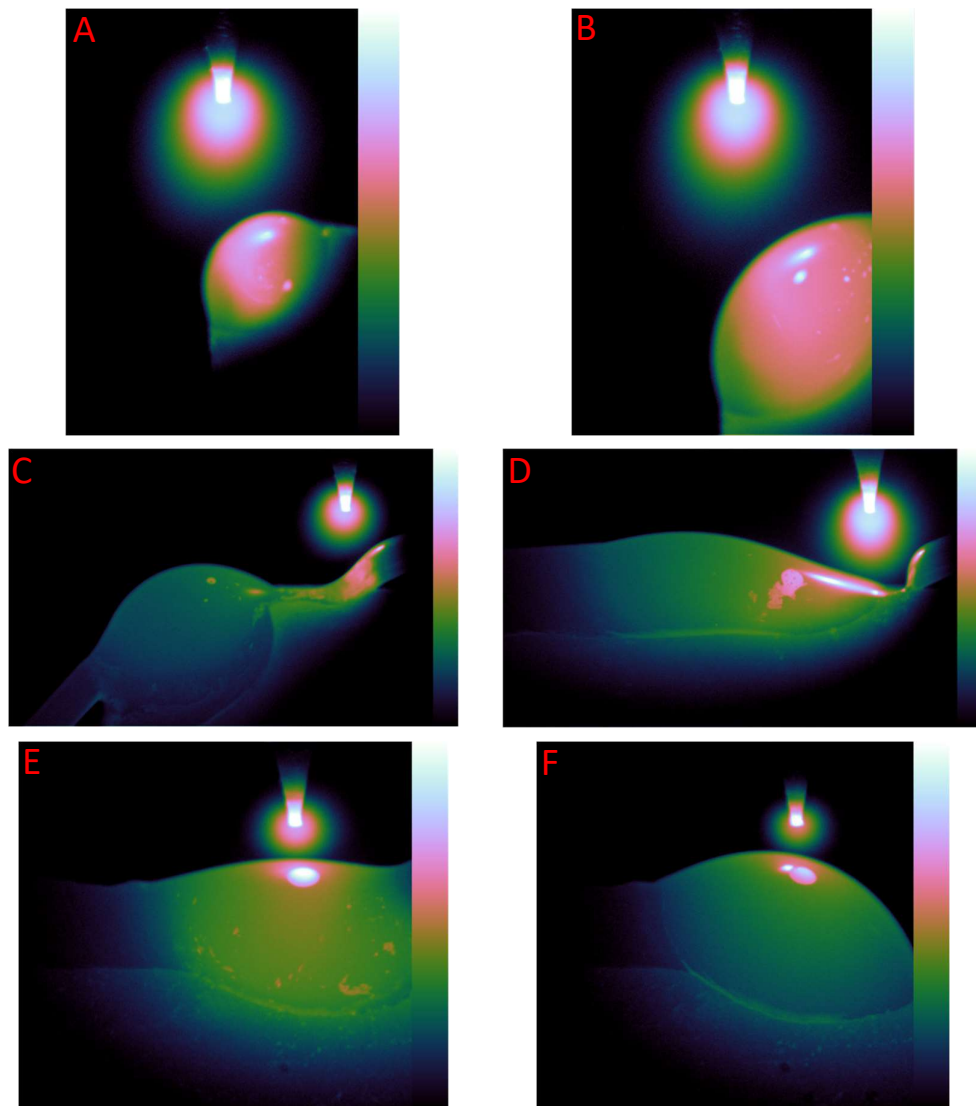


Figure 5.4 Turbine blade image example thermal images. Colourmap scale 1300-2200 °C

### 5.2.1 Freezing Point Detection

One metric that was investigated with analysis of the thermal images is the freezing point of the weld. The freezing point of a material can reveal information about its properties such as its composition and grain structure. The freezing points of some pure metals are well known and used to define the ITS-90 temperature scale and are used to calibrate infrared instruments to that scale [4]. The freezing point of a material can be identified in a thermal measurement by finding the freezing plateau in a cooling curve. When a material transitions from liquid to solid phase there is a release of energy caused by the transition. This latent heat of solidification is caused by the making of bonds to form a solid [5]. This release is apparent when observing the cooling curve and seen as either a plateau in cooling or a slight rise in temperature when the material solidifies. Whether there will be a temperature plateau or rise depends on the materials molar heat of solidification and the rate at which the freezing point is transitioned through [6].

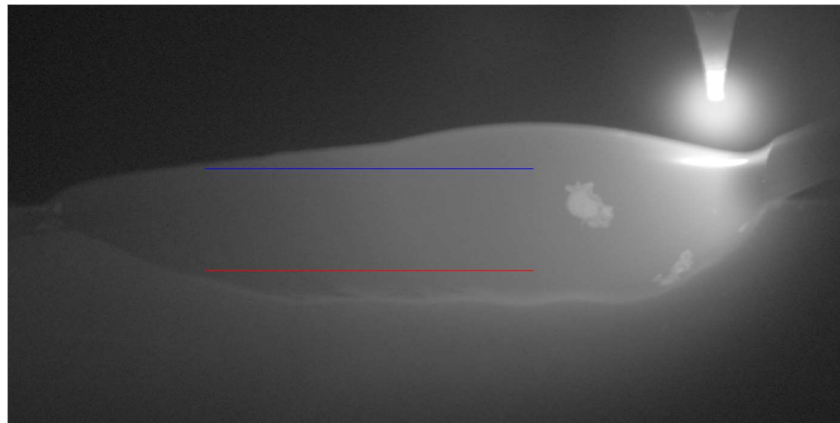


Figure 5.5 Location of cooling profiles on weld bead

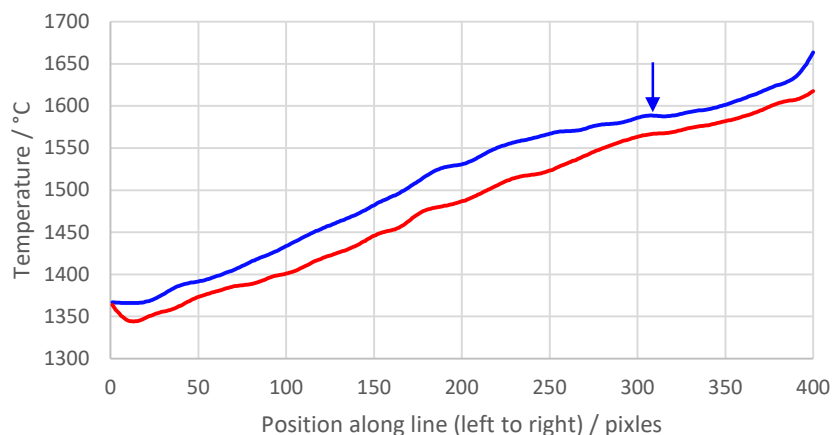
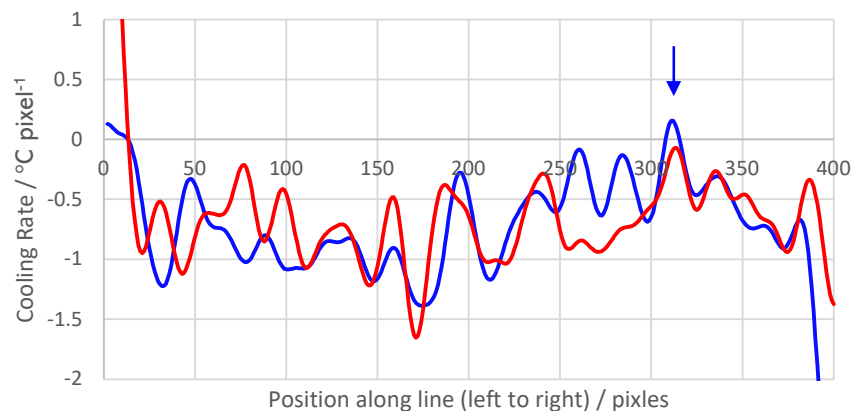


Figure 5.6 Comparison of cooling profiles, showing possible freezing plateau location

When using thermal imaging cooling rate images can be created by using the difference in temperature between each frame from a sequence of images; these would be analogous

to a cooling rate curve from a single point IR measurement device for each pixel. However, in the turbine blade images because the workpiece was moving in frame and heated in a constant location the entire cooling region can be seen in one frame. Therefore, a cooling profile and cooling rate curve can be obtained by sampling pixels along the direction of travel. Figure 5.5 shows this location on a thermal image and Figure 5.6 show the corresponding temperature plot. The cooling of the weld happened from right to left on the image and this was seen on the temperature curves, these curves have been low pass filtered to remove high frequency pixel to pixel noise. Neither of these curves show strong signs of a freezing plateau, even though by observation of the thermal image sequence the weld was known to solidify in the region. This was shown further by the cooling rate plot (gradient of the temperature profile) in Figure 5.7, a 0 or positive value here would be an indication of freezing. Other than at the extremes of the data only the top (blue) line has a slight positive gradient (location marked with arrow), this was a weak indication of freezing but there was nothing on the lower line (red). One reason for there being a more pronounced freezing location towards the top of the weld would be the greater heat sinking effect of the blade on the weld at the bottom compared to the top. There is also argon purge gas blown on the part from below which only occurs near the torch head on top.



**Figure 5.7 Comparison of cooling rates along the two profiles**

The method of looking for a plateau in a single point temperature measurement plot is primarily designed for use with contact or single point IR measurements. A more robust way of finding the freezing point was developed by leveraging the amount of data captured in a thermal image. The relatively large area of the image that was filled by the cooling weld was used to implement a multiple threshold method of detecting the freezing point.

The method works by; cropping the image to the area containing the cooling weld, removing the very bright electrode and cool areas surrounding the workpiece (Figure

5.8.A). A threshold was applied to this area every 5 °C (thresholds every 10 °C shown in Figure 5.8.B for clarity), this created a series of binary threshold images with temperatures between the threshold value and the maximum selected. The number of pixels in the selected area in each threshold image was calculated and plot against the temperature range from which the threshold was created. The gradient of this curve was calculated and any peaks in it identified (Figure 5.8.B, selected peak identified in red). A peak in this curve was an identifier for a potential freezing point location in the same way as a positive gradient on the cooling rate curve above is. If the curve has multiple peaks, they are evaluated by calculating the absolute value of the top of the peak and its proximity to the last detected freezing point (on the previous image). With the proximity to the last freezing point used to weight the absolute values of the peaks, the lowest value peak was determined as the freezing point. The weighting with the relative distance to the last peak was used because the camera is run at a sufficiently high frame rate that versus the travel of the workpiece that unless there is an anomaly in the weld or external factors the position of the freezing point should be relatively constant.

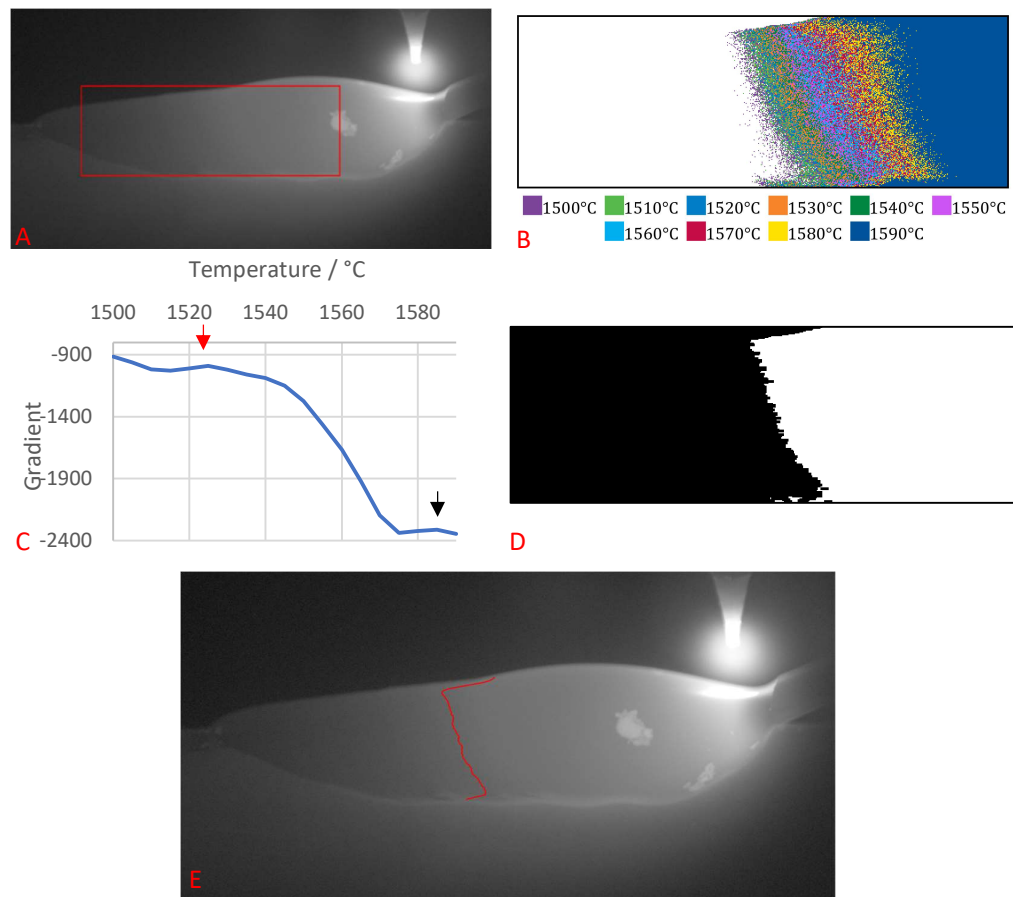
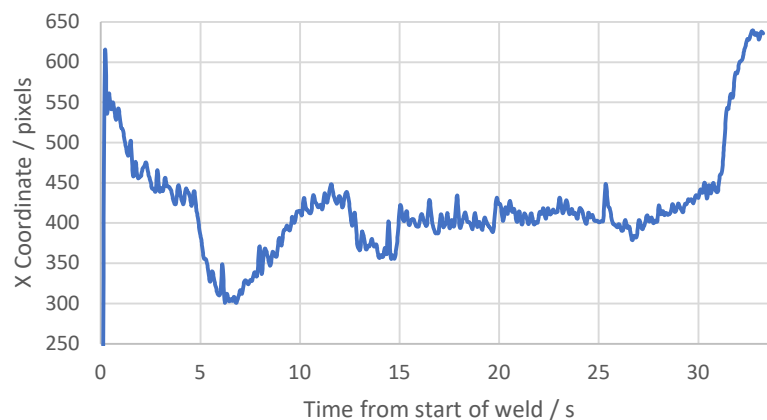


Figure 5.8 Freezing point identification steps; A: region of interest, B: thresholding by temperature, C: identification of temperature gradient peak, D: selected peak threshold image, E: processed freezing point overlaid in position on original thermal image

Using the most likely peak the threshold image to be used was determined (Figure 5.8.D). The left edge of the selected area in the threshold image was used as a starting point for the identification of the solidification point. A series of morphological operations are performed on the mask to remove noise and smooth the edge; fill, close and erode operations are performed. These remove any areas that may have been selected incorrectly by the threshold, for example, those that aren't connected to the main area on the right. This process was important as the left most pixel on each row was selected as being the freezing point on that row. The freezing points for each row are then filtered with a moving average to remove high frequency components that are likely artefacts of the image processing and any remaining noise. The final freezing point line can be seen overlaid on the image in Figure 5.8.E. A flow chart of this process is shown at the end of the section in Figure 5.11. The MATLAB code that implements the freezing point detection algorithm is listed in appendix 7.2.

Using this analysis technique, the image sequence showing the full weld track was analysed. This gave a history along the full weld track of the detected freezing point, with the work piece moving approximately  $22.5 \mu\text{m}$  between each frame. From this data a location of the freezing point in the image coordinate space can be calculated. The mean X value of the curve in the image coordinate space was then used to plot the location of the freezing point with time. This data was lowpass filtered to remove high frequency spikes in the location caused by the algorithm detecting the edges of slag floating on top of the molten pool as the freezing point because of the apparent high change in temperature (Figure 5.9).



**Figure 5.9 Position of freezing point along the weld with time (measured from torch X location)**

The low starting point on the data is an artefact of the lowpass filter used. When analysing the frequency content of the mean X location data peaks at 1 Hz and 2 Hz are seen. This frequency correlates to 0.9-1.8 mm movement of the blank. This scale of feature can be seen on the weld bead in multiple places across the test blanks (Figure 5.10).

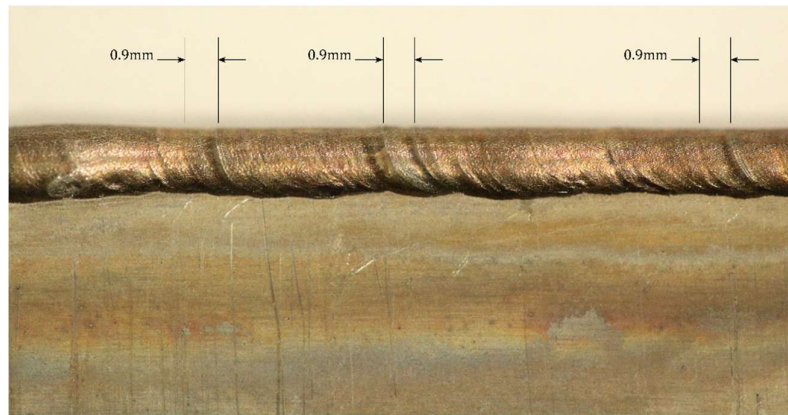


**Figure 5.10 Picture of weld bead showing 0.9 mm features correlating to the frequencies seen in the position of the freezing point**

As can be seen in Figure 5.10 the majority of the weld bead, especially towards the top edge, is smooth; this is considered a good visual indicator for a good weld. However, towards the lower edge and across the full bead in places ripples can be seen, which is an indicator of a possible weld defect. The ripples corresponded to the size of feature detected by the freezing point analysis. This shows potential defects being detected with this analysis method. There are multiple reasons why a ripple can form in a weld bead, most of which relate to the imbalance of pressure in the molten weld pool. There have been multiple explanations for this ranging from the composition of the molten material at that specific point, power supply oscillations and variations, variations in solidification growth rate due to thermal variation [7], [8].

With the identification of potential defect locations high speed thermal imaging will be a valid option for online weld analysis and control. This system has already started to be incorporated into future robotic welding setups focused on developing real time control. When combined with other real time sensors, such as current and voltage meters, this kind of imaging setup could identify the effects of power supply variations on weld quality. It has also been used as a valuable real time feedback mechanism for the operator running welding trials whilst setting up these robotic welding systems. A real time temperature image of a weld bead in progress can inform someone much more than a view through a welding visor.

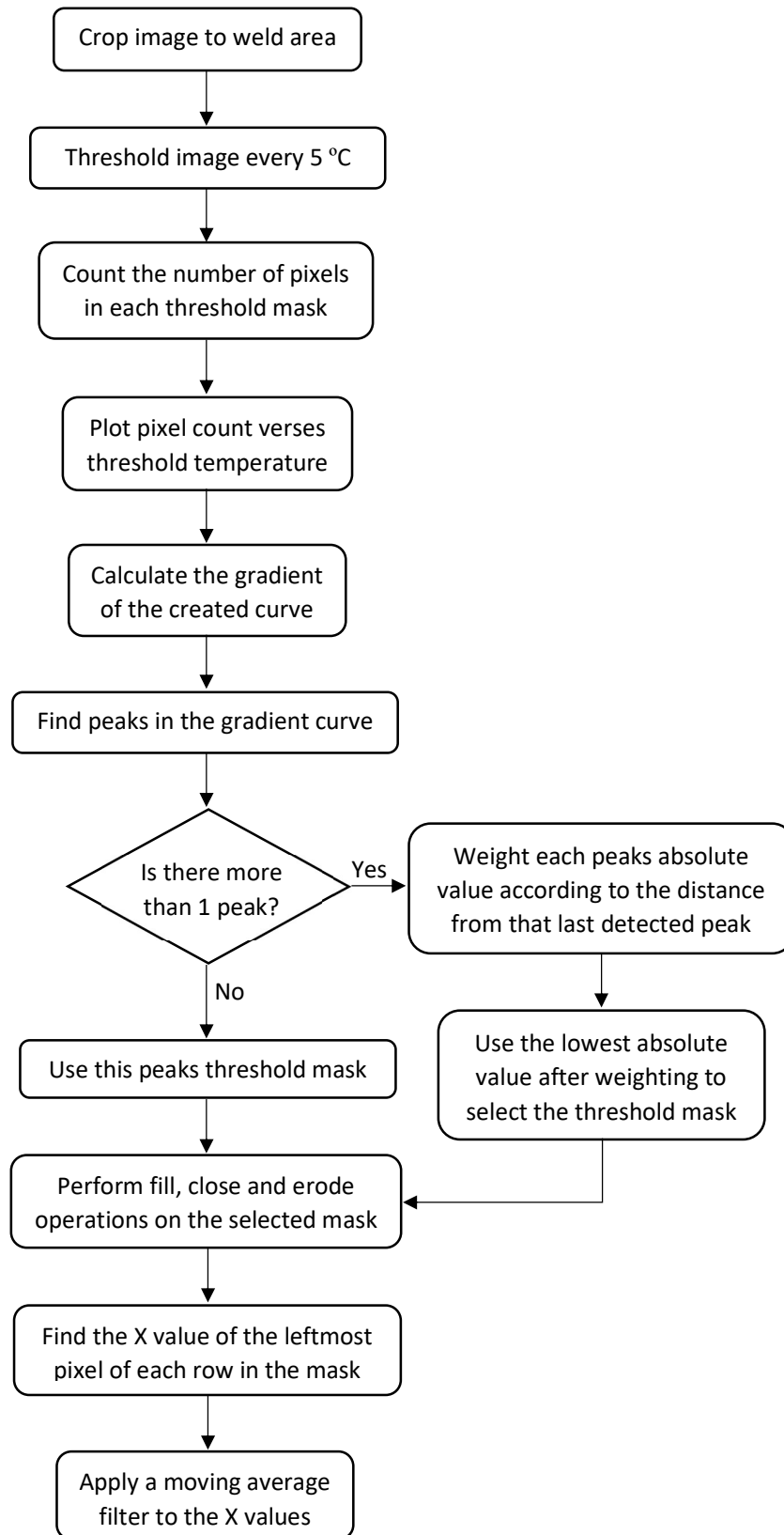


Figure 5.11 Flow chart of freezing point detection process

### 5.3 Pipe Welding Slag Detection and Tracking

GTAW is commonly used in industrial processes to join pipe sections and create pipe networks like fuel distribution systems. Here thermal imaging was used to image the weld pool on a robotic pipe welding system similar to that used in the section above. The camera was positioned to have a view of the side profile of the weld and the cross section of the pipe. The focus of the imaging was high resolution, high speed thermal imaging of the weld pool to look at the dynamics of the molten material.

To gain insight into how the weld pool was behaving and how the weld was moving whilst still molten areas of slag floating on top of the weld were used. Slag is formed on a weld bead when impurities are encountered along the weld track; this could be on the surface of the work piece, such as surface oxidation, or pockets of impurities in the work piece itself. Another reason is the flux used to prevent oxidation during the weld, the flux, with proper technique, should rise to the top of the molten weld pool and depending on the amount form a layer over the top of the weld when cooled. The slag rising to the top of the molten pool is the process relied on for this method. Slag spots can also be indicators of impurities in the weld and tracking them in this way could give insight into the quality of the weld[9].



**Figure 5.12 Pipe welding thermal imaging setup**

To capture thermal images with a framerate as high as possible the camera was set up with a 2048x512 region of interest and a 2.5 ms exposure time. The same 950 nm filter was used as above but with an f/7.1 aperture, allowing a temperature range of 700-2190 °C. The 2.5 ms exposure time allowed a 400 frames per second capture.

A selection of example thermal images captured from a single run using this setup are shown in Figure 5.13. Image pairs A, B and C, D each show filler being added to the weld pool. In images A and C, the molten tip of the filler rod can be seen and in A specifically its reflection can be seen on the surface of the weld pool. In images B and D, the interaction

between the filler and the weld pool can be seen. The shape of the pool changes considerably during this period, becoming longer and flatter due to the surface tension of the molten material. Mainly in image C and D, the cooling of the weld pool can be seen as the pip rotates anticlockwise. In all 4 images slag can be seen floating on top of the weld pool, which of interest for this analysis.

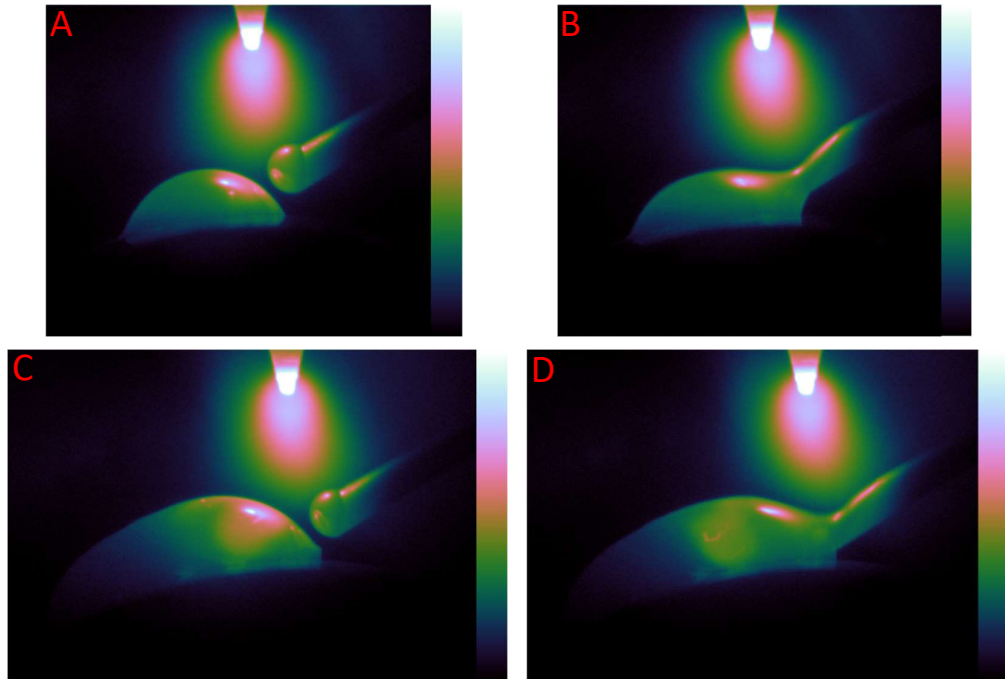
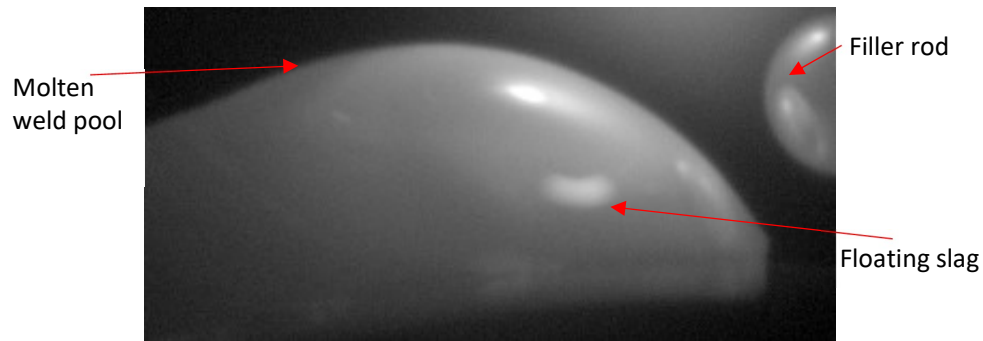


Figure 5.13 Example pipe welding thermal images. Colourmap scale 1000-2000 °C

A section of 100 images was used to develop the analysis technique. This is a small sample considering the framerate, but the sample was visually representative of the features across a whole dataset. The analysis was developed with the intention of being run on a full dataset and was shown to work on other samples as well as the development dataset. A region of interest was manually selected for the analysis which contained just the weld pool, this could be automated in the future with, for example, the process shown in section 5.4. Figure 5.14 shows an annotated example of the cropped region.

The analysis technique revolved around tracking the floating slag on the weld pool. However, due to the dynamic nature of the weld pool any other movement also needed to be accounted for. To detect the whole weld pool a threshold was applied, this simple technique worked because the weld pool was much hotter than the background. This created a mask that could be used as a region of interest for further operations. Next, differential images were created by selecting only areas that changed between 2 consecutive images, these were also thresholded to find only rapidly changing areas. This was done in both directions creating 2 sets of images one that highlighted rapid positive changes in temperature and one negative. Using the rapid temperature changes in both

positive and negative was what made the method robust against other movement and interactions or hot spots.



**Figure 5.14** Cropped region of interest showing the weld pool and slag feature to be tracked for the analysis

On each of these sets of images a blob detection algorithm was run to find the first location of the slag spot on the surface of the weld pool. The parameters for the shape and size were manually tuned but could be automated in the future with methods like that presented in 5.4. Once the first location of the slag spot was found further detection was limited to a small area around that location. This was done by cropping the image around the centroid of the detected spot in the last image. This limited the tracking to only one spot at once but accounted for the amount a spot should move between frames and made it robust to the spot moving through other bright areas, like the reflection of the electrode tip.

Once a list of potential slag spot centroids had been created for each of the two thresholded differential image sets they were compared to create a track of the actual spot moving on the weld pool. This step made sure only the moving slag spot was the object being tracked. By comparing the location of a centroid from the negatively thresholded images with the centroid from the next frame of the positively thresholded set, only an object moving along the same track in both sets of images is detected. If the locations of the centroids were within a 10-pixel radius of each other then, the location was added to the track. If they were within a 50-pixel radius then an extra check was performed to check for the shape of the spot and it was only added if the perimeter shapes matched within 50 pixels. This second check was added to catch valid detections when the spot would interact with the edge of the weld pool and was obscured from view. This would move the centroid more than expected, but the visible portion of the spot would be the same shape as the last. A flow chart of this process is shown below in Figure 5.15. The MATLAB code that implements the slag detection and tracking algorithm is listed in appendix 7.3.

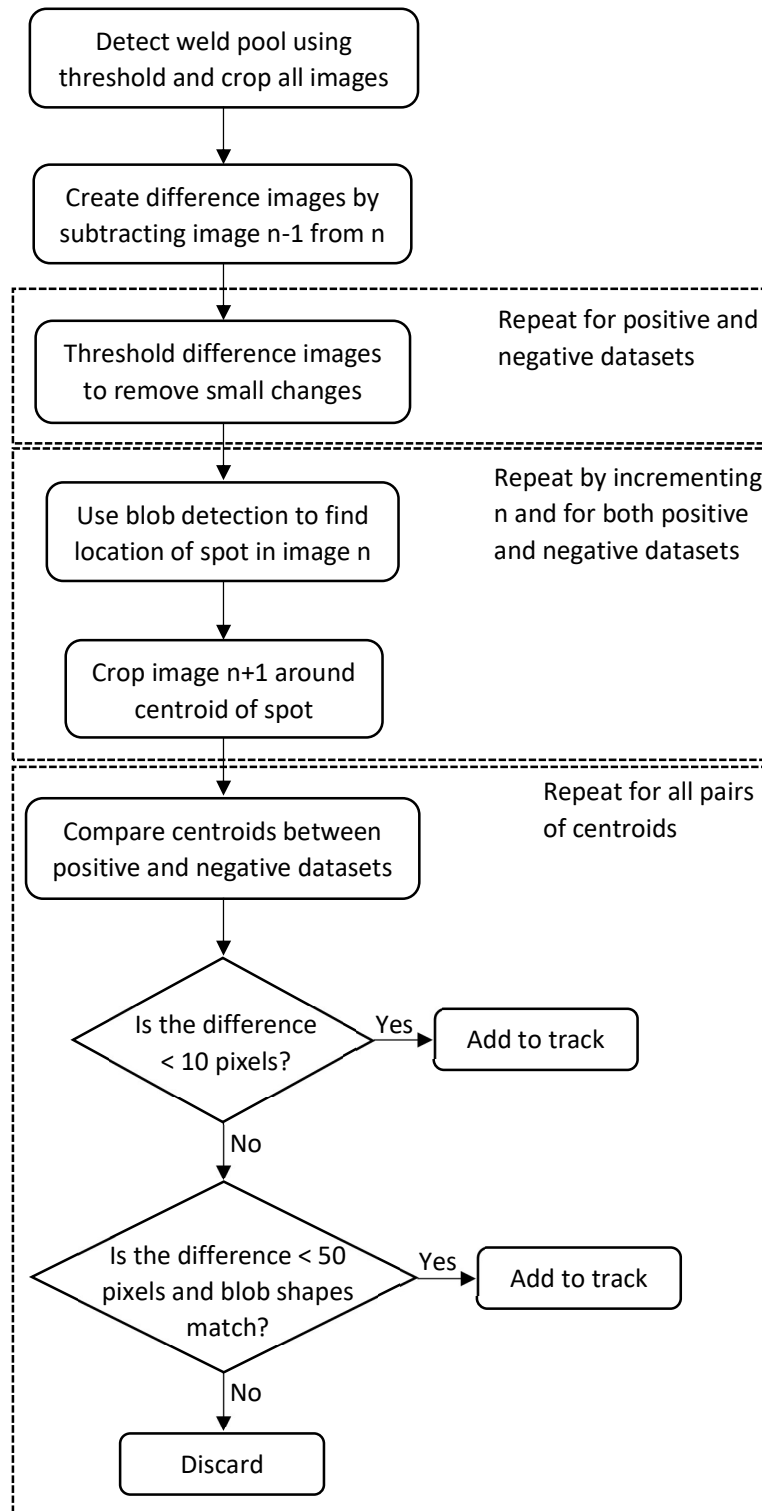
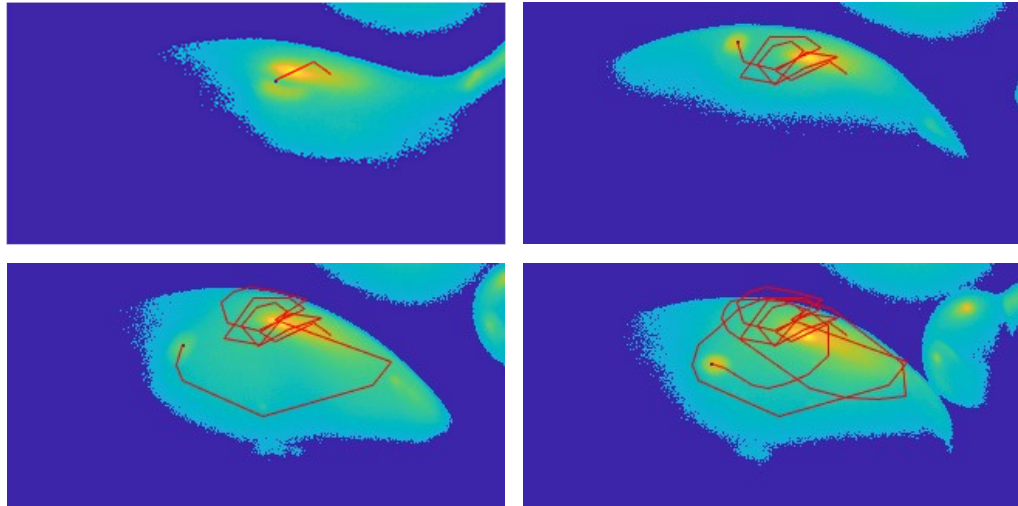


Figure 5.15 Flow char of slag detection process

An example track progression is shown in Figure 5.16. From this track data the velocity of the spot could be calculated using the time between frames and the number of pixels moved. Pixel size was calibrated using the electrode diameter because this was a known and well-defined size within the image. With a inter frame time of 2.5 ms and pixel

calibration of 72.2 pixels/mm velocities of up to 0.22 m/s were calculated. The values ranged from 0.03-0.22 m/s on all the sample sequences tested, with mean velocity being 0.09 m/s. These values are slightly lower than simulated values of weld pool fluid velocity in literature which range from 0.18-0.32 m/s[10]. However, the weld conditions simulated were not exactly the same as this test, the simulated voltage was lower and current higher.



**Figure 5.16 Slag tracking example frames; showing the path a small area of floating slag takes on the weld pool surface**

With more experimentation and refining of the tracking technique this analysis method, provided by thermal imaging, could give more insight into the dynamic welding process and allow models to be validated against real-world testing.

#### **5.4 Machine Learning for Automated Detection and Measurement**

Machine learning, as already presented in earlier chapters, is becoming an increasingly useful tool for data analysis and point of interest identification. It is being applied in a large number of areas, many of which include image analysis in some form. In a previous chapter an SVM was used to classify EBM thermal images to automate camera acquisitions. This section expands on that to employ ML as an analysis technique, that could be integrated as a part of a feedback mechanism into robotic welding. The setup used in this work was the same as in the previous section, with the focus on 'end on' thermal images from the pipe welding GTAW setup. These images were captured with a view to analysing the weld pool at high speeds.

The machine learning technique used before, an SVM, is a technique used to classify data as a whole into categories, applied to images. A different technique will be used here that can be applied in more versatile ways. Neural networks and deep learning have become increasingly common techniques in ML recently due to advances in availability of computing power and in turn algorithm development. A neural network based pixel level classification system was designed and tested for image segmentation on pipe welding

images. This would allow analysis on specific image areas or the size and shape of identified areas of interest in an image.

This technique was chosen because of the difficulty in getting successful image segmentation with traditional image processing methods. Traditional methods were successful previously in this chapter because of the limited areas they worked on and the limited amount of information that was trying to be extracted using the process, e.g. location of a single blob. When the whole image is considered there are too many areas with similar features that belong to different segments of the image. This was found not only with the welding images, but also when trying to segment the images captured from the EBM system. In both cases very subtle changes in brightness on an image, both spatially and temporally, can indicate a feature. This then makes algorithm development more difficult because making the processing methods sensitive enough to detect these changes also makes them very noisy. Trying to differentiate between the noise and the features is then hard because the features are out of context and they all fit the same rule used to detect initially.

The challenges of designing a ML based image processing system are very different to those of designing a traditional image processing pipeline. In an ML based system, especially a NN, the individual processing steps are almost invisible to both the user and designer. Rather than designing each individual image processing operation when using a NN the inputs, outputs and structure of the network are defined. The structure of the network is the main design problem; the single layer size and depth of the network need to be selected and tuned for the task. After the network has been designed it is trained and evaluated on a large dataset, during this process the algorithm optimises the weightings of the network nodes. This is the process that ultimately defines the processing steps that are used within the network.

#### **5.4.1 First Neural Network Design**

The types of networks that can be used for tasks are often defined by the input data and the amount of data available. Here a relatively shallow 13 layer network was designed first, consisting of 11 internal layers, an image input layer and a pixel classification output layer. Figure 5.17 shows the layer diagram. The internal layers of the network are configured to downsample in the first half of the network then upsample the outputs of those layers in the second half to match the output size. This has the overall effect of getting the network to focus on larger features in the image; which should be more generic to the dataset as a whole rather than the specific training images.

The downsampling layers in the first half of the network are made up of 2 groups of 3 layers with each group consisting up of a 2D fully convolutional layer, a ReLU layer and a max pooling layer. The 2D fully convolutional layer was the layer that contains the image

processing steps. These layers were configured with 64 3x3 filters, or kernels, a stride of 1 in both x and y directions and padding of 1 pixel on all edges. These settings make the layer fully convolutional by creating the same sized output as the input in the x and y dimension. Each kernel is convolved with the input to create an ‘activation image’ containing the output from the convolution, therefore the output from this layer will be the same size and the input in the x and y dimension but will contain 64 images in the z dimension.

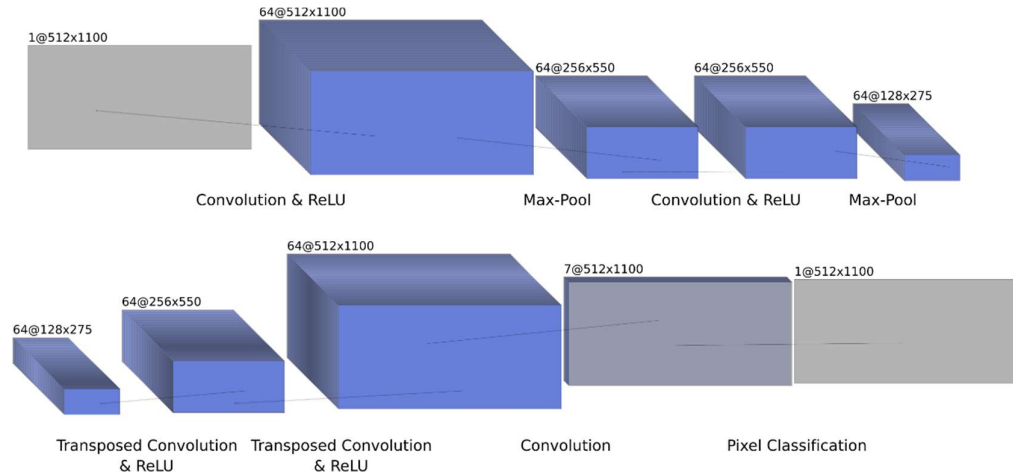


**Figure 5.17 Network layer diagram of first design, showing layer transform types and sizes after each layer. 1<sup>st</sup> line is downsampling layers, 2<sup>nd</sup> upsampling layers, (central layer (64@128x275) repeated for clarity) [11]**

The next layer, a Rectified Linear Unit (ReLU), is an activation function layer. There are multiple different types of activation functions but the purpose of all of them is to add non-linearity to the network. Non-linearity is what differentiates neural networks from other ML techniques like SVMs[12]. Non neural network style ML algorithms fit and solve a linear regression problem to map from input to output, whereas a neural networks fit and solution is non-linear; this is what allows their application on more complex problems. The ReLU function is designed to more closely resemble biological neurons, whilst keeping the ease of linear gradient optimisation in the network [13]. This is because the ReLU function (Figure 5.18) has a nonlinear effect but is a piecewise linear function, with 2 parts meeting at 0, meaning its evaluation is very fast.

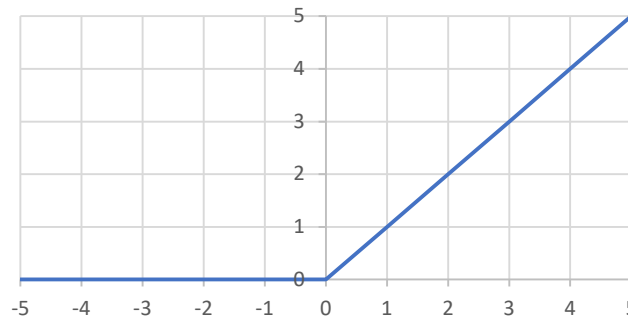


**Figure 5.18 ReLU function example, for all input values < 0 (X axis) 0 is output and for value > 0 the input value is returned**

The next layer, a max pooling layer, was a layer designed to modify the output of the previous 2 layers by summarising an area of the output in a specific way. The max pooling layer was the layer in this set of 3 that does the down sampling, it was configured here with a 2x2 size and a stride of 2 in both directions. This means that the output from this layer will be half the size in both width and height of the input. Each value on the output will be the maximum of the 2x2 area it represents on the input. Pooling layers are included in a network to select features from previous layers and make the network more robust to small changes in the input, in terms of the input values and the locations of those values. For example max pooling layers have shown to be good for image recognition tasks and similar because they will remove noise from the network and preserve the relative locations of features [14].

These layers are repeated twice to make the downsampling portion of the network. In the centre of the network the size of the output is a quarter that of the input, in x and y, and 64 in z as a result of the convolutional layers with 64 filters each. This means with an input image size of 1100x512x1 the size after the downsampling layers will be 275x128x64. By this point in the network there should be a representation of larger features within the image created by the filters in the convolutional layers.

The second half of the network uses this distilled information about the input image to make the 'decision' on the classification of each pixel. This is done in two stages; first the output from the first half of the network is upsampled to match the input size, then the classification is made. The first stage is, like the downsampling, completed with 2 groups of 2 layers; a transposed convolutional layer, then a ReLU layer. In the second stage the pixel classification was handled by 3 layers, a convolutional layer, a softmax layer and a pixel classification layer.

The upsampling stage here was essentially the same as scaling an image, the transposed convolutional layers perform the inverse of the convolution that occurred in the first half of the network. This can be called a deconvolution, and in certain network designs these layers are deconvolutional layers, however the difference is that deconvolution does not perform any interpolation. A deconvolution will convolve its input and pad with a fixed value, normally 0, this has the effect of spreading the input data out according to the size of the kernel. This means there is a one-to-one relationship between the input and output, whereas to truly perform the inverse of a convolution there should be a one-to-many relationship.

The transposed convolutional layers here were configured with 64 kernels, a kernel size of 4x4, a stride of 2 in both directions and will crop the output by 1 pixel along all edges. These parameters have the effect of, over 2 iterations, upsampling to the original image input size so the classification layers can classify every pixel. As mentioned above the

transposed deconvolutional layers interpolate the input data to create an output value at every location. The interpolation here was the learned element; rather than being set to a predefined interpolation method, like bi-cubic or linear, the values of the 4x4 kernels are optimised in training. This was why the ReLU layer after the transposed convolutional layers was introduced, it again adds non-linearity to the network.

The first layer of the classification stage was another convolutional layer, configured with 7 kernels, a kernel size of 1x1 and a stride of 1 in both directions. The purpose of this layer was to condense the 64 output activation images from the previous images into 7 that will represent each possible classification. After this layer the 7 activation images contain the activations of the network for each pixel for each of the 7 classes. At this point they are raw outputs from the previous convolutions, the next layer, a softmax layer, transforms this raw output into weightings for each class. This will be represented in the form of a probability across all 7 classes. The softmax layer is an extension of logistic regression and allows the network to work with more than 2 classes.

The final layer in the network was a pixel classification layer and uses the probability output from the softmax layer to output a class for each pixel. This layer can also take into account class weightings, these will weight the probabilities from the softmax layer before choosing an output class. The purpose of weighting the classes is to try and remove bias from the training dataset. Ideally the training data would contain the exact same number of samples for each category; however, this is not practical, especially for a pixel level classification working on real world images. To fulfil this requirement each image would need to be crafted with perfectly segmented regions and no noise. Here the class weightings were set to the inverse of their number of appearances in the training dataset. This should mean that each class is represented equally to the network. The MATLAB code for creating, training and evaluating the networks is listed in appendix 7.4.

#### **5.4.2 First Network Training & Results**

With the design of the network completed, the next step was to train the network. This was the process of optimising the weightings of the network nodes; in relation to the layers described above this means optimising the values of the convolution kernels. This is done using back propagation, a process where the output of the network is compared against the correct category and the difference used to correct each layer in turn. The goal here is to reduce the difference in the output verses the ground truth for that input to 0, this difference is termed the 'loss' of the network. A loss of 0 means the network predicted every pixel correctly across the whole dataset. This is the optimisation problem the network is designed to solve and generally uses a form of gradient decent to do so. In this case a SGDM (stochastic gradient descent with momentum) solver was used.

For a training dataset 100 sample images from a welding run were annotated with labels for every pixel. These were picked to represent all states of the weld during a run, from before any filler was melted onto the pipe, through to a completed revolution. These were manually annotated for the 7 categories using MATLABs Image Labeller application. The categories chosen for segmentation were; torch, filler, molten filler, weld pool, solidified weld, torch glare and background. These were numbered from 1 to 7 to be represented as pixel values in ground truth images (examples Figure 5.19). These categories were selected to represent all potential areas of interest in the welding images, with particular interest in the weld pool and solidified weld categories. Statistics on these areas of the image can inform a lot about the current state of the weld and if they can be segmented well by the network, this could be a valuable analysis tool.

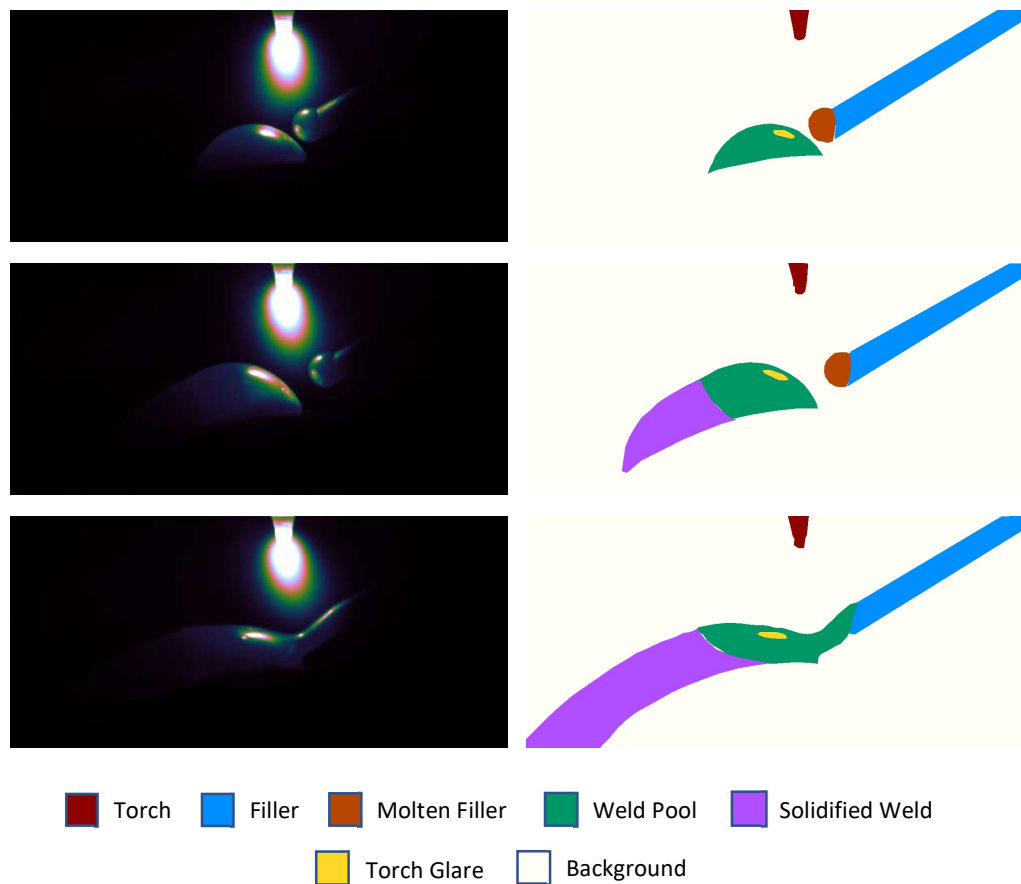


**Figure 5.19 Example training images and corresponding ground truth images with labeled areas coloured**

Training was completed with the 100 image training dataset for approximately 6000 iterations; using MATLABs multi CPU parallel trainer over approximately 36 hours. The training dataset was small here for a machine learning dataset problem, but this was the best practical dataset size achievable. The size of the dataset will affect the training of the algorithm and could cause it to over train because the dataset was not varied enough.

Strategies to mitigate this will be explored in later iterations. During the training the trainer was set to save its progress every epoch (3 iterations). In Figure 5.20 below the global accuracy of the network at each epoch can be seen. Training was interrupted at epoch 800 and restarted, that was what caused the large drop in accuracy.

The drop-in accuracy at the start can be explained by the random initialisation of the network node values. This was the training algorithm starting to change the values and because of the nature of the optimisation it will not always head in the correct direction to start with before it finds a positive gradient. After 1949 epochs the global accuracy was approximately 0.335, training was stopped here because the accuracy of the network had flattened out and it was apparent it was not going to improve.

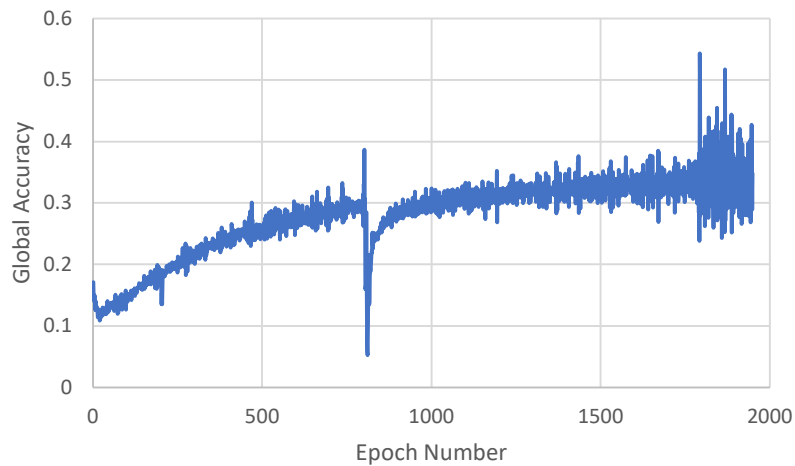


Figure 5.20 Global accuracy of the first network design over the whole training period

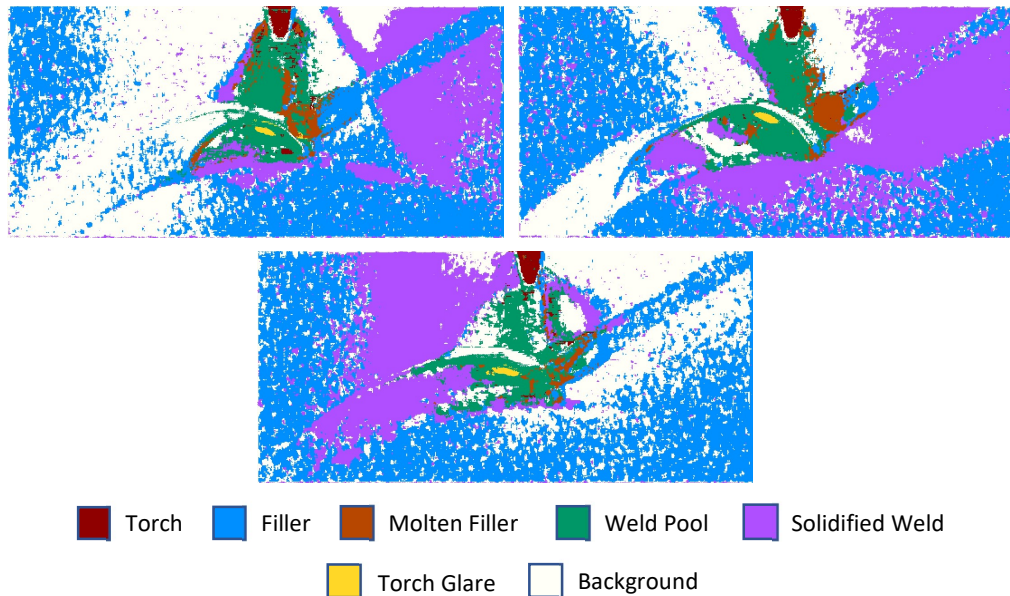


Figure 5.21 Example segmentation images from first neural network iteration. Corresponding 3 images from Figure 5.19

When evaluating the images segmented with the final network iteration there was a lot of confusion between certain categories of pixels. Especially with pixels being classified as background when they should not be. The network was likely detecting small changes in the background intensities from reflections or other artefacts between the images and using them as features for that category. This was what was expected, but the problem lies in the weighting of the categories. The background features are weighted as highly as all the foreground features to the algorithm, therefore when outputs from the network are very similar for each category pixel was just as likely to be classified as background as any other. In an ideal sense this is correct, but with a network that was not going to predict all pixel classifications perfectly it would be better to bias the network away from the background class. This would put more emphasis on it correctly predicting the other foreground classes that are of more interest.

Another reason for this could be the shallow nature of the network. It may be identifying strong features from each class but might not be able to properly relate them to each other and their location in the full image. The shallowness of the network would cause this because at its smallest the input image is described by a  $275 \times 128 \times 64$  tensor. Which is a large number of data points when only using a  $3 \times 3$  kernel. At this level 1 node in the tensor only contains information from a  $5 \times 5$  area in the original image.

### **5.4.3 Second Network Design**

To address the problems seen with the first iteration of the network the layers and kernel sizes were adjusted for the second iteration. In the down sampling layers the convolution kernel size was increased to  $5 \times 5$  and the number of kernels reduced to 50. This was an effort to increase the field-of-view of each node at the centre of the network had of the input image; and also try to focus more on the larger features within the image. The number of down sampling layer sets was also increased from 2 to 3, which further increased the effective area the centre nodes have 'seen' of the original image.

The stride of the convolution was kept at 1 in both directions but the padding around the edge of the image needed to be increased to fit the kernel size and stride to the to the input image size. The input image was padded with 2 rows along the top and bottom and 4 columns along the left and right. These extra pixels were set to 0's which will cause some distortion in the segmentation around the edges of the image. This is because at the edges of the image the padded areas will influence the convolution of the pixels up to 2 rows/columns into the real image. This was acceptable for this application as the main areas of interest will not lie close to the edges of the image. The max pool and ReLU layers remained the same.

The upsampling half of the network remained largely the same from the first iteration. The number of kernels was changed to 50 to match the down sampling layers. The cropping

needed to change to 1 row top and bottom and 3 columns left and right to account for the padding added by the down sampling layers. The stride remained at 2 in both directions and the kernel size at 4x4.

The final classification layers remained the same apart from the class weightings on the pixel classification layer. Here the weightings were biased away from the background class, this was to discourage the network from predicting pixels as background because it was the biggest class when it was unsure. The rest of the class weights were still based on the frequency of their occurrence in the input dataset. The completed network diagram can be seen in Figure 5.22.

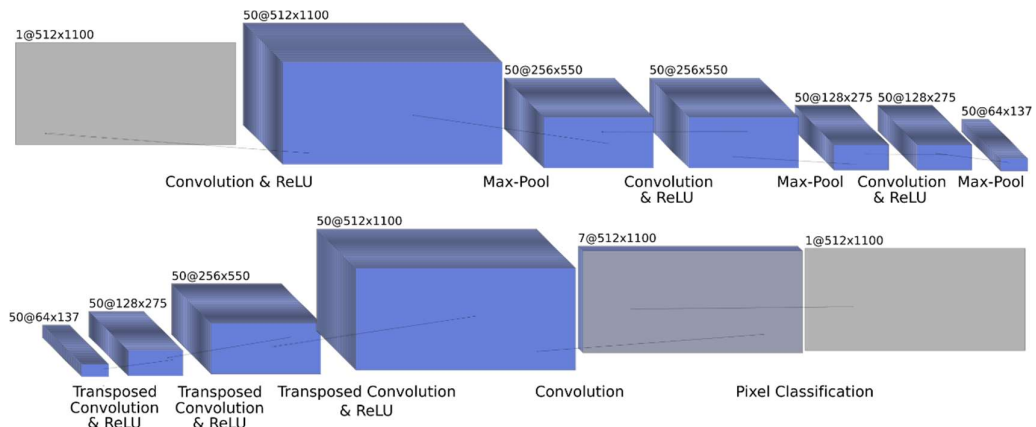


**Figure 5.22 Network layer diagram of second design, showing layer transform types and sizes after each layer. 1<sup>st</sup> line is downsampling layers, 2<sup>nd</sup> upsampling layers (central layer (50@64x137) repeated for clarity) [11]**

#### 5.4.4 Second Network Training & Results

The training strategy for this iteration was changed compared to the first network. With the first network the learning rate was constant. But for this iteration it was started high and decreased over time. The aim of this was to mimic the human learning process, the big picture of the subject can be learnt quickly and easily to start with, resulting in large jumps in knowledge. The finer points are then learnt more slowly because they require a deeper understanding. This is what changing the learning rate for the network does. The learning rate sets the size of the steps in the optimisation stage; the larger the step size the more likely the algorithm is to get close to the best solution, rather than getting stuck at a local minimum. Decreasing the learning rate then allows the algorithm to home in on the optimum solution.

This process was also assisted by starting with a reduced dataset and increasing its size. 30 images were chosen for the first stage of training, making sure to include images from varying points in the process. In this first stage a small set of validation images were also used. This was a set of 7 images that the network was tested against every 50 training iterations, these were separate from the images it was trained on. This was useful to

monitor progress on the limited dataset because the point of training the network this way was that its accuracy will increase quickly, but that was only on the training dataset. Validation gave insight as to whether that accuracy score will be applicable to the full dataset.

After 600 training iterations with the first training dataset as described above the network was evaluated against the full 100 image training dataset. At this point a global accuracy of 0.778 was achieved, this shows the training strategy was working.

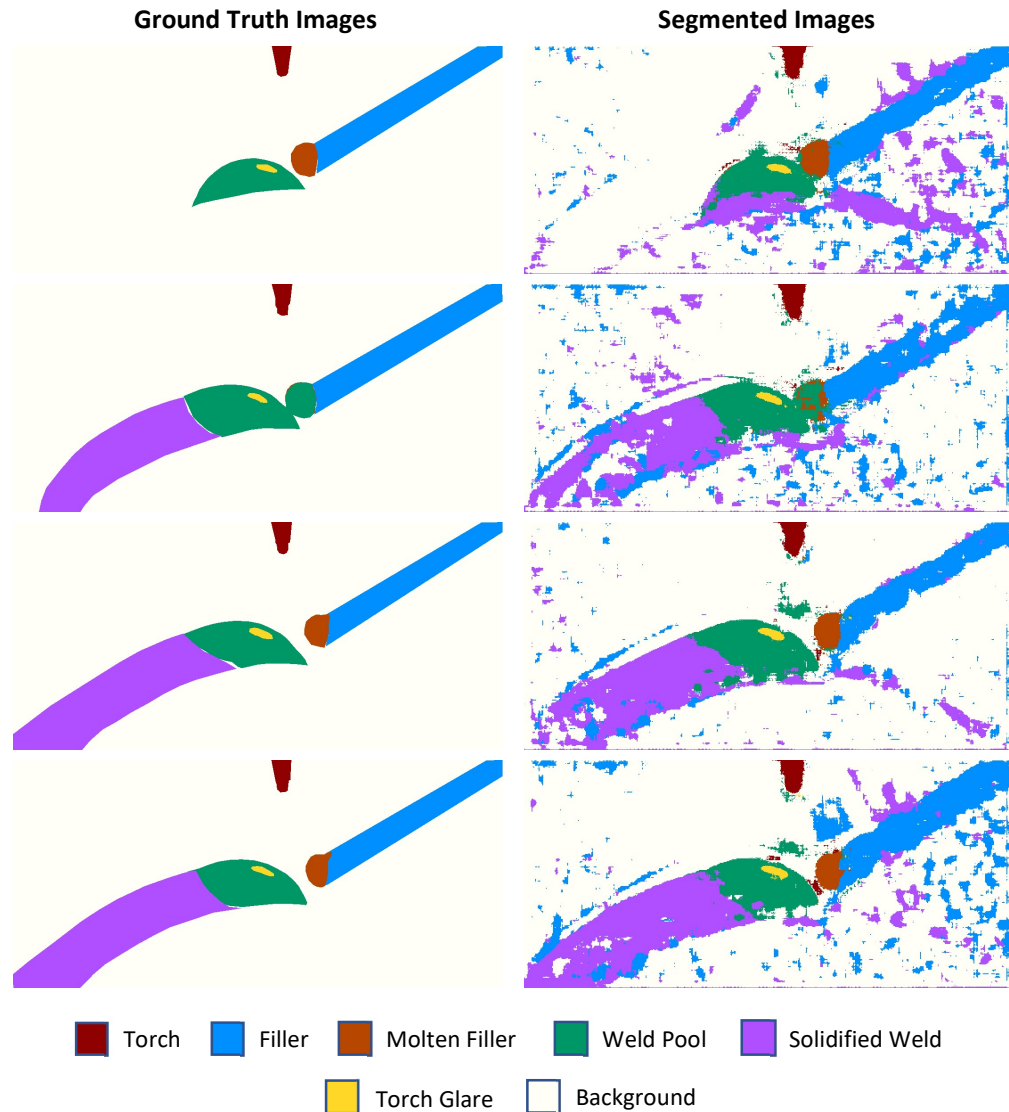


**Figure 5.23 Example of second neural network output. Showing ground truth and output images**

The training was continued for another 1000 iterations before increasing the dataset size to 50 images and removing the validation set. After 1500 iterations training with 50 images, the full dataset was included, and the learning rate reduced to a constant 0.0001. The final version of this network had been trained for 9000 iterations and reach a global

accuracy of 0.83 and mean accuracy of 0.927 when evaluated against the full dataset. This included 40 new images that the network had never seen before. Mean accuracy takes into account the accuracy of individual image classes whereas the global accuracy is the ratio of correctly predicted pixels to incorrectly predicted pixels, regardless of class. This resulted in images like shown in Figure 5.23.

A third iteration of the network was designed to take advantages of what was learnt in designing and training the first 2. The network structure stayed the same as the second network with 3 downsample and upsample layer sets, however the number of convolution kernels was increased to 64. This should allow the network to increase the complexity of the segmentation versus the second network and the training methodology from the second network has been proven for this dataset and was used again.

When trained the third network design only achieved a global accuracy of 0.745 and a mean accuracy of 0.493. This was significantly lower than the previous network and shows that the training method used matched well to the number of kernels used in the second iteration and the dataset size. It was likely that the dataset size was too small to properly train more kernels than used in the previous iteration. A dataset size of 100 images was also very small for a neural network.

#### **5.4.5 Neural Network Segmentation Evaluation**

When evaluating the results of the segmentation of the second network the real challenges of the problem become apparent. When comparing the sections that were correctly segmented versus the raw data of those areas the input data looks very similar locally even though they are being expressed as raw 16-bit images. This means that small kernels and a low number of layers as used in this design will struggle to identify larger segments; especially those that are not very well differentiated from the surrounding segments. The third network design was an effort to account for this but as mentioned above it is likely the case that the input training dataset was also starting to limit the potential at this size.

Shown in Figure 5.24 is an image segmented with the best iteration of the second network along with the corresponding ground truth and input image. The background of this image demonstrates the problem with small kernels, the small areas identified as solidified material towards the top left of the image are the jaw of the chuck passing though the image. The edges of the jaw are creating features in the image that are illuminated by the reflections from torch arc and weld pool. These are incorrectly identified as solidified material because on the scale of the view area of a single pixel has at the network centre (7x7 pixels of the original image) they fit the model it has learnt for that class. However, if this area was much larger it would be evident that it was only a small area that properly satisfies the characteristics of the class and not the large area that the network was trained

on and really identifies solid material. This kind of problem is one of the reasons for the increase in use of deep neural networks, for example Noh et.al [15] uses 13 convolutional layers for segmentation.

The areas in the images there are segmented correctly are very close to the ground truths the network was trained with in terms of size, shape and locations of the segments. This was the case for images from the original training dataset as well as images not included in training. This shows that this solution is capable of the goal of segmentation of images to detect the weld pool and other features in end on pipe welding thermal images. With more training data and time this technique could be refined and applied to a real time camera input to enable intelligent measurements of weld pool size for example. This could then lead to extra measurements enabled by thermal imaging such as those shown as part of a manual process in earlier sections or examples like weld pool temperature and the cooling rate of the solidification process.

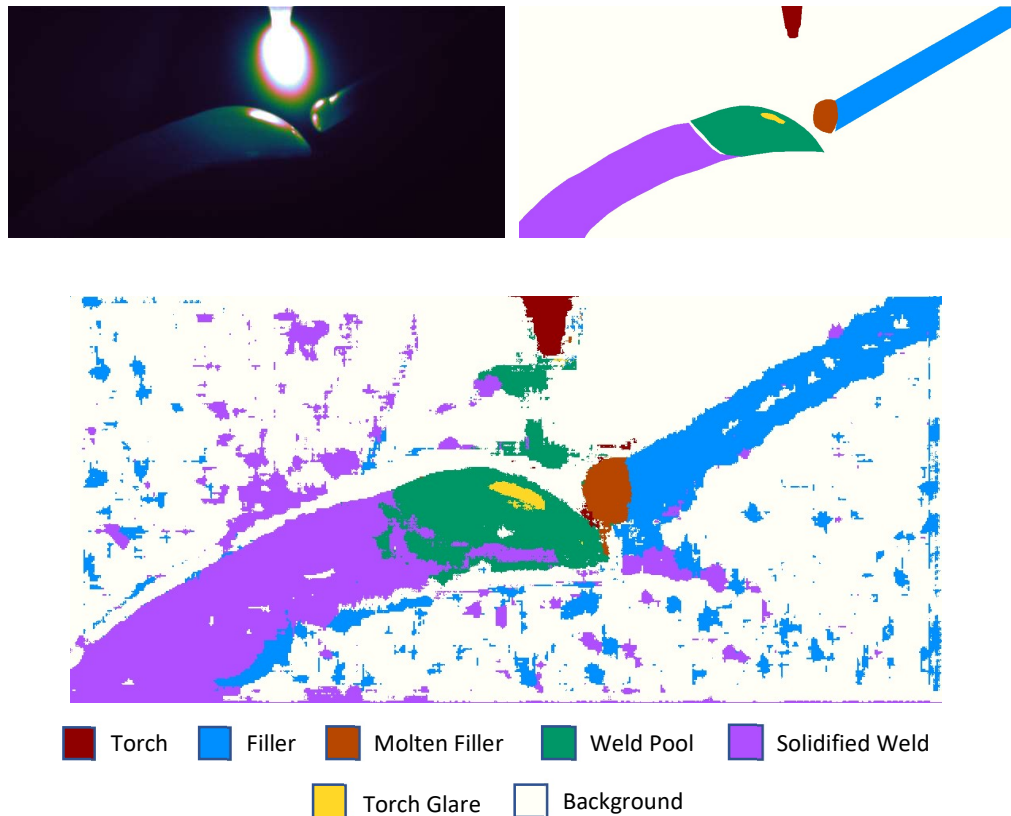


Figure 5.24 Example output from neural network, showing input, ground truth and output

## 5.5 Conclusion

This chapter has shown the application of the system and knowledge developed in the previous two chapters to gas tungsten arc welding. Analysis techniques based on thermal images of turbine blade welding and pipe welding were developed; based on freezing point detection and slag tracking in the weld pool. Both techniques could be further

developed into weld quality indicators with the view to them being used as such in real-time feedback systems for robotic welding. Use of thermal imaging in robotic welding applications has not been widely demonstrated, especially in this application. The freezing point analysis is something that could leverage existing research on weld dynamics to provide insight that previously may have only been possible with destructive analysis. A neural network was also developed for image segmentation of the pipe welding thermal images. While at this stage the network does not produce perfect results this level of segmentation has not been applied in this context before. However, the network can detect important parts of the thermal image and could be used for rough size measurement as well as informing other analysis techniques which sections of an image should be used for their analysis.

- [1] R. French and H. Marin-Reyes, "High value intelligent aerospace turbofan jet engine blade re-manufacturing system," in *Advances in Intelligent Systems and Computing*, 2016, vol. 490, pp. 241–252.
- [2] R. French, W. Yeadon, G. Kapellmann, and H. Marin-Reyes, "Development of a Vision System for TIG Welding - A Work-in-Progress Study," in *2018 IEEE 23rd International Conference on Emerging Technologies and Factory Automation (ETFA)*, 2018, pp. 1193–1196.
- [3] Edmund Optics, "Anti-Reflection (AR) Coatings," *Laser Optics Resource Guide*. [Online]. Available: <https://www.edmundoptics.eu/resources/application-notes/optics/anti-reflection-coatings/>. [Accessed: 30-Apr-2019].
- [4] H. Preston-Thomas, "Temperature Scale of 1990 The International Temperature Scale of 1990 ( ITS-90 )," vol. 27, pp. 3–10, 1990.
- [5] A. C. Davies, *The science and practice of welding*, 8th ed. Cambridge University Press, 1984.
- [6] B. Deo and R. Boom, *Fundamentals of steelmaking metallurgy*. Prentice Hall International, 1993.
- [7] P. S. Wei, C. Y. Chang, and C. T. Chen, "Surface Ripple in Electron-Beam Welding Solidification," *J. Heat Transfer*, vol. 118, no. 4, p. 960, 1996.
- [8] J. Hu, H. Guo, and H. L. Tsai, "Weld pool dynamics and the formation of ripples in 3D gas metal arc welding," *Int. J. Heat Mass Transf.*, vol. 51, no. 9–10, pp. 2537–2552, May 2008.
- [9] J. Rau, "The Effect of Trace Elements on the Formation of Slag Spots During Gas Tungsten Arc Welding of 316L Stainless Steel Tube Systems," in *Presentation at SEMI Stainless Steel Task Force Meeting*, 2003.
- [10] X. Kong, O. Asserin, S. Gounand, P. Gilles, J. M. Bergheau, and M. Medale, "3D finite element simulation of TIG weld pool," *IOP Conf. Ser. Mater. Sci. Eng.*, vol. 33, no. 1, p. 012025, Jul. 2012.
- [11] A. Nail, "NN SVG." [Online]. Available: <http://alexlenail.me/NN-SVG/LeNet.html>. [Accessed: 12-Nov-2019].
- [12] I. Goodfellow, Y. Bengio, and A. Courville, "Learning Algorithms," in *Deep Learning*, Cambridge, Massachusetts: The MIT Press, 2016, p. 775.
- [13] X. Glorot, A. Bordes, and Y. Bengio, "Deep Sparse Rectifier Neural Networks Xavier," *Proc. 14th Int. Conf. Artif. Intell. Statistics*, no. 15, pp. 315–323, 2011.
- [14] D. Scherer, A. Müller, and S. Behnke, "Evaluation of pooling operations in convolutional architectures for object recognition," in *Lecture Notes in Computer Science (including subseries Lecture Notes in Artificial Intelligence and Lecture Notes in Bioinformatics)*, 2010, vol. 6354 LNCS, no. PART 3, pp. 92–101.
- [15] H. Noh, S. Hong, and B. Han, "Learning deconvolution network for semantic segmentation," in *Proceedings of the IEEE International Conference on Computer Vision*, 2015, vol. 2015 Inter, pp. 1520–1528.

## 6 Conclusion and Further Work

### 6.1 Summary of Work

This work has introduced and developed a thermal imaging system for use in monitoring additive manufacturing processes. Specifically, it has demonstrated the use of silicon sCMOS detectors in electron beam melting and gas tungsten arc welding. Silicon sensors are a lesser used technology in the area of thermal imaging, and it has been shown that AM is a very good application for them. The high temperature nature of metal AM processes allows sCMOS to be used to begin with and the other traits of AM, such as high speed, high cooling rates and small feature size mean the sCMOS sensors can really be taken advantage of.

Chapter 3 began by showing the design and calibration process for the imaging system. The design aim was to create a system specifically for AM monitoring and the combination of an sCMOS camera and the custom designed lens system fulfilled this. The calibration followed the process of single point infrared thermometer calibration as a guide which allowed radiance temperatures to be monitored. The whole imaging system was designed to require no modification to the essential parts of the Arcam S12 EBM machine and minimal modifications overall. With the system in place and using the film feed system to keep the window free of metallisation, it was shown that the system could monitor the AM process without interruption. With a variable exposure time and multiple calibrations, the temperature range of interest could be set from a range that focused on the low range cooling effects and powder bed, up to high contrast imaging of the molten material in the melt pool. The chapter finished by showing the potential of the system to begin to detect problem areas and defects within AM builds.

Chapter 4 looked at linking what is seen in thermal images to materials properties and what is possible with analysis of real time images from the system. Cooling rates were used as a predictor for material grain structure. This is already established knowledge but, using thermal images from layers at different heights of the build the observed cooling rates were able to be correlated with the materials structure and properties of that location. This was done by post processing analysis, but it shows that this system can be used to predict these properties without destructive testing of parts. The melt pool size within a build was also investigated and its relationship to part porosity, initial results showed that where smaller melt pools were seen porosity increased.

An emissivity tracking system was built to provide tracking of melted parts of a build and allow the application of different processing or calibration dependant on location. Tracking the melted sections of a layer allowed different emissivities to be applied given the likely surface finish and composition of that area. This allows more accurate emissivity correction and therefore more accurate temperatures from the thermal images. This

system was initially designed only for this purpose but also proved a useful tool for extra visualisation and analysis of builds by allowing the melted areas to be automatically extracted from images.

To increase automation and effectiveness of the system, in terms of data collection, an effort was made into integrate the image capture process with the Arcam. Due to lack of access to the machines control system and unpredictable sensors triggering captures on layer start was not reliable. To provide another solution machine learning was used to create a system to trigger the capture based on the real time analysis of the thermal images. This system was able to detect and trigger a capture within 200 frames of the layer start and was able to stop the capture at the end of a layer. This fully automated the capture process and reduced the number of empty frames captured.

Finally, this chapter looked at electron beam welding of dissimilar metals. With the use of the thermal imaging system on the Arcam the weld pool temperature could be analysed in situ. This allowed an area of heating in front of the weld pool to be identified. The preheating effect was identified as one of the main factors for the dissimilar weld being possible in this process. Without the thermal imaging system this kind of analysis would not have been possible.

Chapter 5 showed this technology in a different AM context, Gas Tungsten Arc Welding. Applying the same sCMOS camera as previous chapters with off the shelf optics allowed high speed imaging of the GTAW welding process and weld pool. The setup was recalibrated for the application to focus primarily on the high temperature weld pool. An analysis technique for detecting the freezing point of the weld was created based on the detection of the freezing plateau in the cooling weld bead. The high spatial resolution of the system was used here to give a high-resolution view of the cooling of the weld. With this analysis potential defect locations were able to be detected based on the frequency of the movement of the freezing point along the weld bead. Finally, machine learning was used to detect features in the welding images. A network was designed and trained to perform a pixel wise segmentation of the images, aiming to identify 7 different classes within each image. The network was able to detect position size and shape of the weld pool and other features in an image.

The combination of sCMOS hardware and the types of analysis shown here are a good match for AM applications and start to show the potential for this kind of system. As discussed in the first chapter a motivation for this kind of system is the lack of knowledge and trust in AM processes, compared to traditional manufacturing processes. With this kind of thermal imaging system analysis can take place during a build and in areas that would not have been possible with other techniques, or without destructive testing. This

can then lead to a better understanding of AM processes and how to best take advantages of them to create parts accurately and with the desired properties.

## 6.2 Conclusions

The main conclusion from this work has been that silicon sCMOS imaging technologies are suitable for use as thermal imagers in high temperature applications such as additive manufacturing. Currently this technology is sparsely used in the field of thermal imaging and this is its first use in AM. The advantages of using silicon have been shown and how they benefit the application of AM monitoring. Besides the greater speed and resolution that silicon sensors bring their wider availability and specification diversity is an advantage if they are to be used in the future on commercial monitoring products for example.

Although currently standardised methods for calibration do not exist, they are being worked on by others in the field. However, this work has shown that using the calibration method from a single point device can produce representative temperature images, even if it doesn't account for all the effects that will be present on an image sensor compared to a single detector. Specific to the analysis methods applied to AM here it was also evident that relative temperatures are still of interest. They can still be used to draw useful conclusions around the links between the thermal conditions during a build and materials properties.

The demonstration of the emissivity tracking system is the first attempt to provide dynamic emissivity correction in an AM monitoring system. Emissivity is known to often be the biggest source of error in any IR temperature measurement system. This process will reduce that error by accounting for the emissivity change from the powder to solid material change. This will be further improved by better understanding of the emissivity changes of materials in AM. This kind of emissivity correction will be required for any thermal imaging system used in AM that hopes to provide anything more than radiance temperatures.

The monitoring system as a whole has provided insights in the EBM process that would not have been possible without it. The links between materials properties and the thermal characteristics of a part could have been inferred based on knowledge of the materials. However, in situ monitoring throughout a build allows the important temperature transitions to be pinpointed and conclusions drawn about whole parts without destructive testing. The potential for using systems similar to this in the future for part verification is huge and could be something that allows the widespread adoption of metal AM.

The use of thermal imaging as a non-destructive testing and observation method for welding is also something that could be a valuable tool in this field. When conducting this research one of the researchers working on the welding setup commented how much more useful a real time temperature view of the weld was, opposed to a view through a

welding visor. The automated detection of defects based on analysis like that presented with the freezing point analysis could remove steps from the post weld processing. It could also allow parts to be tested that previously could not because of prohibitive cost or other complications. In both cases and with the EBM work machine learning elements could augment existing analysis and provide new analysis opportunities.

### **6.3 Further Work**

This work has shown the initial development of a silicon sCMOS based thermal imaging system for AM. There are areas of the system itself and the analysis built on top of it that can be further developed to produce more accurate temperatures, tighter integration and more instantly relevant outputs.

Emissivity is an issue with all infrared measurement techniques and has started to be addressed with the emissivity tracking system shown in this work. However, this system only currently considers 2 possible states of the material in a given area, melted or not melted. This could be extended with more potential states taken into account; molten material and different levels of sinter for example. This would require more processing techniques to detect these states in the image, or potentially this could be another application for a ML model like shown in chapter 4. This would also require more in-depth studies of the emissivity of the alloys used in the process; current literature does not give an appropriate set of emissivities or emissivity model for these alloys in the various states they are found within the EBM process. If an emissivity model for the process can be created there is a big improvement in measurement accuracy and uncertainty to be made.

One of the challenges in creating and applying an emissivity model will be the temperature dependence of the emissivity of the Ti-6AL-4V alloy commonly used in EBM and other AM processes. With the emissivity changing not only with surface finish and material state but also its temperature an emissivity independent temperature measurement would be required to fully apply an emissivity model like this. An independent measurement would be very hard to create with a contactless method, and if it was done with high resolution could replace the CMOS measurement system itself. Another, more practical, way to achieving this could be to use a model of the process and part being built to predict temperatures at a given point and time within a build, this could then be used to inform the emissivity model and provide a correction.

The discrete state detection and correction via machine learning may be a more practical and achievable solution with the current state of the technology and modelling. If this were to be undertaken a large set of images with areas of known qualities would need to be created and labelled accordingly. The sample would need to be much larger than the 100 images used in chapter 5, because, as discussed in that section, the neural network

already appeared to be hitting the limits of the training dataset. This method would also be subject to the uncertainties caused by temperature dependant emissivity.

Integration of the imaging system into the process would also be an area for further work in both the EBM and GTAW setups. One of the aims of this work was to create a system that could be used as a sensor input for a process control system, however this was not achieved. Further integration with the Arcam EBM system is possible, starting with and building on the automated capture system shown in chapter 4. Being a propriety system the Arcam software may be difficult to interface with for control over the process, however other systems allow for programmable access to the control system and parameters. Any techniques developed with the system on the EBM setup could be transferred onto machines with this capability.

On the GTAW setup the opportunities to hook into the control system are much greater with the systems being bespoke for the application. Here high magnification imaging of the weld pool, electrode and surrounding area could be used to feedback data to the control system. This may take the form of information about the weld pool size and temperature, the effect gas flow is having on the melt pool and the effect the weld is having on the surrounding material. This last point will be of interest when welding materials at risk of microstructural changes because of high temperature changes local to the weld. Minimising the amount of heat build-up in these parts is crucial to providing a good weld that does not affect the structural integrity of the part as whole. Control algorithms are already used to minimise this effect, but with the addition of real time feedback of the temperature and size of the heat affected zone around the weld improvements could be made.

One issue that effects all imaging systems and becomes important when they are relied on for measurement is the quality of the optical system. A real-world optical system cannot perfectly represent the scene it is viewing, any given system will have a transfer function that describes how it transforms the image. A full transfer function will consider any aberrations and the size of the measurement field of view (MFOV) for a given pixel. This will take the form of a point spread function (PSF), which could be different for each pixel of an array and describes how the optical system distributes the energy received from a MFOV. This means that not all the energy received from a given area of the scene will be received by its corresponding pixel on the imager array; therefore, in the case of a thermal imaging system objects will appear cooler than they should. Creating this PSF for every pixel is not trivial but would be needed to fully correct for the optical system in an imager. Corrections for this would further decrease the measurement uncertainty for an imaging system and would be particularly useful in AM monitoring because of the small size of interesting features in an image.

## 7 Appendices

### 7.1 Emissivity Tracking Code

Below is a listing of the `melpoolTrack` MATLAB function which implements the emissivity tracking and is used as a part of a larger image processing workflow in MATLAB.

```
function [meltedMask, emissivityImage, correctedImage] =
melpoolTrack(mask, image, in)

    thresholdImage = imbinarize(image, (in.threshold / 65536));

    [~,centroids, ~, major, minor, orientation] =
in.hblob(thresholdImage);

    if ~isempty(centroids)
        [m, ~] = size(centroids);
        for blobNo = 1:m
            mask = ellipseMatrix(centroids(blobNo,2), ...
                centroids(blobNo, 1), major(blobNo)/2, minor(blobNo)/2, ...
                orientation(blobNo), mask, 1, 0, 0);
        end
    end

    se = strel('disk', in.melpoolDiameter);
    mask = imclose(mask, se);

    emissivityImage = ones(size(image));
    emissivityImage(mask) = in.emissivityMelted;
    emissivityImage(~mask) = in.emissivityUnmelted;

    correctedImage = double(image) ./ emissivityImage;

    meltedMask = mask;
end
```

This function is called in the large image processing loop that increments through a set of images to be processed. The input parameter `mask` contains the emissivity mask which is the previous output of the function if it has been run, or a matrix the same size as the input image containing all zeros. The image input parameter contains the current raw image being processed. The `in` parameter contains the input setting for the image processing code. The function returns `meltedMask` - a binary mask of melted areas on that layer, `emissivityImage` - an image containing an emissivity value for each pixel in the image and the corrected and `correctedImage` - the emissivity mask applied to the input image. The blob detector `in.hblob` is setup using the below code outside the function.

```
in.hblob = vision.BlobAnalysis(...
    'CentroidOutputPort', true, 'BoundingBoxOutputPort',
    true, ...                               'MajorAxisLengthOutputPort',
    true, ...                               'MinorAxisLengthOutputPort', true,
    'OrientationOutputPort', ... true, 'MinimumBlobArea',
    in.melpoolArea, 'MaximumCount', 10);
```

## 7.2 Freezing Point Detection Code

Below is a listing of the MATLAB script used to implement the freezing point detection algorithm, the parameters for the run shown in this work are defined at the top of the script.

```
clear;
imgFolder = 'imagePathRemoved';
imgRange = 930:3860;
row = 140:380;
col = 90:600;
lineAvgSize = 10;
tempIncrement = 5;
minTemp = 1440;
maxTemp = 1590;
smoothingHeight = 2;
smoothingWidth = 5;
colourMin = 1300;
colourMax = 2200;

video = 0;
videoPath = [pwd '\\'];
videoName = 'Freezing Point Video Thresh With Peaks Full';
framerate = 10;
figureSize = [0, 0, 1920, 1080];

colourMap = cubehelix(colourMax - colourMin,0.5,-1.5,1.29,1,
[0,1]);

img = imread([imgFolder num2str(imgRange(1)) '.tif']);
[imgH, imgW] = size(img);

fig = figure('Position', figureSize);

se = strel('rectangle', [smoothingHeight, smoothingWidth]);

if video == 1
    vid = VideoWriter([videoPath videoName ' ' datestr(now,'dd-mmmm-
yy HH.MM.SS')], 'Motion JPEG AVI');
    vid.FrameRate=framerate;
    vid.Quality = 100;
    open(vid);
end

lastBest = 0;
weight = 0.003;
choice = [];
meanChoiceX = [];

for i=imgRange
    disp(i)
    img = imread([imgFolder num2str(i) '.tif']);
    for j=minTemp:tempIncrement:maxTemp
        dataRow = ((j - minTemp) / tempIncrement) + 1;
        threshData(dataRow, 1) = j;
        thresh(:, :, dataRow) = imbinarize(img(row, col), j/65536);
        threshData(dataRow, 2) = nnz(thresh(:, :, dataRow));
    end
    grad = gradient(threshData(:, 2));

    [bestGrad, bestPoint] = findpeaks(grad);
```

```

% if cant find any peaks use the last point
if isempty(bestGrad)
    bestPoint = lastBest;
    bestGrad = grad(bestPoint);
end

%plot raw threshold counts data
subplot(2, 2, 2);
plot(threshData(:, 1), threshData(:, 2))
title('Threshold area, peaks highlighted')
n = 1:size(bestPoint, 1);
if size(n, 2) == 0
    [~, bestPoint] = min(abs(grad(2:end)));
    n = 1:size(bestPoint, 1);
end
%plot peaks of gradient on the raw data curve
hold on;
for j = n
    plot(threshData(bestPoint(j), 1), threshData(bestPoint(j), 2),
'm-o')
end
hold off;

for j=n
    mask(:, :, n) = imfill(thresh(:,:, bestPoint(n)), 'holes');
    mask(:, :, n) = imclose(mask(:, :, n), se);
    mask(:, :, n) = imerode(mask(:, :, n), se);
end

for k = n
    for j=row
        rowNum = (j - row(1)) + 1;
        if isempty(find(mask(rowNum, :, k), 1))
            curve(rowNum, k) = row(end);
        else
            curve(rowNum, k) = find(mask(rowNum, :, k), 1);
        end
    end
    curve(:, k) = curve(:, k) + col(1);
    curve(:, k) = movingAvg(curve(:, k), lineAvgSize);
end

%plot image and all potential best lines
subplot(2, 2, 1);
colourImg = ind2rgb(img - colourMin, colourMap);
imshow(colourImg);
colormap(colourMap);
bar = colorbar;
ax = gca;
ax.CLim = [colourMin, colourMax];
bar.Limits = [colourMin, colourMax];
title('Temperature image with possible freezing points(blue),
selected freezing point(pink)');
hold on;
for j = n
    plot(curve(:, j), row', 'b-', 'linewidth', 1.5);
end

% if we have more than 1 result compare the potential points to
the
% last an penalise for being futher away
if lastBest > 0

```

```

    multiplier = 1 - (abs(bestPoint - lastBest) * weight);
    bestGrad = bestGrad ./ multiplier;
    multiGrad = grad;
    multiGrad(bestPoint) = bestGrad;
    [~, nearest] = max(bestGrad);
else
    [~, nearest] = max(bestGrad);
end

% plot grad curve
subplot(2, 2, 4);
if lastBest > 0
    % plot weighted grad curve and winning point
    plot(threshData(:, 1), multiGrad, 'g');
    hold on;
    plot(threshData(bestPoint(nearest), 1),
multiGrad(bestPoint(nearest)), 'm-o');
end
plot(threshData(:, 1), grad);
title('Gradient of threshold area curve; unweighted(blue),
wighted(green), selected point(pink)');
hold off;

lastBest = bestPoint(nearest);

% plot best on image
subplot(2, 2, 1);
hold on;
plot(curve(:, nearest), row, 'm-', 'linewidth', 1.5);
hold off;

%record and plot choice
choice((i - imgRange(1)) + 1, :) = threshData(bestPoint(nearest),
1)';
meanChoiceX((i - imgRange(1)) + 1) = mean(curve(:, nearest));
subplot(2, 2, 3);
plot(choice);
title('History of selected temperatures of freezing point');
hold off;
drawnow;

if video == 1
    writeVideo(vid, getframe(fig));
end
end

if video == 1
    close(vid);
end

function avg = movingAvg(data, avgSize)
if size(data, 1) > size(data, 2)
    avg = zeros(size(data, 1) + (avgSize * 2), 1);
else
    avg = zeros(size(data, 2) + (avgSize * 2), 1);
end
avg(1:avgSize) = data(1);
avg(end - avgSize + 1: end) = data(end);
avg(avgSize + 1: end - avgSize) = data;
avg = filter((1/avgSize)*ones(1, avgSize), 1, avg);
avg = avg(avgSize+1: end - avgSize);
end

```

This code runs on a folder full of thermal images, as well as running the algorithm it also displays a live output for the user as each image is processed and saves a video of the resulting plots. This was useful when tuning the parameters of the algorithm.

### 7.3 Slag Detection Code

Below is a listing of the MATLAB scrip used to implement the pipe welding slag detection, the parameters for the run shown in this work are defined at the top of the script.

```
clearvars;
imageDir = 'imagePathRemoved';
imagePrefix = 'Meltpool floater';
imagePadding = 4;
imageExtension = '.tif';
imageRange = 10:99;

detectionBlobArea = 30;
detectionRadius = 50;
backgroundThresh = 1300;
lowThresh = -100;
highThresh = 100;

centroidRange = 10;
centroidRange2 = 50;

pxPmm = 72.2;
frameTime = 2.5e-3;

for i = imageRange
    j = (i - imageRange(1)) + 1;
    images(:, :, j) = imread([imageDir imagePrefix num2str(i, ['%0'
num2str(imagePadding) 'd']) imageExtension]);
    images(:, :, j) = images(:, :, j) .* uint16((images(:, :, j) >
backgroundThresh));
end

images = double(images);

for i = 2:size(images, 3)
    imageDiff(:, :, i) = images(:, :, i) - images(:, :, i-1);
end

imageDiff = imageDiff .* double(imageDiff < backgroundThresh / 2);
imageDiff = imageDiff .* double(imageDiff > -backgroundThresh / 2);

blobby = vision.BlobAnalysis('CentroidOutputPort', true, ...
    'BoundingBoxOutputPort', false, 'MajorAxisLengthOutputPort',
true, ...
    'MinorAxisLengthOutputPort', true, 'OrientationOutputPort',
true, ...
    'MinimumBlobArea', detectionBlobArea, 'MaximumCount', 1, ...
    'ExcludeBorderBlobs', false);

lowDiff = imageDiff < lowThresh;
highDiff = imageDiff > highThresh;

centroidsL = zeros(size(lowDiff, 3), 2);
centroidsH = zeros(size(highDiff, 3), 2);
lowOffsets = zeros(size(centroidsL, 1), 2);
highOffsets = zeros(size(centroidsH, 1), 2);
```

```

for i = 2:size(imageDiff, 3)
    %crop image to stop detecting the whole meltpool moving
    if sum(centroidsL(i-1, :), 2) > 1
        [lowOffsets(i, 1), lowOffsets(i, 2), tempImage] = ...
            cropImageAroundPoint(floor(centroidsL(i-1, 1)),
floor(centroidsL(i-1, 2)), lowDiff(:, :, i), detectionRadius);
        %imshow(tempImage);
        %pause;
    else
        tempImage = lowDiff(:, :, i);
    end
    if ~isempty(blobby(tempImage))
        [AreaL(i), centroidsL(i, :), majorL(i), minorL(i),
orientationL(i)] = blobby(tempImage);
        centroidsL(i, :) = centroidsL(i, :) + lowOffsets(i, :);
    end

    %crop image to stop detecting the whole meltpool moving
    if sum(centroidsH(i-1, :), 2) > 1
        [highOffsets(i, 1), highOffsets(i, 2), tempImage] = ...
            cropImageAroundPoint(floor(centroidsH(i-1, 1)), floor(centroidsH(i-
1, 2)), highDiff(:, :, i), detectionRadius);
        %imshow(tempImage);
        %pause;
    else
        tempImage = highDiff(:, :, i);
    end
    if ~isempty(blobby(tempImage))
        [AreaH(i), centroidsH(i, :), majorH(i), minorH(i),
orientationH(i)] = blobby(tempImage);
        centroidsH(i, :) = centroidsH(i, :) + highOffsets(i, :);
    end
end

centroidDiff = abs([0, 0; centroidsH(1:end-1, :)] - centroidsL);
validDetection = sum(centroidDiff, 2) < centroidRange &
sum(centroidDiff, 2) > 0;
validDetection = validDetection | sum(centroidDiff, 2) <
centroidRange2 & sum(centroidDiff, 2) > 0;
validDetection = validDetection(2:end);

for i = 1:size(validDetection)
    if validDetection(i) == 1
        centroid = floor(centroidsH(i, :));
        images(centroid(2):centroid(2)+1, centroid(1):centroid(1)+1, i)
= 800;
        centroidList(i, :) = centroid;
    end
end

%remove leading 0s
imageStart = 0;
while sum(centroidList(1, :), 2) < 1
    centroidList = centroidList(2:end, :);
    imageStart = imageStart + 1;
end
%duplicated entries when no detection
for i = 1:size(centroidList, 1)
    if sum(centroidList(i, :), 2) < 1
        centroidList(i, :) = centroidList(i-1, :);
    end
end

```

```

end

lastI = 1;
for i = 1:size(validDetection, 1)
    if validDetection(i) == 1
        cI = i - imageStart;
        if cI > 1
            dx = abs(centroidList(cI, 1) - centroidList(cI-1, 1));
            dy = abs(centroidList(cI, 2) - centroidList(cI-1, 2));
            distancePx(cI) = sqrt((dx ^ 2) + (dy ^ 2));
            distanceM(cI) = distancePx(cI) / (pxPmm * 1000);
            speedMs(cI) = distanceM(cI) / (frameTime * (cI - lastI));
            %disp(['i: ' num2str(i) ' frames since detection: '
num2str(cI - lastI)]);
            end
            lastI = cI;
        end
    end
end

figure
montage(images)
caxis([800 2000]);
colormap(parula);

f = figure;
for i = 1:size(centroidList, 1)
    imshow(images(:, :, i + imageStart))
    hold on;
    plot(centroidList(1:i, 1), centroidList(1:i, 2), '-r');
    caxis([800 2000]);
    colormap(parula);
    imagesC(:, :, :, i) = getframe(gcf);
    hold off;
end
close(f);
implay(imagesC)

figure;
plot(speedMs);

```

This code runs on a folder full of thermal images, as well as running the algorithm it also displays a live output for the user as each image is processed. When finished displays an animation of the track progression and a plot of the speed along the track. This was useful when tuning the parameters of the algorithm.

## 7.4 Neural Network Training Code

Below is a listing of the MATLAB script used to create and train the final iteration of the neural network.

```

load('groundTruths.mat');

%Setup Datasets
imDir = fullfile('pathToImagesRemoved');
pxDir = fullfile('pathToLabelDataRemoved');

imDs = imageDatastore(imDir);
pxDs = pixelLabelDatastore(gTruth);

```

```

% Create NN
inputSize = [512 1100];
imgLayer = imageInputLayer(inputSize);

filterSize = 5;
numFilters = 64;
conv = convolution2dLayer(filterSize, numFilters, 'Padding', [2,
4]);
relu = reluLayer();

poolSize = 2;
maxPoolDownsample2x = maxPooling2dLayer(poolSize, 'Stride', 2);

downsamplingLayers = [conv, relu, maxPoolDownsample2x, ...
    conv, relu, maxPoolDownsample2x, conv, relu,
maxPoolDownsample2x];

filterSize = 4;
transposedConvUpsample2x = transposedConv2dLayer(filterSize,
numFilters, 'Stride', 2, 'Cropping', [1, 3]);

upSamplingLayers = [transposedConvUpsample2x, relu, ...
    transposedConvUpsample2x, relu, transposedConvUpsample2x,
relu];

numClasses = size(gTruth.LabelDefinitions, 1);
conv1x1 = convolution2dLayer(1, numClasses);

%calculate wieghts for final layer based on number of pixels in
each class
tbl = countEachLabel(pxDs);
totPx = sum(tbl.PixelCount);
freq = tbl.PixelCount / totPx;
classWeights = 1 ./ freq;

finalLayers = [conv1x1, softmaxLayer(), ...
    pixelClassificationLayer('Classes', tbl.Name, 'ClassWeights',
classWeights)];

layers = [imgLayer, downsamplingLayers, upSamplingLayers,
finalLayers];

% Train Network
allTrainingData = pixelLabelImageDatastore(imDs, pxDs);

%trainingInd = randi(100, 20, 1);
%trainingData = partitionByIndex(allTrainingData, trainingInd);

%validationInd = randi(100, 5, 1);
%validationData = partitionByIndex(allTrainingData, validationInd);

%[trainSet, valiSet, TestSet] = splitEachLabel(trainingData, 0.8,
0.1);

opts = trainingOptions('sgdm', 'InitialLearnRate', 0.001, ...
    'MaxEpochs', 1000, 'MiniBatchSize', 10, 'Shuffle', 'every-
epoch', ...
    'Plots', 'training-progress', 'ExecutionEnvironment',
'parallel', ...
    'ValidationData', validationData, 'CheckpointPath', ...
    'checkpointPathRemoved');

```

```

net = trainNetwork(trainingData, layers, opts);

%% Continue training
%select network checkpoint
[file, path] = uigetfile;
load([path, file]);

trainingInd = randi(100, 30, 1);
trainingData = partitionByIndex(allTrainingData, trainingInd);

validationInd = randi(100, 7, 1);
validationData = partitionByIndex(allTrainingData, validationInd);

%[trainSet, valiSet, TestSet] = splitEachLabel(trainingData, 0.8,
0.1);

opts = trainingOptions('sgdm', 'InitialLearnRate', 0.001, ...
    'MaxEpochs', 200, 'MiniBatchSize', 10, 'Shuffle', 'every-
epoch', ...
    'Plots', 'training-progress', 'ExecutionEnvironment',
'parallel', ...
    'ValidationData', validationData, 'CheckpointPath', ...
    'checkpointPathReomved');

net = trainNetwork(trainingData, net.Layers, opts);

```

The below code was also used to evaluate networks at each of their checkpoints with an unseen dataset.

```

nndir = 'patheToNetworkCheckpointsRemoved';
imDir = fullfile(pathToUnseenImagesRemoved);
pxDir = fullfile('pathToUnseenLabelsRemoved');

load('./Test Data\groundTruthTestData.mat');

imDs = imageDatastore(imDir);
pxDs = pixelLabelDatastore(pxDir,
table2cell(gTruth.LabelDefinitions(:, 1)),
table2cell(gTruth.LabelDefinitions(:, 3)));

nets = dir([nndir '*.mat']);
[~,ind] = sort([nets.datenum]);
nets = nets(ind);

allMetrics = [];

for i = 1:size(nets, 1)
    load([nndir, nets(i).name]);
    disp(['Evaluating ' nets(i).name]);

    pxDsRes = semanticseg(imDs, net, 'WriteLocation', './Temp\',
'UseParallel', true, 'ExecutionEnvironment','cpu');

    metrics = evaluateSemanticSegmentation(pxDsRes, pxDs,
'UseParallel', true);
    allMetrics = [allMetrics; metrics.DataSetMetrics];
end

save('checkpointEvaluations.mat', allMetrics);

```